



Estd. 1962
"A++" Accredited by NAAC (2021)
with CGPA 3.52

SHIVAJI UNIVERSITY, KOLHAPUR

JOURNAL OF SHIVAJI UNIVERSITY : SCIENCE AND TECHNOLOGY

(Peer Reviewed Journal)

Volume-47, Issue-2 (July, 2021)

ISSN Science-0250-5347



JOURNAL OF SHIVAJI UNIVERSITY : SCIENCE AND TECHNOLOGY

(Peer Reviewed Journal)

Volume-47, Issue-2 (July, 2021)

ISSN Science-0250-5347

EDITORIAL BOARD OF THE JOURNAL

Prof. (Dr.) D. T. Shirke

Chairman

Hon'ble Vice Chancellor, Shivaji University, Kolhapur

Prof. (Dr.) P. S. Patil

Hon'ble Pro Vice Chancellor, Shivaji University, Kolhapur

Dr. V. N. Shinde

Registrar (Ag.), Shivaji University, Kolhapur

Prof. (Dr.) Smt. S. H. Thakar

Dean, Faculty of Science & Technology, and
Head, Department of Mathematics, Shivaji University, Kolhapur

Prof. (Dr.) S. D. Delekar

Editor,

Department of Chemistry, Shivaji University, Kolhapur

MEMBERS OF THE EDITORIAL BOARD

Prof. (Dr.) K. Y. Rajpure	Head, Dept. of Physics, Shivaji University, Kolhapur
Prof. (Dr.) Smt. J. P. Jadhav	Head, Dept. of Bio-technology, Shivaji University, Kolhapur
Prof. (Dr.) K. D. Sonawane	Head, Dept. of Biochemistry, Shivaji University, Kolhapur
Dr. S. N. Sapali	Director, Dept. of Technology, Shivaji University, Kolhapur
Prof. (Dr.) R. V. Gurav	Head, Dept. of Botany, Shivaji University, Kolhapur
Prof. (Dr.) S. B. Mahadik	Head, Dept. of Statistics, Shivaji University, Kolhapur
Dr. Smt. K. S. Oza	Head, Dept. of Computer Science, Shivaji University, Kolhapur
Prof. (Dr.) A. A. Deshmukh	Head, Dept. of Zoology, Shivaji University, Kolhapur
Prof. (Dr.) K. K. Sharma	Head, Dept. of Nano Science & Technology, Shivaji University, Kolhapur
Prof. (Dr.) S. D. Shinde	Head, Dept. of Geography, Shivaji University, Kolhapur
Dr. Smt. A. S. Jadhav	Head, Dept. of Environmental Science, Shivaji University, Kolhapur
Prof. (Dr.) P. K. Gaikwad	Head, Dept. of Electronics, Shivaji University, Kolhapur



Estd. 1962
"A++" Accredited by NAAC (2021)
with CGPA 3.52

Shivaji University
Kolhapur 416 004 (INDIA)

**JOURNAL OF SHIVAJI UNIVERSITY :
SCIENCE AND TECHNOLOGY**

(Peer Reviewed Journal)

.....
Volume-47, Issue-2 (July, 2021)
.....

ISSN Science-0250-5347
.....

- Contact Details -

Prof. (Dr.) S. D. Delekar

Editor, Journal of Shivaji University : Science and Technology
and

Department of Chemistry

Shivaji University, Kolhapur 416 004 (India)

E-mail : editor,jscitech@unishivaji.ac.in

website : <http://www.unishivaji.ac.in/journals/>

Shivaji University, Kolhapur

**JOURNAL OF SHIVAJI UNIVERSITY :
SCIENCE AND TECHNOLOGY**

(Peer Reviewed Journal)

.....
Volume-47, Issue-2 (July, 2021)
.....

ISSN Science-0250-5347
.....

- Editor -

Prof. (Dr.) S. D. Delekar
Journal of Shivaji University :
Science and Technology

- Published by -

Dr. V. N. Shinde
Ag. Registrar,
Shivaji University, Kolhapur 416004.

- Printed by -

Shri. B. P. Patil
Superintend
Shivaji University, Kolhapur 416004.

The Editor, on behalf of the Editorial Board of the Journal of Shivaji University : Science and Technology, Vol. No. 47 (2) wishes to express his thanks to the contributing authors and the experts for acting as referees for the papers included in the issue.

Published : July, 2023

Journal of Shivaji University: Science and Technology
Volume-47, Issue-2 (July, 2021)

INDEX

Sr. No.	Title of Research Article with Name of Author/s	Page No.
1.	One-Step in Situ Polymerization of Polythiophene Fibrous Microbundles for Electrochemical Storage Application Rahul S. Redekar, Kishor V. Patil, Alaka A. Bhoite, Nilesh L. Tarwal	1
2.	Recent Spray Deposited Materials for Solar Cell Application Kishor V. Patil, Rahul S. Redekar, Alaka A. Bhoite, Nilesh L. Tarwal	11
3.	Chemically Derived Carbon Aerogel Electrodes for Supercapacitors Ashwini V. Patil, Rajiv S. Vhatkar	28
4.	Investigation of Effect of Critical Power of Beam on Propagation of Super Gaussian Beam in Collisional Plasma Prasad T. Takale, Vinayak S. Pawar, Kalyani Y. Khandale, Sanyogita S. Patil, Sandip D. Patil, Mansing V. Takale	39
5.	Effect of Self-focusing and Diffraction Length on Propagation of Gaussian Laser Beam in Non-Degenerate Germanium having Space Charge Neutrality Kalyani Y. Khandale, Trupti U. Urunkar, Prasad T. Takale, Sanyogita S. Patil, Purva P. Nikam, Manisha B. Mane, Sandip D. Patil, Mansing V. Takale	45
6.	A Facile Hydrothermal Synthesis of Nickel Phosphate Hydrate for Supercapacitors Satyajeet S. Patil, Sumit D. Korade, Sarika B. Dhavale, Shweta M. Pawar, Pramod S. Patil	53
7.	Synthesis and Characterization of Barium Titanate Perovskite by Co-precipitation for Oxygen Evolution Reaction Rohit K. Kamble, Sharadchandra S. Patil, Prashant N. Nikam, Umesh M. Chougale, Gaurav M. Lohar, Vijay J. Fulari	63
8.	Air Quality and Air Ion Assessment Ratio for Papaya, Chickpea, and Guava Vegetation Area at Rural Station Khatav (16°57'N, 74°31'E) Subhash D. Pawar, Gajanan B. Patil, Prachi G. Patil, Pratik G. Patil, Jalindar L. Bhosale	71

Department of Physics
Shivaji University, Kolhapur
Journal of Shivaji University : Science & Technology
Volume-47, Issue-2 (July, 2021)
Departmental Editorial Board

Sr. No.	Name of the Faculty	Editorial Board Designation
1.	Dr. K. Y. Rajpure	Chairman
2.	Dr. N. L. Tarwal	Member
3.	Dr. M. V. Takale	Member
4.	Dr. J. B. Yadav	Member

One-Step in Situ Polymerization of Polythiophene Fibrous Microbundles for Electrochemical Storage Application

Rahul S. Redekar^a, Kishor V. Patil^a, Alaka A. Bhoite^a, Nilesh L. Tarwal^{a,*}

^aDepartment of Physics, Shivaji University, Kolhapur 416 004 (MS) India.

*Corresponding author: nlt.phy@unishivaji.ac.in

ABSTRACT

Supercapacitors have been far explored in these years due to their higher power density and energy density than other energy storage devices. In this study, polythiophene fibrous microbundles are synthesized one-step in situ polymerization method. The structural and morphological analysis of polythiophene powder is carried out with help of X-ray diffraction, Fourier transforms infrared spectroscopy, and Scanning electron microscopy. The electrochemical performance of polythiophene-coated stainless steel is studied in 1 M KOH electrolyte within a -0.1 to 0.3 V potential window at various scan rates and current densities. The obtained specific capacitance was 155.58 F/g at 1 mA/cm² current density. Based on the results, Polythiophene powder can be used as an electrode for high-performance supercapacitor applications.

KEYWORDS

Polythiophene, Polymerization, Supercapacitor, Energy storage.

.....

1. INTRODUCTION

In recent years, climate change has become a major issue in front of the world. Also, non-renewable resources are facing a burden due to the growing industrialization and population which put the world into an energy crisis issue. Use of the renewable resources is one of solution on the climate change as well as the energy crisis. Among all renewable resources, solar, wind, and tidal resources have eco-friendly nature, are cheap, and are easy to access. But they have intermittent nature. So, it is necessary to store the energies from these resources for future purposes [1,2]. For storing such energies, various types of energy storage systems (ESS) have developed in the last few years. Among them, capacitors, supercapacitors, and batteries are the most known ESS. By virtue of advantages, recently supercapacitors have been studied extensively as more efficient energy storage devices. It has more energy storage capacity than the capacitor and more power density than the battery. It has the ability to fill the gap between the conventional capacitor and the battery [3]. The basic construction of a supercapacitor has consisted of two conducting electrodes. The electrolyte solution is

placed in the space between these two electrodes. As the potential is applied to electrodes, the charge formation takes place in the electrolyte solution. These charges are traveled towards the polarized electrode which results in the storage of charges at the electrode-electrolyte interface [4]. Based on the materials used in electrodes, these charges are stored in two ways, one is electrostatic (non-faradic) and the second is electrochemical (faradic) [5]. Respective of these two ways, supercapacitors are broadly classified as electrical double-layer capacitors, pseudocapacitors, and hybrid supercapacitors [6]. In EDLC, the charges are stored electrostatically in a double-layer known as the Helmholtz double-layer. On the contrary, charges are stored via adsorption, redox reactions, and intercalation in a pseudocapacitor [7]. The hybrid supercapacitor has both types of electrodes, one is EDLC type and another is pseudocapacitive type. Again, a hybrid supercapacitor has also three sub-types such as asymmetric, composite-type, and battery-type whereas all hybrid sub-types are better promising supercapacitors with excellent performance [8]. As mentioned above, the storage mechanism of the supercapacitor is primarily dependent on the electrode material. Comparing the performances of all materials, pseudocapacitive materials have come forward with superior specific capacitances, high energy densities, and excellent power densities [9]. Conducting polymers and metal oxides are dominant groups of pseudocapacitive materials. Among them, conducting polymers have been explored for pseudocapacitance due to their characteristic properties like high conductivity, high mechanical strength, lightweight, easy synthesis and processibility, high purity, high theoretical capacitance, excellent rate capability, and ability to intercalate [10, 11]. Up to now, various conducting polymers were examined for supercapacitive performances. Conducting polymers like polyaniline (PANI) [12], Polypyrrole (PPy) [13], Polythiophene (PTh) [14], and derivatives of polythiophene [15] have shown their excellent contribution in the supercapacitor field. Among these conducting polymers, polythiophene has been studied as a supercapacitor material by many researchers due to its high structural stability and better electrochemical performance. Till now, polythiophene synthesized using cost-effective routes such as in situ polymerization and electrochemical polymerization. Gnanakan et al. [16] synthesized the nanoparticles of polythiophene by dilute polymerization with help of a surfactant. The synthesized polythiophene nanoparticles were coated on stainless steel foil to fabricate electrodes. The obtained specific capacitance of the electrode was about 134 F/g at a scan rate of 5 mV/s. besides, Senthilkumar et al. [17] compared the performances of the chemically polymerized pure polythiophene and surfactant-assisted polythiophene. The sample prepared with Triton-X surfactant showed better specific capacitance than the pure one. The highest specific capacitance of the Triton-X-assisted polythiophene was about 117 F/g at 5 mV/s.

In the present study, polythiophene fibrous microbundles have been synthesized by a cost-effective in situ polymerization method. Polythiophene fibrous microbundles have been characterized for its structural, morphological, and

electrochemical properties. The electrochemical properties have been examined in 1 M KOH solution for various scan rates and current densities. Based on the results, polythiophene can be considered an electrode material for supercapacitor applications.

2. EXPERIMENTAL SECTION

2.1. Chemicals

Thiophene monomer (99%, pure), FeCl₃ (Ferric chloride anhydrous, 99% pure), and Chloroform (99%, pure) were purchased from Cisco-SRL Co. Ltd and used as a precursor. All chemicals are AR grade and used without further purification

2.2. Synthesis of Polythiophene Fibrous Microbundles

The *in-situ* polymerization of the thiophene monomer was carried out with help of the oxidizing agent FeCl₃. In prior synthesis, 0.1 M of thiophene monomer was added to 20 ml of chloroform and then the solution was stirred for 20 min vigorously. Similarly, 0.1 M of FeCl₃ was added to another beaker with 20 ml chloroform and stirred for 20 mins. After stirring, the FeCl₃ solution was added dropwise to the monomer solution. After the addition of FeCl₃, the colour of the reaction solution was changed from colour-less to black colour and polymerization of the thiophene monomer was started. After 2 hrs, the black-colored precipitate was collected and washed with ethanol and acetone to remove unreacted monomer and oxidizing agent. After washing, the colour of the precipitate was changed from black to brown which confirm the polymerization of thiophene. Finally, the precipitate was dried at 60°C for 6 hrs. The final product was brown-colored polythiophene powder

2.3. Characterizations

The structural and morphological properties of the polythiophene powder were investigated by various characterization techniques. The structural formation was investigated by X-ray powder diffractometer (XRD) with Cu K α = 1.54 Å wavelength (Bruker AXS Analytical Instruments Private Ltd., Germany, D6 phaser). The functional group analysis was carried out with help of Fourier transform infrared spectroscopy (FT-IR) in the range 4000-400 cm⁻¹ (JASCO, Lisses, France). The morphology and surface analysis were studied by Scanning electron microscopy (SEM) (JEOL JSM-6360).

2.4. Electrochemical Characterization

The electrochemical properties were studied with the help of Autolab potentiostat) (Metrohm Autolab, PGSTAT302N, Netherland). The analysis was carried out in a three-electrode system with 1 M KOH as an electrolyte. In the three-electrode system, Graphite was used as the counter electrode, saturated calomel electrode as a reference, and the polythiophene-based working electrode. The working electrode was prepared by making a slurry of synthesized polythiophene powder (80%), carbon black (10%),

conducting agent), and polyvinylidene fluoride (PVDF) (10%, binder) in the solvent N-Methyl-2-pyrrolidone (NMP). The prepared slurry was coated on a 1 cm² pre-treated stainless steel substrate and dried at 70°C for 12 hrs. The mass of active material in prepared electrode was 0.9 mg/cm².

3. RESULTS AND DISCUSSION

The XRD pattern of the polythiophene powder is shown in **Figure-1**. From the XRD pattern., it is revealed that; the polythiophene has amorphous nature. Near a diffraction angle of 20°, a presence of a broad peak was observed [18]. The presence of this peak indicates the intermolecular π - π stacking of the polythiophene rings.

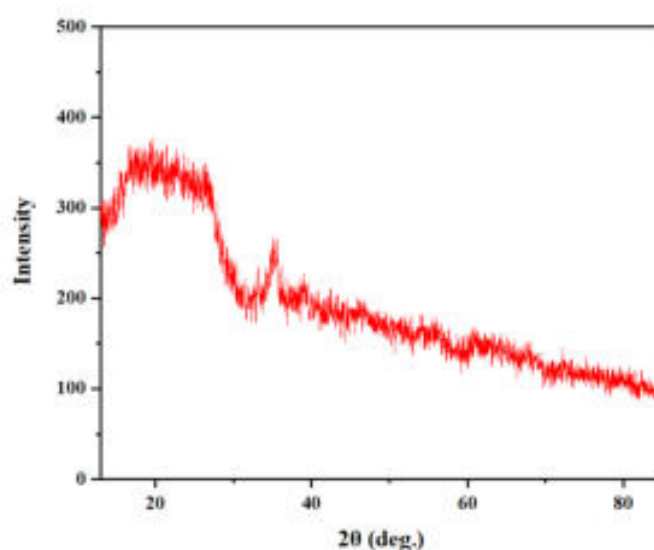


Figure-1. XRD pattern of Polythiophene powder.

The detection of the function groups and bands is confirmed by the FT-IR spectrum in the range of 500-4000 cm⁻¹. The FT-IR spectrum of polythiophene is shown in **Figure-2**. In **Figure-2**, the functional absorption peak at 678 cm⁻¹ is attributed to the C-S stretching in the ring of thiophene. Besides, during the polymerization of the monomer, out-of-plane vibration of the C-H bond caused the absorption of the peak at 781 cm⁻¹ [19, 20]. While in-plane stretching vibration of C-H can be seen at 1021 cm⁻¹. The peaks present at 1482 and 1436 cm⁻¹ are attributed to the stretching vibrations of the C=C vibration. The presence of the water can be seen at 3425 cm⁻¹. The region 600-1500 cm⁻¹ is corresponding to the polythiophene fingerprint region [21]. All Peaks are well agreed with the literature.

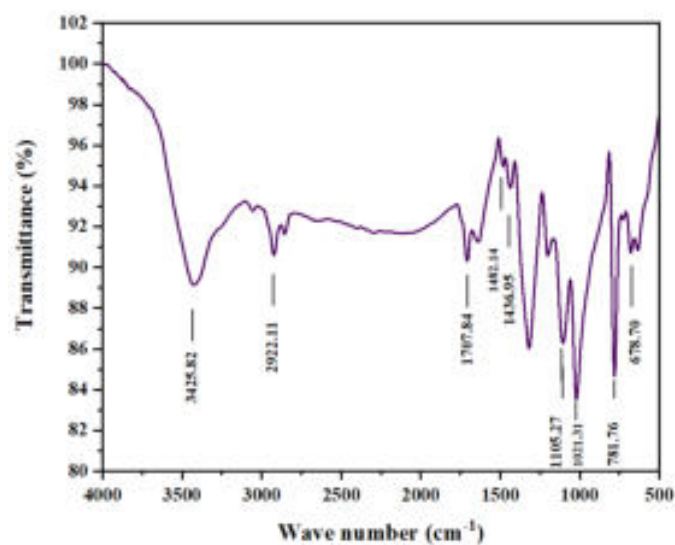


Figure-2. FTIR spectra of Polythiophene powder.

The surface morphological studies of polythiophene powder were carried out with help of SEM micrographs. **Figure-3a** to **Figure-3d** show the SEM micrographs of polythiophene powder at various magnifications such as X 1000, X 5000, X 7500, and X 10000, respectively.

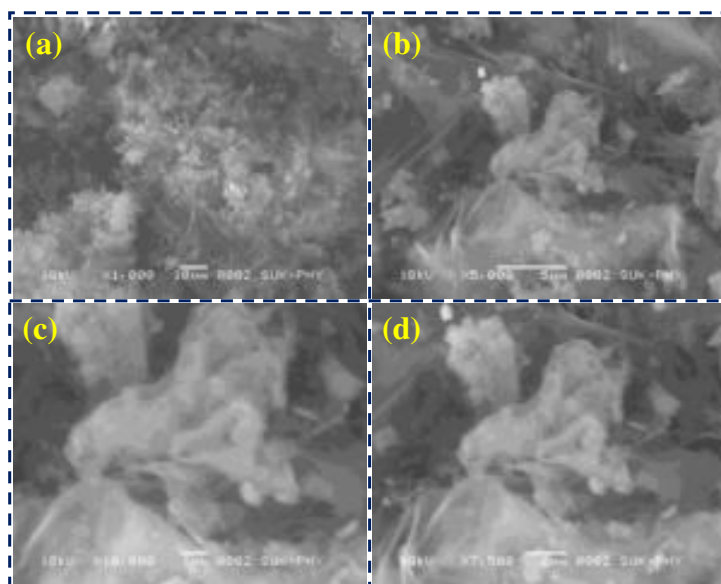


Figure-3. SEM micrographs of Polythiophene powder at different magnifications (a) X1000, (b) X5000, (c) X7500, and (d) X10000.

From **Figure-3**, Formation of the small bundles of the cloth-like fibrous microstructure of the polythiophene can be seen. Some cloth-like microbundles were wrapped around themselves and interconnected with each other's to form a porous microstructure. The formation of the such interconnection helped to store more charges during the redox reactions.

The electrochemical behavior of the polythiophene-coated stainless steel was studied in the 1 M KOH solution within the potential window -0.1 to 0.3 V against the SCE. The cyclic voltammetry was analyzed at different scan rates such as 10, 20, 40, 60, 80, and 100 mV/s as given in **Figure-4**. From **Figure-4**, It is seen that the shapes of the CV plots have deviated from the typical rectangular shape which confirmed the pseudocapacitive nature of the polythiophene electrode [22].

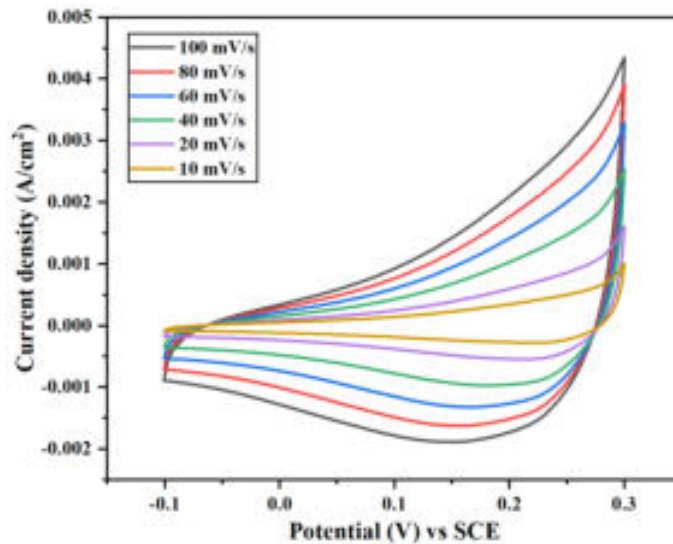
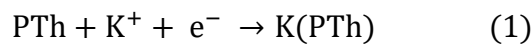


Figure-4. Cyclic voltammetry of polythiophene electrode.

Also, as the scan rate increased, the area under the CV curves increased. At a high scan rate of 100 mV/s, a maximum area under the curve was observed [23]. The deviated rectangular shape of CV curves denoted the Faradic capacitive charge storage in polythiophene. Basically, the polythiophene stores the charges through the doping/oxidation and de-doping/reduction processes. The potential charging-discharging mechanism can be given as follows [24, 25],



From the above equation, it can be seen that the formation of the polaron led to the pseudocapacitive charge storage of the polythiophene. The charge storage capacity of the polythiophene electrode was investigated by the galvanostatic charge-discharge technique. The GCD plots of polythiophene were studied at various current

densities as 1, 2, 3, and 4 mA/cm². **Figure-5** shows the GCD plots of polythiophene electrodes. The deviation from the triangular shape of GCD plots represented the pseudocapacitive nature of the electrode during charging and discharging [26]. At a low current density of 1 mA/cm², the electrode shows higher discharging which means higher charge storage. The specific capacitances (C), energy densities (E), and power densities (P) from these GCD plots were calculated using the following expression [27],

$$C = \frac{I \times \Delta t}{m \times \Delta V} \left(\frac{F}{g} \right) \quad (2)$$

$$E = \frac{C \times \Delta V^2}{2 \times 3.6} \left(\frac{Wh}{kg} \right) \quad (3)$$

$$P = \frac{E \times 3600}{\Delta t} \left(\frac{W}{kg} \right) \quad (4)$$

Here, I is current density, Δt is discharge time, m is mass of active material and ΔV is a potential window.

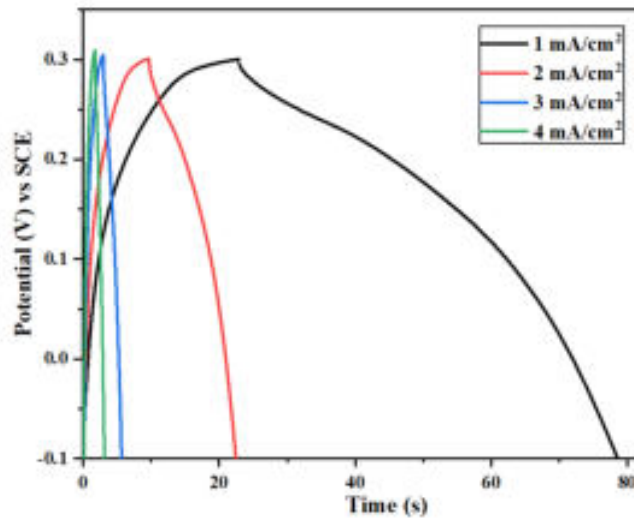


Figure-5. Galvanostatic charge-discharge profiles of polythiophene electrode.

The calculated specific capacitances of the polythiophene electrode from the GCD plot were as 155.58, 71.05, 21.75, and 12.22 F/g at 1, 2, 3, and 4 mA/cm², respectively. This showed that polythiophene electrodes could be good electrode material for supercapacitors. The energy densities and power densities of the polythiophene electrode were calculated using formulae (2) and (3). The highest energy of 5.186 Wh/kg was obtained at 333.33 W/kg power density and the highest power density of 1332.01 W/kg was obtained at 0.402 Wh/kg energy density.

The electrochemical impedance of the polythiophene was analyzed in the frequency range 100 kHz-0.1 Hz with an AC amplitude of 10 mV. **Figure-6** shows the Nyquist plot of the polythiophene electrode. From the Nyquist plot, at high frequency, a small deviated semicircle and a straight line at the lower frequency region are seen [28, 29].

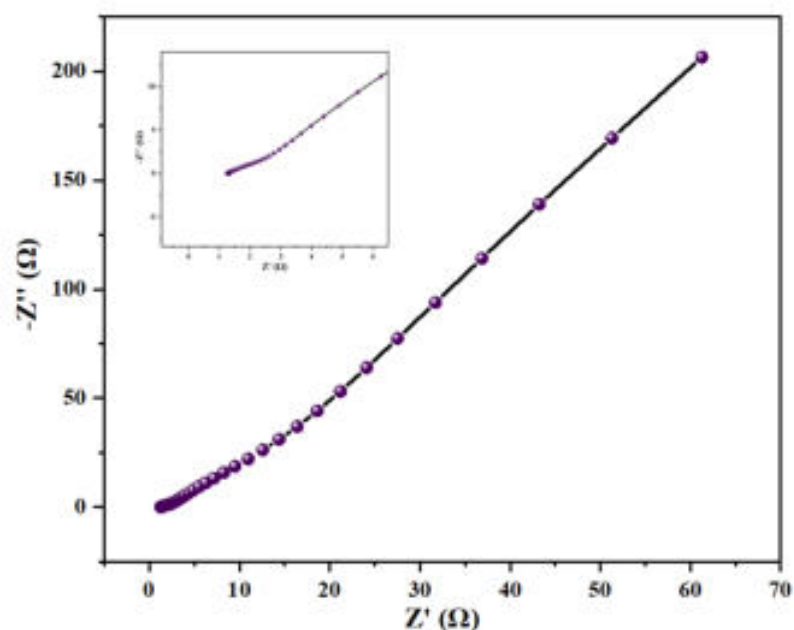


Figure-6. Nyquist plot of Polythiophene electrode.

In the high-frequency region, the value of the series resistance (R_s) was obtained at about 1.25 Ω and in the mid-frequency region, the charge transfer resistance (R_{ct}) of 5.49 Ω was obtained.

4. CONCLUSION

Single-step in situ polymerization method was used to synthesize polythiophene powder. From the XRD pattern, the amorphous nature of polythiophene was observed while from the FTIR study, the polymerization of monomer was confirmed. The interconnected fibrous microbundles of polythiophene served as porous microstructure for storing the electrochemical charge. The obtained highest specific capacitance of polythiophene electrode was 155.58 F/g at 1 mA/cm². The highest energy density was about 5.186 Wh/kg and the highest power density was about 1332.01 W/kg.

ACKNOWLEDGEMENT

Nilesh L. Tarwal is thankful to Shivaji University Kolhapur for providing financial assistance through Research Initiation Scheme. All Authors are thankful to UGC-DSA Phase II (2018-2023) and DST-PURSE Phase-II (2018-2023) Department of Physics, Shivaji University, Kolhapur (MS) India.

REFERENCES

1. Augustyn, V., Simon, P., Dunn, B. (2014) *Energy & Environmental Science*, 7, 1597.
2. Winter, M., Brodd, R. J. (2004) *Chemical Reviews*, 104, 4245-4270.
3. Kim, B. K., Sy, S., Yu, A., Zhang, J. (2015) *Handbook of Clean Energy Systems*, 1-25.
4. Zhang, L., Hu, X., Wang, Z., Sun, F., Dorrell, D. G. (2018) *Renewable and Sustainable Energy Reviews*, 81, 1868-1878.
5. González, A., Goikolea, E., Barrena, J. A., Mysyk, R. (2016) *Renewable and Sustainable Energy Reviews*, 58, 1189-1206.
6. Wang, C., Zhou, E., He, W., Deng, X., Huang, J., Ding, M., Wei, X., Liu, X., Xu, X. (2017) *Nanomaterials*, 7, 41.
7. Pan, H., Li, J., Feng, Y. (2010) *Nanoscale Research Letters*, 5, 654-668.
8. Chen, X., Paul, R., Dai, L. (2017) *National Science Review*, 4, 453-489.
9. Shao, Y., El-Kady, M. F., Sun, J., Li, Y., Zhang, Q., Zhu, M., Wang, H., Dunn, B., Kaner, R. B. (2018) *Chemical Reviews*, 118, 9233-9280.
10. Snook, G. A., Kao, P., Best, A. S. (2011) *Journal of Power Sources*, 196, 1-12.
11. An, C., Zhang, Y., Guo, H., Wang, Y. (2019) *Nanoscale Advances*, 1, 4644-4658.
12. Eftekhari, A., Li, L., Yang, Y. (2017) *Journal of Power Sources*, 347, 86-107.
13. Ma, G., Peng, H., Mu, J., Huang, H., Zhou, X., Lei, Z. (2013) *Journal of Power Sources*, 229, 72-78.
14. Laforgue, A., Simon, P., Sarrazin, C., Fauvarque, J. F. (1999) *Journal of Power Sources*, 80, 142-148.
15. Patil, D. S., Pawar, S. A., Kim, J. H., Patil, P. S., Shin, J. C. (2016) *Electrochimica Acta*, 213, 680-690.
16. Gnanakan, S. R. P., Rajasekhar, M., Subramania, A. (2009) *International Journal of Electrochemical Science*, 4, 1289-1301.
17. Senthilkumar, B., Thenamirtham, P., Selvan, R. K. (2011) *Applied Surface Science*, 257, 9063-9067.
18. Kulkarni, G., Kandesar, P., Velhal, N., Phadtare, V., Jatratkar, A., Shinde, S. K., Kim, D. Y., Puri, V. (2018) *Chemical Engineering Journal*, 355, 196-207.
19. Zhang, H., Hu, L., Tu, J., Jiao, S. (2014) *Electrochimica Acta*, 120, 122-127.

20. Wu, K., Zhao, J., Wu, R., Ruan, B., Liu, H., Wu, M. (2018) *Journal of Electroanalytical Chemistry*, 823, 527-530.
21. Patil, B. H., Jagadale, A. D., Lokhande, C. D. (2012) *Synthetic Metals*, 162, 1400-1405.
22. Lu, Q., Chen, J. G., Xiao, J. Q. (2013) *Angewandte Chemie International Edition*, 52, 1882-1889.
23. Feng, L., Zhu, Y., Ding, H., Ni, C. (2014) *Journal of Power Sources*, 267, 430-444.
24. Liu, Y., Zhitomirsky, I. (2015) *Journal of Power Sources*, 284, 377-382.
25. Moritomo, Y., Sugano, T., Fukuzumi, Y., Iwaizumi, H., Yasuda, T. (2019) *Journal of Electroanalytical Chemistry* 839, 210-213.
26. Zhang, H., Hu, Z., Li, M., Hu, L., Jiao, S. (2014) *Journal of Materials Chemistry A*, 2, 17024-17030.
27. Qin, W., Zhou, N., Wu, C., Xie, M., Sun, H., Guo, Y., Pan, L. (2020) *ACS Omega*, 5(8), 3801-3808.
28. Ates, M. (2011) *Progress in Organic Coatings*, 71, 1-10.
29. Gnanakan, S. R. P., Muruganathan, N., Subramania, A. (2011) *Polymers for Advanced Technologies*, 22, 788-793.

Recent Spray Deposited Materials for Solar Cell Application

Kishor V. Patil^a, Rahul S. Redekar^a, Alaka A. Bhoite^a, Nilesh L. Tarwal^{a,*}

^aDepartment of Physics, Shivaji University, Kolhapur 416 004 (MS) India.

*Corresponding author: nlt.phy@unishivaji.ac.in

ABSTRACT

In recent decades, various materials have been used for energy conversion devices. Thin films attracted great attention for photovoltaic applications. The spray pyrolysis technique is the low costs chemical method used for large-area deposition of thin films in a compact nature that were useful for photovoltaic applications. The method is largely applicable to the synthesis of metal oxides, sulfides, nitrides, selenides, and quaternary chalcogenide semiconducting materials. The compactness of thin films, easy synthesis process, and large deposition area made it more popular for solar cell applications. This review, the based on the basics of the solar cell and its parameters and spray-deposited materials that have been used for photovoltaic applications.

KEYWORDS

Solar cell, Spray pyrolysis, Semiconducting materials, Thin films, Efficiency.

.....

1. INTRODUCTION

Recently, the global environment being unbalanced due to the enormous rise in the population, overuse of fuels, the high release of hazardous gases due to the burning of fossil fuels, etc. which highly contribute to global warming-like issues. So, shifting from these non-renewable energy sources to renewable ones is today's generation's need. Free, highly available, renewable energy sources like wind, solar, tidal, hydro, geothermal, biomass energies, etc. have a large capability to fulfill our recent as well as future energy needs without harnessing the environmental conditions. Among all of these, solar energy has great potential for fulfillment of energy demand, as one-hour solar energy is sufficient for a one-year energy requirement of the whole world [1]. To decrease environmental pollution, changing weather conditions, imbalance in the seasons on earth, and the global rise in the heat, etc. the scientific community is more convenient to use renewable energy sources on a large scale to fulfill the expected 33% energy need in next 20 years [2].

Most of the solar energy reaches the earth in the form of radiation i.e., UV, visible, and infrared. These high-energy radiations can be utilized for the conversion of energy by different photoabsorbing materials. Different solar cell devices based on

the photovoltaic effect were used for electricity production. Solar cell devices are made up of various layers in which photo-absorbing materials are the heart of the device [3]. Various solar cell devices have been used for this conversion of light into electricity viz. thin film solar cells (TFSC) [4], dye-sensitized solar cells (DSSC) [5], perovskite solar cells (PSC) [6], multijunction solar cells [7], organic solar cells [8], etc. Among all of these, the TFSC has great attention in the field of energy conversion devices due to their high stability, low consumption of materials, high device efficiency with less input, easy fabrication techniques, etc. [9]. For the crystalline silicon solar cell, the record breaks efficiency of about 26.7% [10], beyond that due to the sophisticated instrumentation and high costs that replacing it with other materials [11]. Whereas, in the next era of TFSC technology the CdTe and CIGS have attracted great attention from all the researchers due to their well optimum band gap, low costs, and slightly high efficiency than the costs of silicon solar cells. The CdTe and CIGS solar cells show the maximum solar cell efficiency of about 22% and 22.8% respectively [12,13]. These TFSCs have more commercialization due to easy stoichiometry, better reproducibility, and high efficiency [14]. Thin films have great attention in various fields due to their low material consumption leading to low-cost devices, large-area deposition, small thickness, and easy synthesis techniques with flexibility in material properties that attract more attention in solar cell applications [15]. TFSCs are combined with different materials in the form of a thin film having a structure of substrate/transparent conducting oxides/window layer/absorber/top contact [16]. Along with that, the next generation of thin films depends on lower costs, less toxicity, and commercial solar cell fabrication by using perovskite materials, CZTS, and quantum dots (QDs) [17]. The photoabsorbing materials were attracting the attention of the researchers due to the well-optimum band-gap (1-1.8 eV), high absorption coefficient ($>10^4 \text{ cm}^{-1}$), and earth availability of elements [18-20]. Till now, various photoabsorbing materials have been used for solar cell applications like amorphous and crystalline Si, CdS, CdTe, CIS_2 , GaInP, GaAs, etc. i.e., group VI elements chalcogenides [21,22]. Whereas, after CIGS the problem of scarcity was resolved by replacing In and Ga to form a CZTS. The CZTS-based TFSC device shows maximum efficiency of about 12.6 % [23], which was saturated over this due to defects observed in the material. Also, various synthesis techniques have been used for the enhancement of the physico-chemical properties of the materials that would help to enhance the performance of solar cell devices. The physical methods like sputtering and evaporation techniques, and chemical methods like sol-gel, chemical bath deposition, spray pyrolysis, electrodeposition, and chemical vapor deposition methods will be used to deposit good quality thin films for photovoltaic applications [24]. Among these, the spray pyrolysis method has great attention in the field of photovoltaic application due to its easy synthesis method, application for large area deposition, more adherence, and compactness of thin films that are

beneficent for charge carriers flow for a long distance without recombination that improves the optoelectrical properties of the device [25]. Whereas, thin films deposited from the spray pyrolysis method was applicable for photovoltaic application [26], photocatalysis [27], gas sensor [28], memristor [29], hydrogen and oxygen evolution reaction [30], supercapacitor and battery applications [31], etc. The versatility of the spray pyrolysis method for a variety of material synthesis is shown in **Figure-1**.

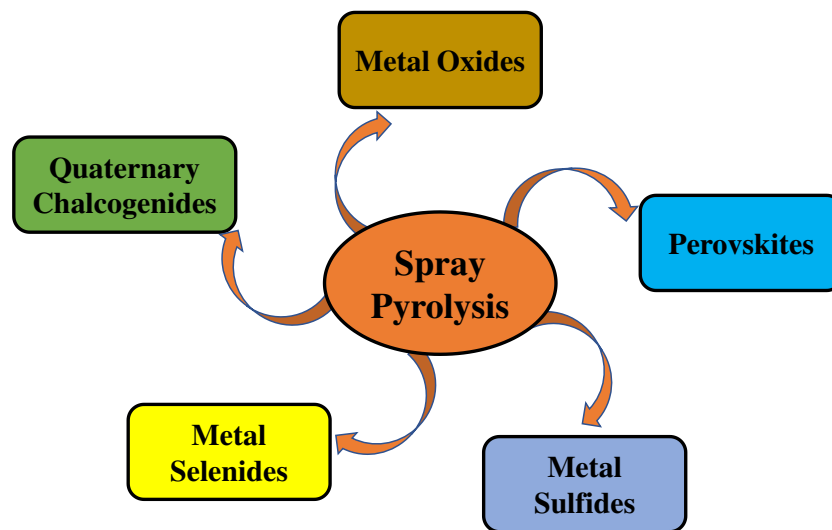


Figure-1. The versatility of the spray pyrolysis method.

In this review, we discussed some basics about solar cells and their parameters that will be used for the material characterization of the photovoltaic study. Also, it includes the significance of all the parameters that will enhance the device's performance is discussed. Also, the recent progress on thin film solar cells and the materials that are applicable to enhance the efficiency of devices are discussed shortly.

2. SOLAR CELL PARAMETERS

Characteristics of the solar cell can be studied with the help of solar cell parameters that can be helpful to investigate the performance of the solar cell devices. The solar cell is a p-n junction diode that works on the photovoltaic effect [32]. Which can convert one form of energy into another form. Most of the parameters that affect the photovoltaic performance of devices include short circuit current (I_{sc}), open circuit voltage (V_{oc}), fill factor (FF), efficiency ($\eta\%$), etc. The p-n junction in the dark represents the current-voltage dependance in Equation-1 and after light illumination, as shown in equation (2) the light-generated current start flowing through the junction which is greater than the diode current [33].

$$I = I_0 e^{qV/nKT} - 1 \dots\dots\dots (1)$$

After light illumination, the current flowing through the p-n junction is given as [34]:

$$I = I_0 (e^{qV/nKT} - 1) - I_L \dots\dots\dots (2)$$

2.1 Short Circuit Current (J_{sc})

The short circuit current (I_{sc}) is the maximum current flowing through the device that is short when $V=0$ i.e., $I=I_{sc}$ when $V=0$. That widely depends on the band gap (E_g) of the photoabsorbing material that is directly proportional to the intensity of light [35]. The band gap decreases which leads to an increase in the I_{sc} of the device. As, $E_g \uparrow$ $I_{sc} \downarrow$, and vice versa.

2.2 Open Circuit Voltage (V_{oc})

The maximum voltage flowing through the circuit when the current is zero i.e., $V=V_{oc}$ when $I=0$. The V_{oc} can be expressed in Equation-3 [36].

$$V_{oc} = \frac{KT}{q} \ln \left(\frac{I_{sc}}{I_0} + 1 \right) \dots\dots\dots (3)$$

As V_{oc} is dependent on the I_{sc} , I_0 , and T . Whereas, the upper limit of V_{oc} is the band gap of the photoabsorbing material ($V_{oc} \leq E_g$).

2.3 Fill Factor (FF)

The fill factor confirms how ideally the diode formation takes place in the solar cell. Ideally, the FF curve measures the squareness of the curve. The ideal value of FF is 1. Most of the good solar cell devices have FF values close to the unity. It is expressed in Equation-4 below [37].

$$FF = \frac{I_{sc}V_{oc}}{I_mV_m} \dots\dots\dots (4)$$

It is the ratio of output power to the maximum power of the solar cell device.

2.4 Efficiency ($\eta\%$)

The efficiency of the solar cell device is the maximum power output extracted from the device to the input power. The efficiency is the maximum power ($I_{sc}V_{oc}FF$) to the input power. So, the formula for the efficiency of solar cells is given in Equation-5 below [38]. The performance was tested under AM 1.5 spectrum of the input power density of 1000 W/m^2 .

$$\eta\% = \frac{I_m V_m}{P_{in}} = \frac{I_{sc} V_{oc} FF}{P_{in}} \dots\dots\dots (5)$$

where, P_{in} = No. of solar cells \times Area of solar cells \times Intensity of light

These are the major four parameters of a solar cell that need to be studied for the photovoltaic study of the device. Recently, the TFSC has attracted the researcher's attention due to its low material consumption and comparable low device cost with high efficiency. Some of the materials used for TFSC were listed below.

3. SOLAR CELL MATERIALS

The different materials have been synthesized for TFSC application in various device structures. Here we have discussed some materials that were used to fabricate the device structures for energy conversion. We discussed the binary, ternary, and quaternary materials with their oxide, sulfide, selenide, telluride, and nitride phases of the material that have been widely used in TFSC. The solar cell device structure and parameters were reported in **Table-1**.

Table-1. Solar cell materials by spray pyrolysis method.

Material	Precursors	Device Structure	Solar cell parameters				Ref.
			I_{sc}	V_{oc} (V)	FF (%)	η (%)	
Cu ₂ O	0.1 M [Cu (CO ₂ CH ₃) ₂ .H ₂ O], 0.1 M C ₆ H ₁₂ O ₆ , 10 ml distilled water, 20 vol% 2-propanol.	Glass/FTO/ ZnO/Cu ₂ O/ Ag	9.91 $\times 10^{-5}$ A	0.37	39.0	0.57	[43]
CuO	0.1 M Cu (NO ₃) ₂ .3H ₂ O, Distilled water	n-CuO/p-Si	22 μ A/c m ²	0.0073	77.0	1.24 $\times 10^{-4}$	[44]
CdO	Cd(CH ₃ COO) ₂ .2H ₂ O, 100 ml distilled water, HCl.	CdO/p-Si/Ag	5.90 mA/c m ²	0.429	32.0	0.8	[45]

Cu ₂ O	0.02 M copper acetate monohydrate, 0.02 M D-glucose.	FTO/TiO ₂ /Cu ₂ O	0.9 mA/cm ²	0.365	47.0	-	[46]
Ag doped PbS	PbNO ₃ , AgNO ₃ , thiourea, 10 ml water	FTO/CdS/Ag-PbS/Ag	283 μA	0.267	30.0	0.89	[48]
Cu doped PbS	PbNO ₃ , thiourea, Cu source, 10 ml water.	FTO/CdS/PbS/Ag	267 μA	0.20	32.0	0.68	[49]
Sb ₂ S ₃	30 mM SbCl ₃ , SC (NH ₂) ₂ , methanolic	ITO/TiO ₂ /Sb ₂ S ₃ /P ₃ HT/Au	13.8 mA/cm ²	0.693	58.0	5.53	[50]
CuInS ₂ & In ₂ S ₃	CuCl ₂ , InCl ₃ , NH ₂ CSNH ₂	Mo/CuInS ₂ /In ₂ S ₃ /ZnO/AZO-Ag-AZO/Ni/Al	43.9 mA/cm ²	0.420	31.0	4.19	[51]
CuSbS ₂	9.6 mM/L CuCl ₂ ·2H ₂ O, 28.3 mM/L SbCl ₃ , 150 mM/L tartaric acid	Mo/CuSbS ₂ /CdS/ZnO/ZnO:Al/Ag device	4.63 mA/cm ²	0.193	36.9	0.33	[52]
CuZnS	0.01 M CuCl ₂ ·2H ₂ O, 0.01 M ZnCl ₂ , (NH ₄) ₂ CS, 100 ml distilled water	ITO/AZO/i-ZnO/CZS/Al	4.97 mA/cm ²	0.505	64.28	1.6	[53]
Cu ₂ SnS ₃	Copper chloride, tin chloride, thiourea, distilled water.	Cu ₂ SnS ₃ solar cell	20.2 μA/cm ²	0.0126	26.0	-	[54]

MASnBr ₃	0.085 g MABr, 0.21 g SnBr ₂ , 7 ml DMF	Glass/FTO/ TiO ₂ /MAS nBr ₃ /P ₃ HT/ Ag	0.46 mA/c m ²	0.37	57.0	0.09 7	[59]
CdSe and Al-doped CdSe	0.01 M (CH ₃ COO) ₂ .C d. ₂ H ₂ O, CSe(NH ₂) ₂	CdSe Al:CdSe	0.87 2 mA 1.08 mA	0.25 0.35	20.8 25.0	0.18 0.38	[61]
SnSe	40 ml methanol, 0.30 g of 1, 1- dimethyl-2- Selenourea, 0.45 g SnCl ₂	Mo/SnSe/C dS/ZnO/Zn O: Al	1.67 mA/c m ²	0.086	25.0	-	[63]
Cu(In,Ga)(S, Se) ₂	0.2 M CuCl ₂ .2H ₂ O, 0.2 M InCl ₃ , 0.2 M GaCl ₃ , 1 M SC(NH ₂) ₂	Cu(In,Ga)(S,Se) ₂ solar cell	24.2 9 mA/c m ²	0.621	69.84	10.5 4	[64]
CuIn(S,Se) ₂	0.1M CuCl ₂ , 0.1M InCl ₃ , 1.0 M thiourea	Mo/MoSe ₂ / CISSe/CdS /ZnO/ITO	25.4 8 mA/c m ²	0.418	55.0	5.91	[65]
Cu(In,Ga)(S, Se) ₂	0.09 M Cu(NO ₃) ₂ , 0.07 M In(NO ₃) ₂ , 0.03 M Ga(NO ₃) ₂ , 0.8 M thiourea.	Mo/CIGSS e/CdS/ZnO /Al:ZnO	25 mA/c m ²	0.62	63.0	10.0	[66]

Cu ₂ ZnSnS ₄	0.009 M cupric chloride, 0.0045 M zinc acetate, 0.005 M stannic chloride, 0.05 M thiourea.	Metal contact/ CZTS/CdS/ ZnO:Al/ glass	0.8 mA/c m ²	0.14	-	-	[68]
Cu ₂ ZnSnS ₄	0.013 to 0.021 M Cu(NO ₃) ₂ , 0.0115 M Zn(NO ₃) ₂ , 0.0115 M Sn(CH ₃ SO ₃) ₂ , 0.05 M thiourea	ITO/ZnO/CdS/CZTS/ Mo/glass	20.0 mA/c 7 m ²	0.67	61.0	8.1	[69]
Cu ₂ CoSnS ₄	CuCl ₂ .2H ₂ O (0.1 M), CoCl ₂ .6H ₂ O (0.05 M), SnCl ₄ .5H ₂ O (0.05 M), CH ₄ N ₂ CS (0.4 M), citric acid (0.2 M)	ITO/CdS/CCTS:CQD/ Al	1.1 mA/c m ²	0.24	26.0	0.07	[72]
Cu ₂ CoSnS ₄	0.05 M CuCl ₂ .2H ₂ O, 0.025 M CoCl ₂ .6H ₂ O, 0.025 M SnCl ₄ .5H ₂ O, 10 mL methanol, CH ₄ N ₂ S	CCTS PEC solar cell	29 μA/c m ²	0.151	32.0	2.33	[73]
Cu ₂ NiSnS ₄	0.1 M copper nitrate dehydrate, 0.05 M nickel nitrate dehydrate, 0.05 M stannic	Ag/n-Si/CNTS/Au	9.1 mA/c m ²	0.41	53.0	11.3 4	[74]

	chloride dehydrate, 0.2 M thiourea.							
Cu ₂ ZnGeS ₄	0.12 M CuCl ₂ .2H ₂ O, 0.06 M Zn(CH ₃ COO) ₂ .2H ₂ O, 0.06 M GeCl ₄ , 0.24 M thiourea.	Al/Cu ₂ ZnGeS ₄ /n-Si/Au	16.2 5 mA/cm ² m ²	0.536	38.0	3.3	[75]	

3.1 Metal Oxides

Recently, metal oxides have great attention in photocatalysis, energy storage and conversion devices, gas sensors, solar cells, batteries, and optoelectronic devices [39,40]. A variety of metal oxides (MO) were used in a TFSC viz. CuO, Co₃O₄, Cu₂O, NiO₂, MnO₂, ZnO TiO₂, etc. as an absorbing and window layer [41]. The MO has a band gap in the range of 1.1-3.7 eV [42]. Prabhu et al. [43] fabricated the heterojunction of two oxide layers of Cu₂O with ZnO by spray pyrolysis method. The cubic crystal structure of spray-deposited Cu₂O thin film shows a cubic crystal structure. The fabricated with the device structure of glass/FTO/ZnO/Cu₂O/Ag. The heterojunction devices show a power conversion efficiency of about 0.57%. Whereas, the study of the annealing effect on spray-deposited CuO thin films enhances the optoelectrical properties of the material at 400, 500, and 600°C. They fabricated the heterojunction solar cell device by spraying CuO on a p-si substrate at 600°C i.e., CuO/p-Si which reported a conversion efficiency 1.24×10^{-4} % [44]. Similarly, Ramamurthy et al. [45] fabricated the same heterojunction device by using CdO spray deposited thin film at 400°C on a p-Si. The device with Al/n-CdO/p-Si/Al electrode device resulted in a power conversion efficiency of 0.8% with FF of 0.32, I_{sc} of 5.90 mA/cm², and V_{oc} of 0.42 V. Also, SnO₂ and TiO₂ are used for solar cell applications. In which TiO₂ was used as a buffer layer. The spray deposition temperature was 560 and 520°C for TiO₂ and SnO₂ thin films. The fabricated device shows an efficiency of 9.3%. The heterojunction formed with Cu₂O and TiO₂ with 0.5% of Mg doping in the Cu₂O thin film that is used for solar cell devices [46].

3.2 Metal Sulfides

Metal Sulfides with the appropriate band gap and good absorption coefficient are also used for photovoltaic applications. Most of the binary, ternary, and quaternary sulfide materials like CdS, SnS, PbS, In₂S₃, Sb₂S₃, CuInS₂, CuSbS₂, etc. Generally, the band gap of sulfides varies between 1.0 to 3.6 eV [47]. The spray-deposited PbS

thin film at 200°C was used for the fabrication of a heterostructure thin film device having the structure of FTO/CdS/PbS/Ag. They varied the percentage of Ag doping in a pure PbS. The 6% of Ag doping in PbS in a fabricated device shows a conversion efficiency of 0.89%, also 6% Cu doping in PbS enhances the properties of the fabricated FTO/ CdS/ Cu:PbS/ Ag heterostructure solar cell efficiency [48,49]. The Sb₂S₃ material becomes the suitable material due to the 1.7 eV band gap, and high absorption coefficient >10⁵ cm⁻¹, the hybrid solar cell with structure ITO/TiO₂/Sb₂S₃/P₃HT/Au reported a 5.5% efficiency [50]. Like the CIGS, CuInS₂ attracts more attention due to its similar physico-chemical properties. The device was fabricated with the structure of Mo/CuInS₂/In₂S₃/ZnO/AZO-Ag-AZO/Ni/Al in which metal sulfides were deposited by spray pyrolysis technique. The fabricated device exhibits a conversion efficiency of 4.19%, I_{sc} of 43.92 mA/cm², V_{oc} of 0.42 V, and FF of 31% [51]. The solar cell device with spray deposited CuSbS₂ thin films at 290°C with the Mo/CuSbS₂/CdS/ZnO/ZnO:Al/Ag device structure of 0.34% [52]. Similarly, the CuZnS thin films are deposited by temperature variation in the spray pyrolysis technique. They fabricated the device of CZTS at 350°C having a structure with ITO/AZO/i-ZnO/CZS/Al reported the solar cell parameters as I_{sc}, V_{oc}, FF, and efficiency of 4.97 mA/cm², 0.505 V, 64.28%, and 1.6% respectively [53]. Mostly, Cu₂SnS₃ (CTS) has largely been used for the TFSC application that spray pyrolysis synthesized CTS thin films with fabricated solar cell device of glass/FTO/CTS/CdS/Al:ZnO/Al structure that results in solar cell application [54].

3.3 Perovskites

Perovskite materials that have the same optoelectrical properties that can be useful for solar cell applications. It shows low trap centers, excellent charge transfer characteristics, and large diffusion lengths, which made them suitable for photo absorption [55]. Recently, metal halide perovskites have great attention in PSCs energy devices [56]. Bartholazzi et al. [57] reported the formation of CH₃NH₃PbI₃ thin film by spray pyrolysis method at 60-140°C substrate temperatures. Sn-based perovskites have large attention due to the toxicity issue in Pb perovskite materials [58]. This layer can be synthesized by the spray pyrolysis method and was reported by Kaleli et al. [59]. They fabricated the PSCs by using the ultrasonic spray pyrolysis method MASnBr₃ thin film at 180°C. the fabricated device with structure glass/FTO/TiO₂/MASnBr₃/P₃HT/Ag shows 0.46 mA/cm² of I_{sc}, 0.370 V of V_{oc}, 57.2% of FF, and 0.097% of efficiency.

3.4 Metal Selenides

Metal selenides were also have been used for solar cells due to their appropriate band gap, high absorption coefficient, and good stability of the materials. The Sb₂Se₃ semiconducting material with optimum band gap~1.03-1.17 eV, simple phase, less toxicity, and elemental abundance on earth made it suitable for solar cell application

[60]. Gawali et al. [61] reported the photoelectrochemical study of spray deposited CdSe thin films at temperature ranging from 200-300°C with spray rate of 2.5 ml/min. The as deposited and Al doped thin films were tested in a photoelectrochemical solar cell with configuration of CdSe or Al:CdSe/1 M (Na₂S–S–NaOH)/C. the Al-doped CdSe showed the maximum conversion efficiency than that of pure CdSe solar cell. The enhancement in the efficiency was found to be 0.38% after Al-doping in CdSe. Also, Fadavieslam et al. [62] studied the effect of Se concentration on SnSe thin films deposited by spray pyrolysis method. The deposition was carried out at 470°C substrate temperature. Whereas, Rios et al. [63] successfully fabricated the SnSe based solar cells with structure Mo/SnSe/ZnO/ZnO:Al, Mo/SnSe/CdS/ZnO:Al, and Mo/SnSe/CdS/ZnO/ZnO: Al that reported the J_{sc} of 1.67 mA/cm², V_{oc} of 0.086 V, and FF of 0.25. Quaternary selenides have also emerged as the best promising materials that improve device efficiency beyond 10%. The spray-deposited CIGSSe thin films between 300-350°C were used for good quality deposition of thin films. The device with CIGSSe structure as Mo/CIGSSe/CdS/i-ZnO/AZO reported an efficiency with an antireflecting coating of 10.54% [64]. Also, Ho et al. [65] deposited the CuIn(S,Se)₂ thin film by spray pyrolysis method at 300-350°C substrate temperature. The CISSe device was fabricated that showed a PCE of about 5.91% with J_{sc} of 25.48 mA/cm², V_{oc} of 0.418 V, and FF of 55.0%. Whereas, Na-doping in a sulfide precursor film can enhance the solar cell performance by about 10.7% [66].

3.5 Quaternary Chalcogenides

Quaternary chalcogenides were also been popularized as a photoabsorbing material. The CZTS material has great attention in the past few years due to its similar physico-chemical properties to CIGS [67]. Kumar et al. [68] tried to fabricate the heterojunction device structure with metal contact/CZTS/CdS/ZnO:Al/glass substrate that reports low performance. Nguyen et al. [69] synthesized the CZTS thin film by spray method. They fabricated the TFSC device with ITO/ZnO/CdS/CZTS/Mo/glass structure that reported an 8% solar conversion efficiency of 20.07 mA/cm² of I_{sc} , 0.67 V of V_{oc} , and 61% of FF. Also, the saturation occurred in the CZTS TFSC, most of the researchers over the world will synthesize the different copper-based quaternary chalcogenides to increase the efficiency of fabricated solar cell devices. In which Zn was replaced by the Fe, Co, Ni, etc. elements to form CFTS, CCTS, and CNTS-like materials which can be used as a promising photovoltaic material in solar cells [70]. Prabhakar et al. [71], used the spray pyrolysis method to deposit the CFTS thin film for the counter electrode (CE) in DSSC shows a PCE of about 8.03%. However, Shivagami et al. [72] reported the CCTS thin films were deposited at 170°C as pure and with carbon-based quantum dots (CQD). The fabricated ITO/CdS/CCTS:CQD/Al device showed 0.07% efficiency than that of a pure device. Maldar et al. [73] also synthesized the CCTS thin films for PEC solar cells and

showed an efficiency of 2.33%. The CNTS material also has been synthesized by the spray pyrolysis method, Elsaedy et al. [74] fabricated the CNTS/n-si heterojunction device. In which spray deposited CNTS thin film taken at 350°C on si substrate. The device shows 11.34% conversion efficiency with J_{sc} 9.51 mA/cm², V_{oc} of 0.56 V, and FF of 53.0%. Radaf et al. [75] also reported the Cu₂ZnGeS₄ thin film was synthesized by the spray pyrolysis method. The film was sprayed on the n-si substrate to form a heterojunction thin film device with the structure of Al/n-si/Cu₂ZnGeS₄/Au which reports an efficiency of about 3.3% under 100 mW/cm² light illumination.

4. CONCLUSION

The spray pyrolysis method is a clean, low cost applicable for large-area deposition of thin films. Thin films synthesized from this method is used for various applications including photovoltaic application. The basic parameters of solar cells include short circuit current, open circuit voltage, fill factor, and efficiency. The synthesized materials for solar cell applications like metal oxides, metal sulfides, metal nitrides, metal selenides, and quaternary chalcogenides that discussed in this review. This review focuses on the different materials synthesized by the spray pyrolysis method that will be applicable for solar cell application. The spray pyrolysis method is a low-cost, easy synthesis process that can be applicable for large areas, compact with a uniform thickness which can be applied for solar cell application. In thin film solar cells (TFSC), different layers were applicable to absorb the light spectrum of different wavelengths that will be easily deposited by this technique with varying film thickness. In TFSCs, the layers like metal oxides were used as a window layer to absorb the high energy radiations. As well as, different metal sulfides, selenides, chalcogenides, and perovskites were easily deposited by this method in a large area with less material consumption. That helps to reduce the device fabrication costs due to less material consumption with better efficiency. Also, the easy and low-cost technique is used to fabricate transparent and more efficient devices that impact environmental remediation for CO₂ reduction.

ACKNOWLEDGMENT

All Authors are thankful to UGC-DSA Phase II (2018-2023) and DST-PURSE Phase-II (2018-2023) Department of Physics, Shivaji University, Kolhapur (M.S.), India.

REFERENCES

1. Hayat, M. B., Ali, D., Monyake, K. C., Alagha, L., Ahmed, N. (2019) International Journal of Energy Research, 43, 1049-1067.

2. Firfiris, V. K., Fragos, V. P., Kotsopoulos, T. A., Nikita-Martzopoulou, C. (2020) *Sustainable Energy Technologies and Assessments*, 40, 100750.
3. Tjong, V. T., Wang, H. (2020) *Responsive Nanomaterials for Sustainable Applications*, 1-63.
4. Yan, N., Zhao, C., You, S., Zhang, Y., Li, W. (2020) *Chinese Chemical Letters*, 31, 643-653.
5. Cole, J. M., Pepe, G., Al Bahri, O. K., Cooper, C. B. (2019) *Chemical Reviews*, 119, 7279-7327.
6. Rong, Y., Hu, Y., Mei, A., Tan, H., Saidaminov, M. I., Seok, S., McGehee, M. D., Sargent, E. H., Han, H. (2018) *Science*, 361, eaat8235.
7. Philipps, S. P., Dimroth, F., Bett, A. W. (2018) In *McEvoy's handbook of photovoltaics*, 439-472.
8. Wohrle, D., Meissner, D. (1991) *Advanced Materials*, 3, 129-138.
9. Chopra, K. L., Das, S. R. (1983) *Thin film solar cells*, 1-18.
10. Andreani, L. C., Bozzola, A., Kowalczewski, P., Liscidini, M., Redorici, L. (2019) *Advances in Physics: X*, 4, 1548305.
11. Sopian, K., Cheow, S. L., Zaidi, S. H. (2017) In *AIP Conference Proceedings*, 1877, 020004.
12. Powalla, M., Paetel, S., Ahlswede, E., Wuerz, R., Wessendorf, C. D., Friedlmeier, T. M. (2018) *Applied Physics Reviews*, 5, 041602.
13. Ramanujam, J., Singh, U. P. (2017) *Energy & Environmental Science*, 10, 1306-1319.
14. Ramanujam, J., Bishop, D. M., Todorov, T. K., Gunawan, O., Rath, J., Nekovei, R., Artegiani, E., Romeo, A. (2020) *Progress in Materials Science*, 110, 100619.
15. Aberle, A. G. (2009) *Thin solid films*, 517, 4706-4710.
16. Chopra, K. L., Paulson, P. D., Dutta, V. (2004) *Progress in Photovoltaics: Research and applications*, 12, 69-92.
17. Lee, T. D., Ebong, A. U. (2017) *Renewable and Sustainable Energy Reviews*, 70, 1286-1297.
18. Sutherland, B. R. (2020) *Joule*, 4, 984-985.
19. Chen, E. M., Williams, L., Olvera, A., Zhang, C., Zhang, M., Shi, G., Heron, J. T., Qi, L., Guo, L. J., Kioupakis, E., Poudeu, P. F. (2018) *Chemical Science*, 9, 5405-5414.
20. Kherodia, A., Bathija, R. (2019) *International Journal of Scientific & Engineering Research Volume*, 10.
21. Green, M. A. (2007) *Journal of Materials Science: Materials in Electronics*, 18, 15-19.
22. Jilani, A., Abdel-Wahab, M. S., Hammad, A. H. (2017) *Modern Technologies for Creating the Thin-film Systems and Coatings*, 2, 137-149.

23. Wang, W., Winkler, M. T., Gunawan, O., Gokmen, T., Todorov, T. K., Zhu, Y., Mitzi, D. B. (2014) *Advanced Energy Materials*, 4, 1301465.
24. Perednis, D., Gauckler, L. J. (2005) *Journal of Electroceramics*, 14, 103-111.
25. Riverola, A., Vossier, A., Chemisana, D. (2019) In *Nanomaterials for Solar Cell Applications*, 3-33.
26. Tomar, M. S., Garcia, F. J. (1981) *Progress in Crystal Growth and Characterization*, 4, 221-248.
27. Di Mauro, A., Fragala, M. E., Privitera, V., Impellizzeri, G. (2017) *Materials Science in Semiconductor Processing*, 69, 44-51.
28. Patil, S. P., Patil, V. L., Shendage, S. S., Harale, N. S., Vanalakar, S. A., Kim, J. H., Patil, P. S. (2016) *Ceramics International*, 42, 16160-16168.
29. Singh, R., Kumar, M., Iqbal, S., Kang, H., Park, J. Y., Seo, H. (2021) *Applied Surface Science*, 536, 147738.
30. Freeman, E., Kumar, S., Thomas, S. R., Pickering, H., Fermin, D. J., Eslava, S. (2020) *ChemElectroChem*, 7, 1365-1372.
31. Leng, J., Wang, Z., Wang, J., Wu, H. H., Yan, G., Li, X., Guo, H., Liu, Y., Zhag, Q., Guo, Z. (2019) *Chemical Society Reviews*, 48, 3015-3072.
32. Kodati, R. B., Rao, P. N. (2020) *Advanced Science letters*, 26.
33. Saive, R. (2019) *IEEE Journal of Photovoltaics*, 9, 1477-1484.
34. Munshi, A. H., Kephart, J., Abbas, A., Raguse, J., Beaudry, J. N., Barth, K., Sites, J., Walls J., Sampath, W. (2017) *IEEE Journal of Photovoltaics*, 8, 310-314.
35. Brendel, R., Queisser, H. J. (1993) *Solar Energy Materials and Solar Cells*, 29, 397-401.
36. Richhariya, G., Kumar, A., Tekasakul, P., Gupta, B. (2017) *Renewable and Sustainable Energy Reviews*, 69, 705-718.
37. Gao, F. (2019) In *Advanced Nanomaterials for Solar Cells and Light Emitting Diodes*, edited by Feng, G., pp.1-33.
38. Chavali, M. S., Nikolova, M. P. (2019) *SN applied sciences*, 1, 607.
39. Nunes, D., Pimentel, A., Gonçalves, A., Pereira, S., Branquinho, R., Barquinha, P., Fortunato, E., Martins, R. (2019) *Semiconductor Science and Technology*, 34, 043001.
40. Mei, J., Liao, T., Kou, L., Sun, Z. (2017) *Advanced Materials*, 29, 1700176.
41. Hassan, Z., Saheed, M. S. M., Yusof, A. S. (2019) In *2019 International Energy and Sustainability Conference (IESC)*, 1-5.
42. Lany, S. (2015) *Journal of Physics: Condensed Matter*, 27, 283203.
43. Prabu, R. D., Valanarasu, S., Ganesh, V., Shkir, M., Kathalingam, A., AlFaify, S. (2018) *Surface and Coatings Technology*, 347, 164-172.
44. Hussain, A. N., Hassoon, K. I., Hassan, M. A. (2020) In *Journal of Physics: Conference Series*, 1530, 012140.

45. Ramamurthy, M., Balaji, M., Thirunavukkarasu, P. (2016) *Optik*, 127, 3809-3819.
46. Kardarian, K., Nunes, D., Sberna, P. M., Ginsburg, A., Keller, D. A., Pinto, J. V., Deuermeier, J., Anderson, A. Y., Zaban, A., Martins, R., Fortunato, E. (2016) *Solar Energy Materials and Solar Cells*, 147, 27-36.
47. Boldish, S. I., White, W. B. (1998) *American Mineralogist*, 83, 865-871.
48. Rosario, S. R., Kulandaisamy, I., Kumar, K. D. A., Ramesh, K., Ibrahim, H. A., Awwad, N. S. (2020) *International Journal of Energy Research*, 44, 4505-4515.
49. Rosario, S. R., Kulandaisamy, I., Arulanantham, A. M. S., Valanarasu, S., Hamdy, M. S., Al-Namshah, K. S., Alhanash, A. M. (2019) *Materials Research Express*, 6, 056201.
50. Eensalu, J. S., Katerski, A., Kärber, E., Weinhardt, L., Blum, M., Heske, C., Yang, W., Acik, I. O., Krunk, M. (2019) *Beilstein Journal of Nanotechnology*, 10, 2396-2409.
51. Aydin, E., Sankir, N. D. (2018) *Thin Solid Films*, 653, 29-36.
52. Wan, L., Guo, X., Fang, Y., Mao, X., Guo, H., Xu, J., Zhou, R. (2019) *J. Journal of Materials Science: Materials in Electronics*, 30, 21485-21494.
53. Aabel, P., Kumar, M. S. (2020) *International Journal of Energy Research*, 44, 7778-7788.
54. Patel, B., Waldiya, M., Pati, R. K., Mukhopadhyay, I., Ray, A. (2018) In *AIP Conference Proceedings*, 1953, 100079.
55. Tonui, P., Oseni, S. O., Sharma, G., Yan, Q., Mola, G. T. (2018) *Renewable and Sustainable Energy Reviews*, 91, 1025-1044.
56. Zhang, W., Eperon, G. E., Snaith, H. J. (2016) *Nature Energy*, 1, 1-8.
57. Bartholazzi, G., Pereira, R. P., Lima, A. M., Pinheiro, W. A., Cruz, L. R. (2020) *Journal of Materials Research and Technology*, 9, 3411-3417.
58. Ghosh, S., Pradhan, B. (2019) *ChemNanoMat*, 5, 300-312.
59. Kaleli, M., Şen, E., Lapa, H. E., Aldemir, D. A. (2022) *Physica B: Condensed Matter*, 645, 414293.
60. Lu, S., Zhao, Y., Chen, C., Zhou, Y., Li, D., Li, K., Chen, W., Wen, X., Wang, C., Kondrotas, R., Lowe, N., Tang, J. (2018) *Advanced Electronic Materials*, 4, 1700329.
61. Gawali, S. A., Bhosale, C. H. (2011) *Materials chemistry and physics*, 129, 751-755.
62. Fadavieslam, M. R., Bagheri-Mohagheghi, M. M. (2013) *Journal of Semiconductors*, 34, 082001.
63. Narro-Rios, J. S., Martinez-Escobar, D., Sanchez-Juarez, A. (2018) In *2018 15th International Conference on Electrical Engineering, Computing Science and Automatic Control (CCE)*, 1-5.

64. Hossain, M. A., Tianliang, Z., Keat, L. K., Xianglin, L., Prabhakar, R. R., Batabyal, S. K., Mhaisalkar, S. G., Wong, L. H. (2015) *Journal of Materials Chemistry A*, 3, 4147-4154.
65. Ho, J. C., Zhang, T., Lee, K. K., Batabyal, S. K., Tok, A. I., Wong, L. H. (2014) *ACS Applied Materials & Interfaces*, 6, 6638-6643.
66. Septina, W., Kurihara, M., Ikeda, S., Nakajima, Y., Hirano, T., Kawasaki, Y., Harada, T., Matsumura, M. (2015) *ACS Applied Materials & Interfaces*, 7, 6472-6479.
67. Jiang, M., Yan, X. (2013) *Solar Cells-Research and Application Perspectives*, 388.
68. Kumar, Y. K., Raja, V. S. (2017) *Surfaces and Interfaces*, 9, 233-237.
69. Nguyen, T. H., Harada, T., Nakanishi, S., Ikeda, S. (2016) In *2016 IEEE 43rd Photovoltaic Specialists Conference*, 0470-0472.
70. Kumar, M. S., Madhusudanan, S. P., Batabyal, S. K. (2018) *Solar Energy Materials and Solar Cells*, 185, 287-299.
71. Prabhakar, R. R., Huu Loc, N., Kumar, M. H., Boix, P. P., Juan, S., John, R. A., Batabyal, S. K., Wong, L. H. (2014) *ACS Applied Materials & Interfaces*, 6, 17661-17667.
72. Sivagami, D., Priyadarshini, B. G. (2022) *Materials Advances*, 3, 2405-2416.
73. Maldar, P. S., Mane, A. A., Nikam, S. S., Dhas, S. D., Moholkar, A. V. (2020). *Thin Solid Films*, 709, 138236.
74. Elsaedy, H. I. (2019) *Journal of Materials Science: Materials in Electronics*, 30, 12545-12554.
75. El Radaf, I. M., Al-Zahrani, H. Y. S. (2020) *Journal of Electronic Materials*, 49, 4843-485.

Chemically Derived Carbon Aerogel Electrodes for Supercapacitors

Ashwini V. Patil^a, Rajiv S. Vhatkar^{a,*}

Department of Physics, Shivaji University, Kolhapur 416 004 (MS) India.

*Corresponding author: drvhatkar@gmail.com

ABSTRACT

The application of carbon-based materials to fabricate supercapacitors is trending. Amongst all carbon-based materials, carbon aerogels grab attention towards them as they have low density, high electrical conductivity, and porosity with abundant meso- and micro-porous 3D interconnected carbon networks. In this paper, we discussed the synthesis method, structural, and morphological characterizations along with the electrochemical study of chemically derived carbon aerogel. Herein, the three-dimensional carbon aerogel synthesized by polycondensation of resorcinol-formaldehyde and dried supercritically in ethanol medium followed by carbonization in nitrogen at 800°C. This prepared carbon aerogel showed interconnected, porous, and pearl chain-like carbon structure confirmed by SEM images. The cost effective and flexible carbon electrode was prepared by coating a carbon aerogel powder on flexible stainless-steel mesh by screen-printing. The as-prepared electrode showed the highest specific capacitance of 113 F/g at 5 mV/s scan rate with 40 second discharge time at 2 mA/cm² current density over 1.9 V wide operating potential window in 1 M Na₂SO₄ electrolyte stability of 80% after 2000 charge-discharge cycles. These electrodes exhibit good charging discharging because of the interconnected and porous structure.

KEYWORDS

Carbon aerogel, Energy storage device, Supercapacitor, Supercritical drying.

.....

1. INTRODUCTION

Supercapacitors (SCs) are more popular than batteries and they are dominating the market. Nowadays SCs perform a variety of functions in daily life, ranging from supplying the initial power necessary to start vehicle engines to serving as a backup source of energy in telecommunications, public transportation, and medical procedures [1]. The batteries and conventional capacitors have constraints in terms of low power and energy density respectively. The high-power density, good energy density, fast charging-discharging time, and excellent cyclic stability over thousands of cycles proved SCs candidature in the field of energy storage. Based on the mode of charge storage SCs are divided into two types i) Electric double-layer capacitors

(EDLCs) and ii) Pseudocapacitors. Mostly, metal oxides (RuO_2 , CuO , and MnO_2) and conducting polymers (polyaniline and polypyrrole) are used to fabricate pseudocapacitors [2]. Carbon-based materials like activated carbon, carbon nanotubes, graphene, and carbon aerogels (CAs) are used to fabricate EDLCs [3].

Amongst, CAs are very promising materials used as an electrode material for SCs due to their 3D interconnected structure, good electrical conductivity (25-100 S/cm), high specific surface area ($\sim 1100 \text{ m}^2/\text{g}$), and porosity (80-98%) with abundance of meso- and micro- porosity and low density [4–6]. The first report on CA electrodes used for charge storage in capacitors was published by Pekla et al [7] using resorcinol-formaldehyde (RF). Carbon aerogels were synthesized by using various precursors like resorcinol – formaldehyde [8], melamine- formaldehyde [9], cresol- formaldehyde [10], phenol–resorcinol–formaldehyde [11], phenolic–furfural [5], melamine–formaldehyde, polyurethanes, and polyureas [7]. The wet gels are transformed into aerogels by supercritical drying, subcritical drying, freeze-drying and ambient drying [12,13]. The obtained organic aerogels are then converted into carbon aerogel by carbonization in an inert atmosphere. The physical/chemical activation is further needed for the better performance of CA to use as an SCs electrode. Which further increased their cost. Hence the fabrication of economical carbon aerogel with abundant functionalities, and hierarchical pore structure is still challenging. Also, the use of as-synthesized CA to fabricate SCs electrodes needs to be focused to reduce further fabrication cost.

In this work, carbon aerogel was synthesized by polycondensation reaction of RF to get hydrogels followed by solvent exchange with ethanol and supercritical drying at 255°C . These RF aerogels are then carbonized at 800°C to get carbon aerogel. The prepared aerogel showed a pearl-like linked structure with plentiful pores. Further, the presence of disordered carbons offers better electrode-electrolyte interactions and surface functional groups which resulted in good supercapacitive performance. The as-prepared low-cost flexible electrodes showed specific capacitance (C_s) of 113 F/g in 1 M Na_2SO_4 electrolyte with a wide potential window of 1.9 V without any further activation.

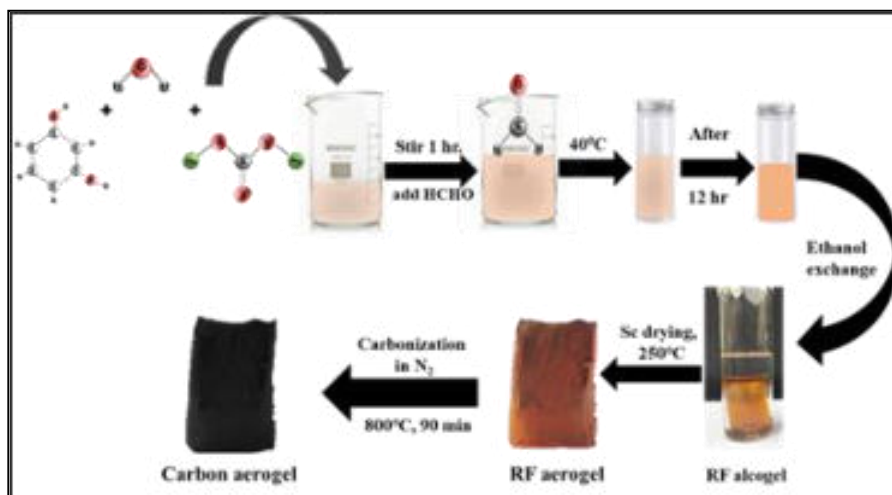
2. EXPERIMENTAL SECTION

2.1. Materials

Resorcinol (R) ($\text{C}_6\text{H}_4(\text{OH})_2$, 99%), Formaldehyde (F) (HCHO , 37% in water), Sodium carbonate (C) (Na_2CO_3 , anhydrous, 99.5%), Ethanol ($\text{C}_2\text{H}_5\text{OH}$, 99.9%) and flexible stainless- steel mesh (FSSM) 300 mesh size used for deposition was purchased from Zain corporation, Pune, India.

2.2. Synthesis of Carbon Aerogel Monolith

The RF hydrogel was prepared by polycondensation reaction of resorcinol and formaldehyde with double distilled water used as a solvent and sodium carbonate (Na_2CO_3) as a catalyst. The wet RF hydrogel was prepared by pouring a solution of resorcinol: formaldehyde: double distilled water: Na_2CO_3 in the molar ratio 1:2:0.47:0.0001 in a cylindrical test tube and kept at 40°C for hydrogel formation.



Schematic-1. Schematic of synthesis of Carbon aerogel.

After 18 hrs the gel is formed and then immersed in ethanol for solvent exchange to exchange the water from the pores of hydrogel with ethanol. After 72 hrs of immersion in ethanol the hydrogel was turned into alcogel at this step water in pores was replaced by alcohol. This RF alcogel was then subjected to supercritical drying in ethanol medium and the system was kept at 255°C with 30-minute hold time. After cooling at room temperature, the RF aerogel was obtained. This RF aerogel was kept in tube furnace for carbonization to get carbon aerogel in N_2 flow at 800°C for 1 hr. Then the furnace was allowed to cool at room temperature and aerogel was labelled as carbon aerogel. **Schematic-1** showed the synthesis route adopted for the synthesis of carbon aerogel.

2.3. Fabrication of Working Electrode

To prepare electrodes for supercapacitor the carbon aerogel block was grind to make powder. The electrode was prepared by screen printing method by mixing carbon aerogel powder, carbon black, and polyvinylidene fluoride in weight ratio 8:1:1 with N-Methyl-2- as a solvent. The slurry was coated on the FSSM and dried for 12hrs at 90°C .

2.4. Characterizations

The structural properties of synthesized carbon aerogel were characterized by X-ray powder diffractometer (XRD, Model: D8. Advance, Bruker Germany), Fourier Transform Infrared (FTIR, Model: PN: 1010948106, Bruker Germany) Spectroscopy, and Raman Spectroscopy (Model: Renishaw INVIA 0120 -20, Renishaw UK). The morphology and elemental analysis of the prepared sample was characterized by Scanning Electron microscopy (SEM, Model: JSM 6360, JEOL Ltd. Japan). The surface wettability study was done by Water contact angle meter.

2.5. Electrochemical Setup

The electrochemical performance of the prepared carbon aerogel electrode was characterized using three electrode system. The carbon aerogel powder screen printed on FSSM used as a working electrode, Platinum as a counter electrode and Saturated Calomel electrode used as a reference electrode. The electrode performance was tested through Cyclic voltammetry (CV), Galvanostatic Charge Discharge (GCD), and Electrochemical Impedance Spectroscopy (EIS) in 1M Na₂SO₄ electrolyte using BioLogic vmp3 potentiostat. Formulae used to calculate specific capacitance from CV and GCD is given below

Specific capacitance from CV [14]

$$C_s = \frac{1}{v(V_2 - V_1)} \int_{V_1}^{V_2} I(V) dV$$

The specific capacitance from charge-discharge curves

$$C_s = \frac{I \Delta t}{m(V_2 - V_1)}$$

Where, C_s = specific Capacitance, I (V)= current (A), v = Potential scan rate (V/s), Δt = discharge time, $V_2 - V_1$ = Potential window (V), m = mass deposited on electrode surface.

3. RESULTS AND DISCUSSION

To confirm the structure of prepared material the XRD study was done. **Figure-1** showed the XRD pattern of prepared carbon aerogel. The two peaks observed at 23° and 44° corresponds to the (002) and (100) planes respectively [14]. The XRD showed amorphous nature of material. The broadening of both peaks depicted the formation of disordered carbon and pointing towards the low degree of graphitization [15]. To study the various functional groups, present in sample FTIR spectroscopy is used.

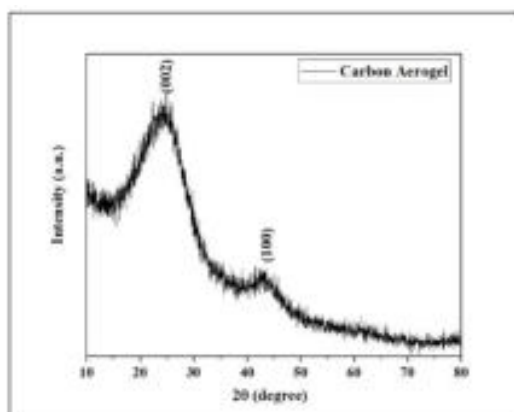


Figure-1. XRD of carbon aerogel.

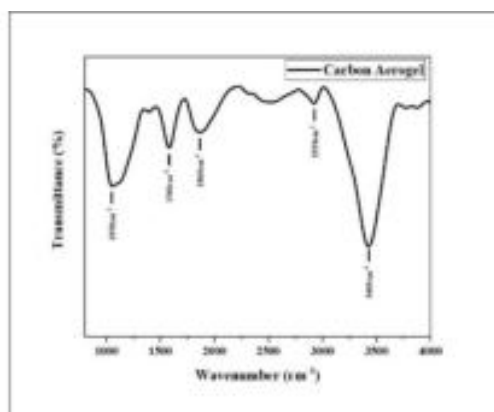


Figure-2. FTIR of carbon aerogel.

The FTIR spectra of prepared carbon aerogel is shown in **Figure-2**. The Peak observed at 1050 cm^{-1} is due to the methylene ether linkage ($\text{CH}_2\text{-O-CH}_2$) formed during polycondensation of resorcinol and formaldehyde [16,17]. The stretching between carbon -carbon is indicated by peak at 1560 cm^{-1} and C=O is the most common peak observed in any carbon -based material present at 1860 cm^{-1} . However, the peak at 2928 cm^{-1} corresponds to the symmetric stretching between C-H present in alkyl groups [18]. The intense and broad peak observed at 3400 cm^{-1} is an indicative of -OH groups. During carbonization the methylene bridge decomposed and form the $\text{CH}_2\text{-OH}$ and CH_2 which is evident of broadening of peak at 3400 cm^{-1} also the surface functional groups like carbonyl, carboxyl groups [19]. The presence of all these functional groups enhances the wettability of material and boosts the ion accession on the surface of electrode which in turn increase the capacitive performance.

The Raman study helped to study the nature of disordered and graphitic carbon present in sample. The two characteristic peaks for carbon material were observed at 1342 and 1586 cm^{-1} corresponds to the D and G band respectively as shown in **Figure-3**. The D band indicate the presence of turbo-static carbons which

are connected to the oxygen based functional groups like carbonyl, carboxyl and hydroxyl groups [20] whereas G band is related to the sp^2 hybridised carbons in structure [21]. The ID/IG ratio of prepared carbon aerogel is 0.99 which is a clear indicative of presence of disordered carbons [6] and well matches with the XRD results showing less degree of graphitization.

In case of supercapacitors the morphology plays a vital role as the charge storage and other faradic reactions took place on the surface of electrode. For EDLC the surface with abundant meso- and micro porous structure with interconnections is very important [14]. The mesopores stored the ions of an electrolyte whereas the micropores provide the short ion diffusion path and reduce the internal resistances [22]. **Figure-4** showed the SEM images of prepared aerogel. The prepared aerogel showed a 3D porous structure with interconnected pearl chain like structure [16]. This porous structure act as a reservoir to electrolyte ions and enhances the performance.

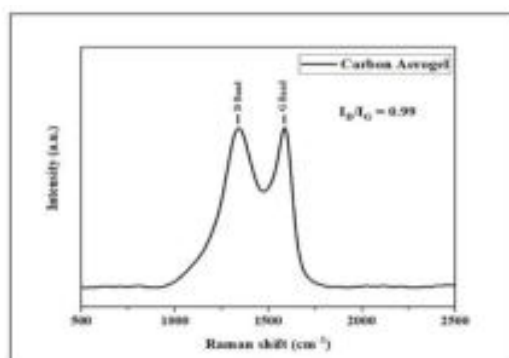


Figure-3. Raman spectra of carbon aerogel.

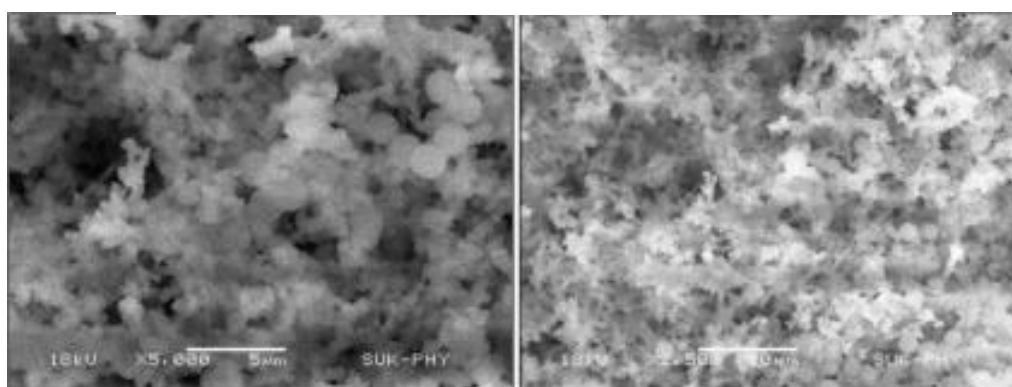
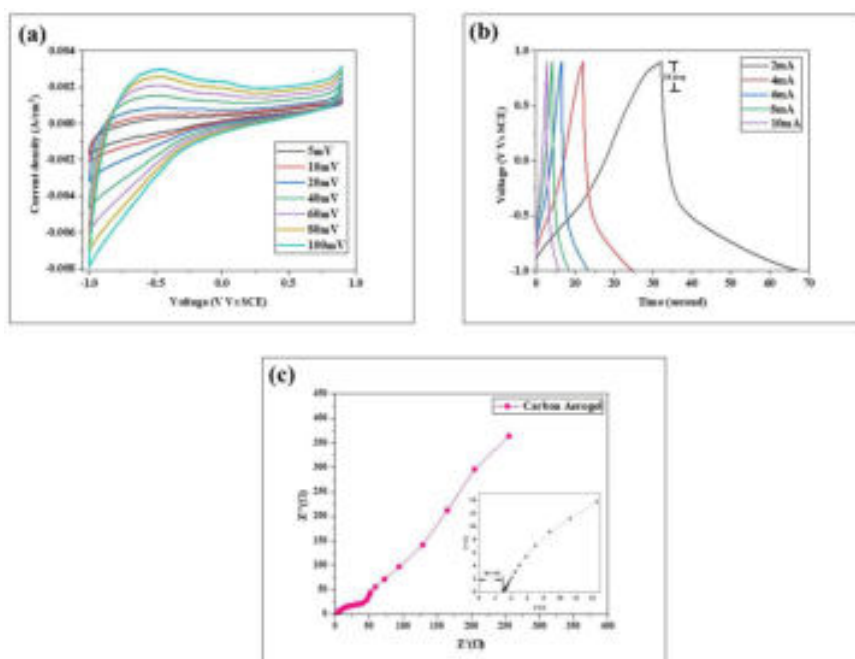


Figure-4. SEM images of carbon aerogel at 5 and 10 μm respectively.

3.1. Electrochemical Performance:

To evaluate the electrochemical behaviour of prepared carbon aerogel electrode the CV, GCD study was done using three electrode system in 1M Na₂SO₄ electrolyte. The use of neutral electrolyte is advantageous over acid or alkaline electrolytes as they worked over large potential window (~2.2V), as well as having low cost and are environmentally friendly than organic electrolytes and ionic liquids [23]. **Figure-5a** showed the CV curves of carbon aerogel over a wide potential window of 1.9V. The shape of curves is quasi rectangular which showed the EDLC behaviour. From CV analysis the highest value of specific capacitance was 113 F/g at 5 mV/s scan rate and for 100 mV/s the capacitance was 30 F/g. With increased scan rate the area under CV curve increased but value of capacitance decreased. This is due to a higher scan rate the electrolyte ions did not get sufficient time to interact with electrode material resulted into lower capacitance value and vice versa.



The GCD curves are shown in **Figure-5b**. The curves are quasi triangular in **Figure -5. a) CV curves of Carbon Aerogel electrode at different scan rates b) GCD curves of Carbon Aerogel electrode at different current densities C) Nyquist plot of Carbon Aerogel electrode.**

nature indicating the fast charge discharge process takes place on surface of carbon electrode surface. For current density of 2mA/cm² the value of capacitance is 80 F/g.

Additionally, the small IR drop (0.3V) also observed in GCD curve suggesting the resistance offered by electrode material. In this range the material did not participate effectively in charging discharging process resulting in poor value of capacitance [24,25]. With increased current density the IR drop also increased indicating that at higher current the material surface was not properly utilized by all electrolyte ions which caused the decrement in capacitance value.

Figure-5c showed the Nyquist plot of as prepared carbon aerogel electrode recorded in frequency range 1mHz to 1MHz. The semicircle appeared at the high frequency region corresponds to the charge transfer resistance (R_{ct}) and the value of R_{ct} is 35 Ω . The initial intercept on X axis is referred as a solution resistance (R_s) and for this electrode the R_s is 3 Ω as shown in inset. The combined effect of these two resistances may cause the decrement in the electrochemical performance of electrode. The steep slope appear in the nonlinear part at intermediate frequency region is an evident of EDLC behavior and showed the resistance offered to bulk electrolyte by porous structure of active material [26].

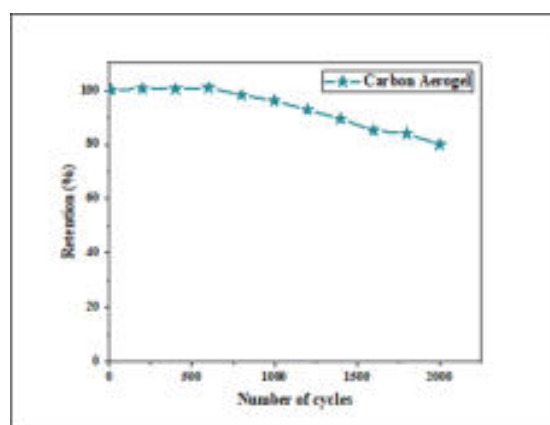


Figure-6. Capacitance retention after 2000 GCD cycles of Carbon Aerogel electrode at 20 mA/cm² current density in 1M Na₂SO₄.

Figure-6 showed the retention in capacitance value of as prepared carbon aerogel electrode after 2000 GCD cycles. The prepared electrode showed good retention of 80% of its initial capacitance value after 2000 cycles. The 4% decrement in capacitance value is observed after 1000 cycles indicating the decreased number of active sites for ion interaction. The further decrement in performance up to 2000 cycles are due to both less ion active sites and the weak connection in between substrate and active material. As the electrode was screen printed so the connection between active material and substrate is weaker than those films on which material is directly grown.

Table 1. Supercapacitive performance of carbon aerogel derived from different drying methods.

Electrode material	Drying method	Activation	Electrolyte	Substrate	Potential window (V)	Specific capacitance (F/g)	Ref.
CA	Supercritical CO ₂ drying	CO ₂	1M H ₂ SO ₄	-	0-0.8	95 (5mV/s)	[9]
CA	Ambient drying	KOH	6M KOH	SSM	-1	119 (10mV/s)	[27]
CA	Supercritical CO ₂ drying	-	2M H ₂ SO ₄	Pt mesh	-	100 (2 A/g)	[28]
CA	Freeze drying	-	EMIM BF ₄	-	0-3.6	173 (3 A/g)	[29]
Benzoxazine based CA	Supercritical CO ₂ drying	-	6M KOH	-	-1	199 (0.5 A/g)	[30]
CA	Ambient drying	-	1M H ₂ SO ₄	SSM	0-0.7	81 (10mV/s)	[31]
CA	Supercritical CO ₂ drying	-	1M NaCl	-	-1	130 (1mV/s)	[32]
CA	Supercritical in ethanol	-	1M Na ₂ SO ₄	SSM	-1.9	113 (5mV/s)	This work

Table-1 summarized the supercapacitive performances of carbon aerogels derived from different drying methods reported by various research groups [9,10,27–32]. Herein the electrodes prepared by the pristine carbon aerogel obtained by supercritical drying using ethanol. These electrodes tested in neutral electrolyte-1M Na₂SO₄ showed 1.9 V potential window with specific capacitance 113 F/g (5 mV/s).

4. CONCLUSION

In conclusion, a pearl-like, interconnected, and porous structure of carbon with porosity was observed in the prepared aerogel. This aerogel has a lot of surface functional groups, which improves surface wettability and raises capacitance. The prepared carbon aerogel was used as an electrode for EDLC and showed highest

capacitance 113 F/g in 1M Na₂SO₄ electrolyte. The choice of neutral electrolyte helped to increase the working potential window. The good retentivity in capacitance was observed due to the 3D and uniform interconnected network of carbon structure which facilitate the flow of electron and the porous network bestow the plentiful active sites for ion interaction. Such low cost, flexible carbon electrodes were proved themselves as a good candidate for supercapacitors with wide potential window used in various applications like the energy storage devices.

ACKNOWLEDGMENT

Author AVP thankfully acknowledge the financial support provided by and Chhatrapati Shahu Maharaj Research Training and Human Development Institute (SARTHI), Pune. The financial assistance through DST PURSE-Phase II (2018-2022) & UGC DSA- Phase II (2018-2023) is highly acknowledged by authors.

REFERENCES

1. Shin, J., Seo J. K., Yaylian, R., Huang, A., Meng, Y. S. (2020) *International Materials Reviews*, 65, 356-387.
2. Li, J., Wang, X., Huang, Q., Gamboa, S., Sebastian, P. J. (2006) *Journal of Power Sources*, 160, 1501-1505.
3. Kandalkar, S. G., Dhawale, D. S., Kim, C. K., Lokhande, C. D. (2010) *Synthetic Metals*, 160, 1299-1302.
4. Myung, Y., Jung, S., Tung, T. T., Tripathi, K. M. (2019) *ACS Sustainable Chemistry & Engineering*, 7, 3772-3782.
5. Pandolfo, A. G., Hollenkamp, A. F. (2006) *Journal of Power Sources*, 157, 11-27.
6. Marichi, R. B., Goel, S., Tomar, A. K., Sahu, V., Lalwani, S., Singh, G., Sharma, R. K. (2020) *Materials Chemistry and Physics*, 239, 121957.
7. Fischer, U., Saliger, R., Bock, V. (1997) *Journal of Porous Materials*, 4, 281-285
8. Jae, Y., Chul, J., Yi J., Baeck, S., Rag, J., Kyu I. (2010) *Current Applied Physics*, 10682-686.
9. Pekala, R. W., Farmer, J. C., Alviso, C. T., Tran, T. D., Mayer, S. T., Miller, J. M., Dunn, B. (1998) *Journal of Non-Crystalline Solids*, 225, 74-80.
10. Hwang, S., Hyun, S. (2004) *Journal of Non-Crystalline Solids*, 347, 238-245.
11. Kim, S. J., Hwang, W., Hyun, S. H. (2005) *Journal of Materials Science*, 40, 725-731.
12. Shen, J., Guan, D. Y., *Aerogels Handbook, Advances in Sol-Gel Derived Materials and Technologies*, edited by Aegerter, M. A. (2011) pp. 813-831.
- 13.

14. Jae, Y., Chul, J., Park, S., Gil, J., Baeck, S., Rag, J., Yi J., Kyu, I. (2011), *Current Applied Physics*, 11, 1-5.
15. Lei, E., Li, W., Ma, C., Xu, Z., Liu, S. (2018) *Applied Surface Sciences*, 457, 477-486.
16. Mirzaeian, M., Abbas, Q., Gibson, D., Mazur, M. (2019) *Energy*, 173, 809-819.
17. Li, J., Wang, X., Huang, Q., Gamboa, S., Sebastian, P. J. (2006) *Journal of Power Sources*, 158, 784-788.
18. Hebalkar, N., Arabale, G., Sainkar, S. R., Pradhan, S. D., Mulla, I. S., Vijayamohan, K., Ayyub, P., Kulkarni, S. K. (2005) *Journal of Materials Science*, 40, 3777-3782.
19. Prakash, A., Bhatnagar, A., Shukla, V., Sekkar, V., (2020) *International Journal of Hydrogen Energy*, 45, 30818-30827.
20. Wang, L., Mu, G., Tian, C., Sun, L., Zhou, W., Yu, P., Yin, J. (2013) *Chemistry Sustainability Energy Materials*, 1-11.
21. Cheng, P., Li, T., Yu, H., Zhi, L., Liu, Z., Lei, Z. (2016) *Journal of Physical Chemistry C*, 120, 2079-2086.
22. Cai, T., Wang, H., Jin, C., Sun, Q., Nie, Y. (2018) *Journal of Materials Science: Materials in Electronics*, 29, 4334-4344.
23. Wang, H., Xu, Z., Kohandehghan, A., Li, Z., Cui, K., Tan, X., Stephenson, T. J., King, C. K., Holt, B., Olsen, B. C., Tak, J. K., Harfield, D., Anyia, A. O., Mitlin, D. (2013) *ACS Nano*, 5, 5131-5141.
24. Zhong, C., Deng, Y., Hu, W., Qiao, J., Zhang, L., Zhang, J. (2015) *Chemical Society Reviews*, 44, 7484-7539.
25. Zheng, J. P., Jow, T. K. (1997) *Journal of the Electrochemical Society*, 144, 9-12.
26. Tsay, K. C., Zhang, L., Zhang, J. (2012) *Electrochimica Acta*, 60, 428-436.
27. Mei, B. A., Munteshari, O., Lau, J., Dunn, B., Pilon, L. (2018) *Journal of Physical Chemistry C*, 122, 194-206.
28. Lee, Y. J., Park, H. W., Park, S., Song, I. K. (2012) *Current Applied Physics*, 12, 233-237.
29. Malkova, A. N., Sipyagina, N. A., Gozhikova, I. O., Dobrovolsky Y. A., Konev, D. V., Baranchikov, A. E., Ivanova, O. S., Ukshe A. E., Lermontov, S. A. (2019) *Molecules*, 24, 1-13.
30. Li, F., Xie, L., Sun, G., Su, F., Kong, Q., Li, Q., Chao, Y., Guo, X., Chen, C. (2017) *ChemElectroChem*, 4, 3119-3125.
31. Zhang, M., Chen, M., Reddeppa, N., Xu, D., Jing, Q. (2015) *Nanoscale*, 3, 10715-10722.
32. Lee, Y. J., Jung, J. C., Park S., Seo J. G., Baeck, S. (2011) *Current Applied Physics*, 28, 492-496.
33. Salihovic, E., Nicola, H. (2018) , *RSC Advances*, 8, 27326-27331.

Investigation of Effect of Critical Power of Beam on Propagation of Super Gaussian Beam in Collisional Plasma

Prasad T. Takale^a, Vinayak S. Pawar^b, Kalyani Y. Khandale^a, Sanyogita S. Patil^c, Sandip D. Patil^c, Mansing V. Takale^{a,*}

^aDepartment of Physics, Shivaji University, Kolhapur 416 004 (MS) India.

^bDepartment of Physics, DKASC College, Ichalkarangi 416 115 (MS) India.

^cDepartment of Physics, Devchand College, Kolhapur 591 237 (MS) India.

*Corresponding author: mvtpthyunishivaji@gmail.com

ABSTRACT

In present paper, effect of critical power on propagation of super Gaussian laser beam in collisional plasma is studied theoretically. In present study, the nonlinearity considered herein due to non-uniform heating of carriers along the wavefront of the laser beam. Nonlinear differential equation is obtained using extra paraxial method. The dielectric constant (ϵ) of collisional plasma and eikonal are expanded upto r^4 . The regions of critical power are obtained and propagation of super Gaussian beam is studied within these regions. Results are found interesting and shown graphically and discussed.

KEYWORDS

Super gaussian beam, Collisional plasma, Self-focusing, Critical power.

.....

1. INTRODUCTION

In last four decades, the physical phenomenon of laser-matter interaction is studied extensively. The high intense laser through the plasma has wide range of applications like plasma-based accelerator [1,2], optical harmonic generation [3,4], X-ray lasers [5], new radiation sources [6] and inertial confinement fusion with fast igniter scheme [7]. Mostly used model for self-focusing of laser beam in the plasma is basically based upon the standard WKB and Paraxial Ray Approximation (PRA) through a nonlinear parabolic wave equation [8-10]. Various investigations have been done on the nonlinear propagation of Super-Gaussian laser beam in the plasmas [11-15]. Sartang [16] highlighted ring like structure in self focused beam. Ring formation and collapse dynamics of super Gaussian beam have been studied by Grow [12]. Mishra [17] and Faisal [18] have identified region where ring formation occurs and paraxial theory is valid. Prime interest of paper is to study effect of critical power on propagation of beam in collisional plasma. So to study effect, region of critical power is calculated. Propagation of beam is studied using extra paraxial approach. Present paper is

organized as follows: In section 2 nonlinear differential equation of beam width parameter is obtained. Discussion of result is done in section 3. Finally brief conclusion is in section 4.

2. FORMULATION

Consider Super-Gaussian beam propagating through collisional plasma along \hat{z} direction. The electric field of beam is given as

$$E(r, z) = A(r, z) \text{Exp}[i(kz - \omega t)] \quad (1)$$

where $A(r, z)$ is complex amplitude of electric field, $k = \frac{\omega}{c} \sqrt{\epsilon_0}$ is propagation constant and ω is frequency of beam. A field distribution of Super Gaussian beam propagating along \hat{z} direction in plasma may be given as

$$A^2 = \frac{E_0^2}{f^2} \left(1 + \frac{a_2 r^2}{r_0^2 f^2} + \frac{a_4 r^4}{r_0^4 f^4} \right) * \exp \left[- \left(\frac{r}{r_0 f} \right)^{2m} \right] \quad (2)$$

where m is Super Gaussian coefficient, f is beam width parameter, parameters, a_2, a_4 symbolises deviation of beam profile from super Gaussian nature. And the eikonal is given as

$$S = S_0 + S_2 \frac{r^2}{r_0^2} + S_4 \frac{r^4}{r_0^4}$$

where S_2 symbolises spherical curvature of beam and S_4 symbolises deviation from spherical nature. Using the field distribution given in equation 2 and following analysis of Faisal [18], one can obtain following equations for Super-Gaussian coefficient $m = 2$ as

$$S_2 = \frac{r_0^2}{2f} \frac{df}{dz} \quad (3)$$

$$a_4 = \frac{a_2^2}{4} \quad (4)$$

$$\frac{d^2 f}{d\xi^2} = \frac{a_2^2 - 8}{\epsilon_0 f^3} - \frac{\epsilon_2 f \rho^2}{\epsilon_0} - \frac{1}{2\epsilon_0} \frac{d\epsilon_0}{d\xi} \frac{df}{d\xi} \quad (5)$$

$$\frac{d^2 S_4}{d\xi^2} = -\frac{1}{2\epsilon_0 f^6} \left(2a_2 + \frac{5}{4} a_2^3 \right) - 4 \frac{S_4'}{f} \frac{df}{d\xi} - \frac{S_4'}{2\epsilon_0} \frac{d\epsilon_0}{d\xi} - \frac{\epsilon_4 \rho^2}{2\epsilon_0} \quad (6)$$

where $\rho = \frac{r_0 \omega p}{c}$, $\xi = \frac{z}{kr_0^2}$.

Similar equations observed for Super Gaussian beam in Gill [15].

The effective dielectric constant of collisional plasma is given as

$$\epsilon = 1 - \frac{\omega_p^2}{\omega^2} + \frac{\omega_p^2}{\omega^2} \left(\frac{\alpha A^2}{2 + \alpha A^2} \right) \quad (7)$$

where $\omega_p = \sqrt{\frac{4\pi n_0 e^2}{m}}$ is plasma frequency, $\alpha = \frac{e^2}{m^2 \omega^2 c^2}$. Here e is the charge on electron and λ is wavelength of laser used. Substituting value of A^2 from equation (2) in equation (7) and expanding ϵ as series in $\frac{r}{r_0}$ upto $\frac{r^4}{r_0^4}$, one can get

$$\epsilon = \epsilon_0 - \frac{r^2}{r_0^2} \epsilon_2 - \frac{r^4}{r_0^4} \epsilon_4 \quad (8)$$

Where

$$\epsilon_0 = 1 - \frac{\omega_p^2}{\omega^2} + \frac{P * \left(\frac{\omega_p^2}{\omega^2} \right)}{(2 + P)} \quad (9)$$

$$\epsilon_2 = - \frac{2a_2 P \left(\frac{\omega_p^2}{\omega^2} \right)}{f^2 (P + 2)^2} \quad (10)$$

$$\epsilon_4 = \frac{\left(\frac{\omega_p^2}{\omega^2} \right) (4P^2 + 3a_2^2 P^2 + 8P - 2a_2^2 P)}{2f^2 (P + 2)^3} \quad (11)$$

$$\text{where } = \frac{\alpha A_0^2}{f^2}.$$

3. RESULT AND DISCUSSION

Equation (5) is nonlinear second order ordinary differential equation governing the variation of dimensionless beam width parameter along dimensionless distance ζ . Numerical solution of equation (5) can be obtained using initial conditions $f = 1, \frac{df}{d\zeta} = 0, S_4 = 0$ and $a_2 = 0$. Under critical conditions, power of beam P is replaced by critical power $P_0 = \alpha A_0^2$. So RHS of equation 5 becomes function of P_0 as follows

$$F(P_0) = \frac{a_2^2 - 8}{\epsilon_0} - \frac{\epsilon_2 \rho^2}{\epsilon_0} \quad (12)$$

Necessary numerical parameters are $r_0 = 20 \times 10^{-4} \text{cm}$, $\omega = 1.78 \times 10^{14} \text{rad/sec}$, $n_0 = 5 \times 10^{18} \text{cm}^{-3}$, $\rho = 11.84$, $a_2 = 1.2$.

Region I	Region II	Region III
$0 < P_0 < 0.19$	$0.19 < P_0 < 20.94$	$P_0 > 20.94$

To study effect of power on propagation of super Gaussian beam, one has to consider **Figure-1**. In **Figure-1**, three regions of power are observed.

Table-1. Regions of Critical Power.

Figure-2 shows variation of beam width parameter along normalised distance of propagation. Self-focusing of beam is observed in region I and III while steady defocusing of beam observed in region II. Trapping of beam is observed at $P_0 = 0.19$ and $P_0 = 20.94$. Hence **Figure-2** supports investigated limits of critical power of beam.

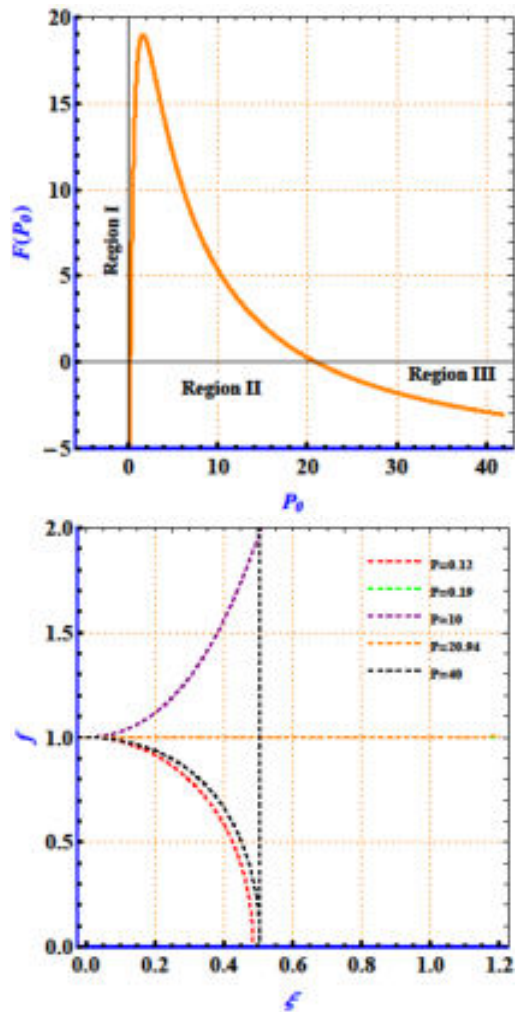


Figure-1. Variation of $F(P_0)$ along P_0 .

Figure-2. Variation of f vs ξ for different critical powers ($P_0 = 0.12, 0.19, 10, 20.94, 40$).

4. CONCLUSION

In present study, propagation of super Gaussian in collisional plasma is studied. Nonlinear differential equation is set up using extra paraxial approach. Effective dielectric constant is extended up to $\frac{r^4}{r_0^4}$. Effect of critical power of beam is studied. Regions of critical power of beam is calculated. Critical power of beam can influence propagation of beam in a collisional plasma.

ACKNOWLEDGMENT

Authors are thankful to DST-PURSE Phase-II (2018- 2023) and UGC DSA - Phase II (2018-2023) Programme for providing research facilities at the Department of Physics, Shivaji University, Kolhapur, M.S., India

REFERENCES

1. Sarkisov, G. S., Bychenkov, V. Y., Novikov, V. N., Tikhonchuk, V. T., Maksimchuk, A., Chen, S. Y., Wagner, R., Mourou, G., Umstadter, D. (1999) *Physical Review E*, 59, 7042.
2. Esarey, E., Sprangle, P., Krall, J., Ting, A. (1996) *IEEE Transactions on Plasma Science*, 24, 252–288.
3. Liu, X., Coe, J. S., Chien, C. Y., Umstadter, D., Esarey, E., Sprangle, P. (1991) In *OSA Proceedings on Short-Wavelength Cherenkov Radiation: Generation and Application*, 7-11.
4. Sprangle, P., Esarey, E., Ting, A. (1990) *Physics Review Letter*, 64, 2011–2014.
5. Burnett, N. H., Corkum, P. B. (1989) *Optical Society of America B*, 6, 1195– 1199.
6. Benware, B. R., Macchietto, C. D, Moreno, C. H., Rocca, J. J. (1998) *Physics Review Letter*, 81, 5804–5807.
7. Tabak, M., Hammer, J., Glinsky, M. E., Kruer, W. L., Wilks, S. C., Woodworth, J., Campbell, E. M., Perry, M. D., Mason, R. J. (1994) *Physics of Plasma*, 1, 1626–1634.
8. Akhmanov, S. A., Sukhorukov, A. P., Khokhlov, R. V. (1966) *Journal of Experimental and Theoretical Physics*, 23, 1025.
9. Akhmanov, S. A., Sukhorukov, A. P., Khokhlov, R. V. (1968) *Soviet Physics Uspekhi*, 10, 609–636.

10. Sodha, M. S., Ghatak, A. K, Tripathi, V. K. In Self-focusing of laser beams in dielectrics, plasmas and semiconductors, Tata McGraw- Hill (1974), 9-17
11. Nayyar, V. P. (1986) Journal of Optical Society of America B, 3, 711–714.
12. Grow, T. D., Ishaaya, A. A., Vuong, L. T., Gaeta, A. L., Gavish, N., Fibich G. (2006) Optics Express, 14, 5468– 5475.
13. Karlsson, M., Anderson, D. (1992) Journal of Optical Society of America B, 9, 1558–1562.
14. Gill, T.S., Mahajan, R., Kaur, R., Gupta, S. (2012) Laser and Particle Beams, 30, 509– 516.
15. Devi, L., Malik, H. K., (2020) Optik, 207, 164439.
16. Sartang, S., Evans, R. G., Toner, W.T. (1983) Journal of Physics D, 16, 955.
17. Mishra S., Mishra S. K. (2009) Journal of Plasma Physics, 75, 769–785.
18. Faisal, M., Mishra, S. K., Varma, M. P., Sodha, M.S. (2007) Physics of Plasmas, 14, 103103.

Effect of Self-focusing and Diffraction Length on Propagation of Gaussian Laser Beam in Non-Degenerate Germanium having Space Charge Neutrality

Kalyani Y. Khandale^a, Trupti U. Urunkar^a, Prasad T. Takale^a,
Sanyogita S. Patil^b, Purva P. Nikam^b, Manisha B. Mane^b,
Sandip D. Patil^b, Mansing V. Takale^{a,*}

^aDepartment of Physics, Shivaji University, Kolhapur 416 004 (MS) India.

^bDepartment of Physics, Devchand College, Kolhapur 591 237 (MS) India.

*Corresponding author: mvtphyunishivaji@gmail.com

ABSTRACT

It is widely known that the self-focusing length R_n and diffraction length R_d play crucial role in propagation dynamics of Gaussian laser beam in non-degenerate germanium having space charge neutrality under ponderomotive nonlinearity. The key interest of present theoretical investigation is to study the effect of interval of $R = R_d/R_n$ to sustain the competition between the phenomena of diffraction and self-focusing during beam propagation. The differential equation governing the dimensionless beam width parameter (BWP) f is achieved by using Wentzel–Kramers–Brillouin (WKB) and paraxial approximations and solved it numerically by utilizing Runge-Kutta fourth order method. To explain it further the plot between function $F(R)$ against R is studied. The behavior of the BWP f with the dimensionless propagation distance ξ under various intervals of R is examined by numerical estimates. It is found that the self-focusing length and rate of defocusing changes with R . The results are presented graphically and discussed.

KEYWORDS

Gaussian, Self-focusing/defocusing, Self-trapping, Germanium.

.....

1. INTRODUCTION

Many novel phenomena were seen and a great deal of interest was generated by the study of how high intensity laser beams interacted with different types of material media. One of the crucial and most fascinating aspects of non-linear optics is self-focusing. Numerous non-linear optical phenomena, such as stimulated Raman and Brillouin scattering, optical breakdown of gases, two-photon absorption, etc., are significantly impacted by self-focusing [1-3]. An intense laser beam can shrink when propagating in a material medium through the influence of self-focusing was first

proposed by Askar'yan in 1962 [4]. Piliptskii and Rustamov registered the first experimental observation of self-focusing by taking pictures of small luminous filaments stimulated in organic liquids by a focused Ruby laser beam [5]. The work in the area of self-focusing resulted in a numerous of controversies and many review articles about self-focusing were published [6-11]. Among these analyses on self-focusing, Akhmanov et. al. [6] have been introduced the self-focusing of laser beams for nonlinear media and its pedagogical straight forward development to plasmas by Sodha et. al. [9]. The self-focusing phenomenon is third order nonlinear effect. When the laser beam incidents on plasma, it modifies the dielectric constant results in modification of the refractive index of plasma and hence laser beam self-focuses/defocuses. There are three prime mechanisms of self-focusing in plasmas: (i) relativistic, (ii) collisional, and (iii) ponderomotive force. Self-focusing of laser beams has wide range of applications such as inertial confinement fusion ICF, laser wakefield acceleration, higher harmonic generation, generation of THz radiation, laser-driven plasma acceleration, X-ray lasers etc., [12-17]. Some following different kinds of laser beam profiles have been explored for the studies of propagation dynamics like Gaussian beams [18-23], Cosh-Gaussian beams [24-27], Hermite Gaussian beams [28], Hermite-cosh-Gaussian (HChG) beams [29-32], Quadrupole Gaussian beams [33], elliptic Gaussian beams [34], Super Gaussian beams [35], and q-Gaussian beams [36, 37], etc., in the plasmas has attracted the attention of the many researchers since last two decades.

The present study explores the propagation dynamics of Gaussian laser beam in non-degenerate germanium having space charge neutrality. In present medium the nonlinearity is induced because of the non-uniform heating and consequent redistribution of carriers in the presence of an electromagnetic beam. The current theoretical investigation is carried out under parabolic wave equation approach via WKB and Paraxial approximations [6, 9].

2. THEORETICAL FRAMEWORK

Consider a field distribution of Gaussian laser beam of the following form propagating along z axis

$$E = A(r, z) \exp[i(\omega t - k_0 z)] \dots\dots\dots (1)$$

where, $k_0 = (\omega/c) \sqrt{\epsilon_0}$, k_0 is the wave number, c is speed of light, and ω is frequency of laser beam used. The effective dielectric constant of the medium through which laser beam propagates can, in general, be written as [9].

$$\epsilon = \epsilon_0 + \Phi(EE^*) \dots\dots\dots (2)$$

where, $\epsilon_0 = 1 - (\omega_p^2/\omega^2)$ and $\Phi(EE^*)$ are the linear and nonlinear terms of the dielectric constant ω_p is plasma frequency $\omega_p = \sqrt{4\pi n_e e^2/m_0}$, where m_0 , e , and

n_e are rest mass of electron, the electronic charge, and plasma electron's density without laser beam, respectively.

For the non-degenerate germanium, the nonlinear term of the dielectric constant is given by [29].

$$\Phi(EE^*) = \frac{\omega_p^2}{\omega^2} \alpha_e \left(1 + \frac{m_e}{m_h}\right) A_0^2 \dots\dots\dots (3)$$

with $\alpha_e = (e^2 M / 6 k_B T_0 \omega^2 m^2)$, where, k_B , M , m , T_0 are Boltzmann constant, mass of ion, electron mass, temperature of the plasma, respectively.

The propagation of laser beam in plasmas with effective dielectric constant ϵ can be governed by wave equation.

$$\nabla^2 E + \frac{\omega^2}{c^2} \epsilon E + \nabla \left(\frac{E \cdot \nabla \epsilon}{\epsilon} \right) = 0 \dots\dots\dots (4)$$

The last term in the equation (4) can be neglected provided that $\frac{c^2}{\omega^2} \left| \frac{1}{\epsilon} \nabla^2 (\ln \epsilon) \right| \ll 1$. This inequality is satisfied in almost all cases of practical interest. Thus, the equation (4) becomes,

$$\nabla^2 E + \frac{\omega^2}{c^2} \epsilon E = 0 \dots\dots\dots (5)$$

Within the framework of WKB approximation, the equation (5) reduces to a parabolic wave equation as follows

$$\frac{\partial^2 A}{\partial r^2} + \frac{1}{r} \frac{\partial A}{\partial r} + \frac{\omega^2}{c^2} \phi(EE^*) A = 2ik_0 \frac{\partial A}{\partial z} \dots\dots\dots (6)$$

Where,

$$A(r, z) = A_0(r, z) \exp [-ikS(r, z)] \dots\dots\dots (7)$$

where, S is the eikonal of the wave and $A_0(r, z)$ and $S(r, z)$ are the real functions of r and z . From equations (6) and (7) by separating real and imaginary parts, one can obtain

$$2 \left(\frac{\partial S}{\partial z} \right) + \left(\frac{\partial S}{\partial r} \right)^2 = \frac{1}{k^2 A_0} \left(\frac{\partial^2 A_0}{\partial r^2} + \frac{1}{r} \frac{\partial A_0}{\partial r} \right) + \frac{\phi}{\epsilon_0} (A_0 A_0^*) \dots\dots\dots (8)$$

and

$$\frac{\partial A_0^2}{\partial z} + \left(\frac{\partial S}{\partial r} \right) \left(\frac{\partial A_0^2}{\partial r} \right) + \left(\frac{\partial^2 S}{\partial r^2} + \frac{1}{r} \frac{\partial S}{\partial r} \right) A_0^2 = 0 \dots\dots\dots (9)$$

By following Akhmanov *et al.* [6] and Sodha *et al.* [9], the solutions of equations (8) and (9) are given by

$$S = \frac{r^2}{2} \beta(z) + \phi(z) \dots\dots\dots (10)$$

and

$$A_0^2 = \frac{E_0^2}{f^2} \exp\left(\frac{-r^2}{r_0^2 f^2}\right) \dots\dots\dots (11)$$

where, $\phi(z)$ is the phase shift, $\beta(z)$ can be written as $\left(\frac{1}{f}\right)\left(\frac{\partial f}{\partial z}\right)$ and it is the inverse of radius of curvature, r_0 is the initial radius of the laser beam, f is beam width parameter and it measures width of the beam as well as axial intensity. Following approach specified by Akhmanov *et al.* [6] and subsequently developed by Sodha *et al.* [9], we have obtained second order differential equation for beam width parameter f as

$$\frac{d^2 f}{d\xi^2} = \frac{4}{f^3} - \frac{4 R_d^2}{f^3 R_n^2} \dots\dots\dots (12)$$

where, $\xi = \frac{z}{R_d}$, $R_d = kr_0^2$, $R_n = (2\varepsilon_0 r_0^2 / \varepsilon_2 E^2)^{1/2}$, R_d , R_n and ξ are diffraction, self-focusing lengths and dimensionless distance of propagation respectively. The below necessary numerical parameters are used in the present theoretical investigation:

$m_e \approx 1 \times 10^{-28}$ g, $m_h \approx 3 \times 10^{-28}$ g, $N_{oe} \approx 1.5 \times 10^{15}$ cm⁻³, $N_{oh} \approx 1.4 \times 10^{16}$ cm⁻³, $\omega = 2 \times 10^{14}$ rad/s, $r_0 = 500 \mu\text{m}$, $\varepsilon_2 = 1.2 \times 10^{-7}$ esu, $E_0 = 15$ esu, $T_0 = 77$ K.

3. RESULTS AND DISCUSSION

Equation (12) is second order nonlinear differential equation which gives evolution of a laser beam during propagation to non-degenerate germanium. The first term on right-hand side of the equation (12) gives to the diffraction divergence of the beam which is responsible for defocusing while second term gives the convergence which is responsible for self-focusing resulting from the ponderomotive nonlinearity. Under initial condition ($f = 1$, $\frac{df}{d\xi} = 0$ and $\frac{d^2 f}{d\xi^2} = 0$ at $\xi = 0$) the right-hand side of equation (12) becomes,

$$F(R) = 4(1 - R^2) \quad (13)$$

Where, $R = R_d/R_n$.

To explore the effect of R right at the beginning one must pay little attention to plot shown in **Figure-1**. The plot can be conveniently studied for three distinct regions as mentioned below.

Self-trapping region:

$$F(R) = 0 \text{ for } R = 1 \text{ i.e., } R_d = R_n$$

Self-focusing region:

$$F(R) < 0 \text{ for } R > 1 \text{ i.e., } R_d > R_n$$

Defocusing region:

$$F(R) > 0 \text{ for } R < 1 \text{ i.e., } R_d < R_n$$

The simple analytical approach leads to following limits for R is depicted in **Figure-1**.

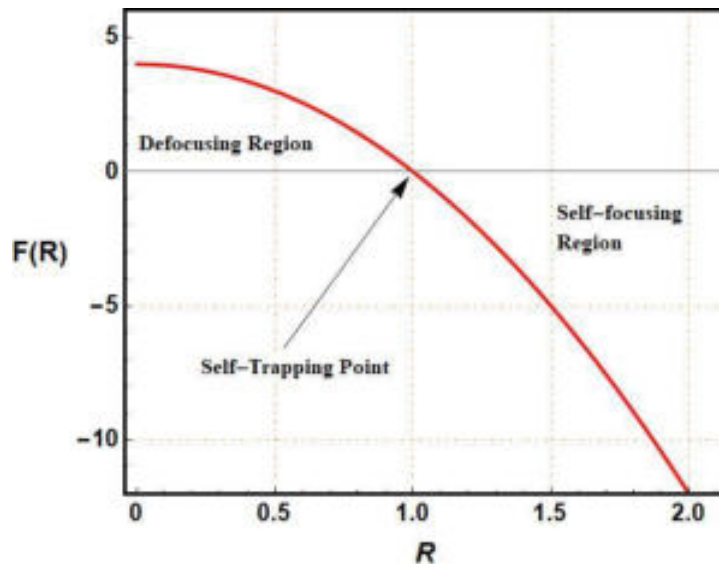


Figure-1. Variation of $F(R)$ as a function of R .

The limits of R investigated in above conditions can support the graph of beam width parameter f versus normalized propagation distance ξ as shown in **Figure-2**. From **Figure-2** the steady state defocusing of the beam is observed for $R < 1$ the beam undergoes defocusing.

Again, as R increases from 0 to 1 rate of defocusing is decreases. The beam propagates without convergence or divergence (self-trapped mode) at exact value $R = 1$. It is also evident from **Figure-2** that the self-focusing is observed for $R > 1$ and as R increases from 1 the self-focusing length decreases. Such type of self-focusing character of Hermite-cosh-Gaussian laser beams for various mode indices in non-degenerate germanium having space charge neutrality has been previously reported in earlier studies [29].

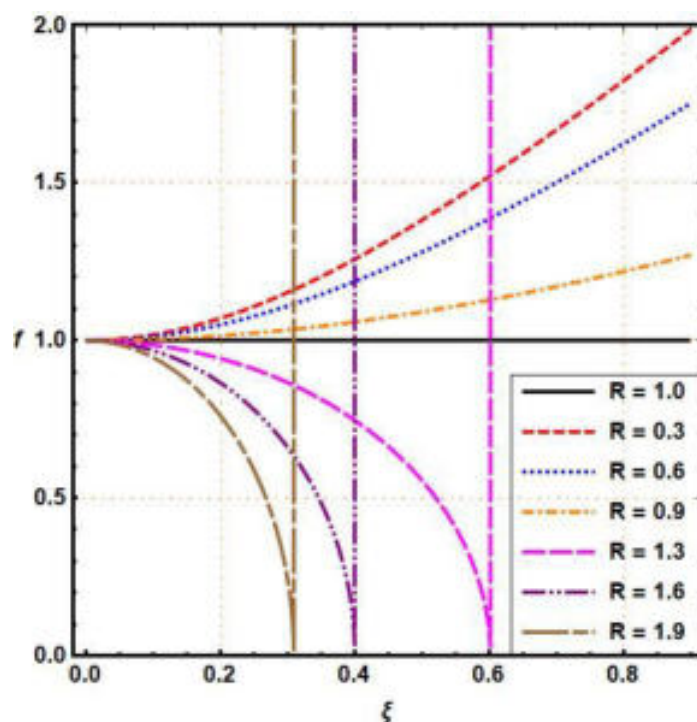


Figure-2. Dependence of beam-width parameter f with respect to normalized propagation distance ξ .

4. CONCLUSION

In the present theoretical investigation, the authors have explored analytically the propagation dynamics of Gaussian laser beam propagating in the non-degenerate germanium having space charge neutrality. The nonlinear differential equation for beam width parameter f is obtained under paraxial and WKB approximations via parabolic equation approach. It is observed that our investigation shows that pre-conditioning of self-focusing and diffraction length at the beginning of propagation can determine propagation dynamics effectively and self-trapping condition is obtained.

ACKNOWLEDGMENT

The authors are thankful to UGC - DSA Phase - II (2018-2023) and DST - PURSE Phase - II (2018-2023) for providing computer research facilities in Department of Physics, Shivaji University, Kolhapur, Maharashtra, India.

REFERENCES

1. Shen, Y. R., Shaham, Y. J. (1967) *Physical Review*, 163, 224-231.
2. Alcock, A. J., DeMichelis, C., V. V. Korobkin, V. V., Richardson. M. C. (1969) *Applied Physics Letters*, 14, 145-146.
3. Chiao, Y. R., Deutsch, I. H. (1991) *Physical Review Letters*, 67, 1399-1402.
4. Askaryan, G. A. (1962) *Journal of Experimental and Theoretical Physics*, 15, 1088.
5. Pilipetskii, N. F., Rustamov, A. F. (1965) *JETP Letters*, 2, 55.
6. Akhmanov, S. A, Sukhorukov, A. P., Khokhlov, R. V. (1968) *Soviet Physics Uspekhi*, 10, 609.
7. Svelto, O. (1974) *In Progress in Optics*, 12, 1-51.
8. Lugovoi, V. N., Prokhorov, A. M. (1975) *Progress Lasers and Laser Fusion*, 77, p. 309-407.
9. Sodha, M. S., Ghatak, A. K., Tripathi, V. K. (1976) *In Progress in Optics*, 13, 169-265.
10. Shen, Y. R. (1975) *Progress in Quantum Electronics*, 4, 1-34.
11. Marburger, J. H. (1975) *Progress in Quantum Electronics*, 4, 35-110.
12. Tabak, M., Hammer, M. E. (1994) *Physics of Plasmas*, 1, 1626.
13. Liu, C. S., Tripathi, V. K. (2009) *Journal of Applied Physics*, 105, 013313.
14. Rajput, J., Kant, N., Singh, H., Nanda, V. (2009) *Optics Communications*, 282 4614-4617.
15. Jha, P., Saroch. A, Mishra, R. K., Upadhyaya A. K. (2012) *Physical Review Accelerators and Beams*, 15, 081301.
16. Hooker, S. M. (2013) *Nature Photonics*, 7, 775-782.
17. Suckewer, S., Skinner, C. H. (1990) *Science*, 247, 1553-1557.
18. Navare, S. T., Takale, M. V., Patil, S. D., Fulari, V. J., Dongare, M. B. (2012) *Optics and Lasers in Engineering*, 50, 1316–1320.
19. Singh, A., Walia, K. (2013) *Journal of Physics: Energy*, 32, 422-425.
20. Patil, S. D., Takale, M. V. (2013) *Physics of Plasmas*, 20, 072703.
21. Patil, S. D., Takale, M. V., Gill, T. S. (2015) *European Physical Journal D*, 69, 1-4.
22. Wani, M. A., Kant, N. (2016) *Communications in Theoretical Physics*, 66, 349–354.
23. Valkunde, A. T., Patil, S. D., Takale, M. V., Vhanmore, B. D., Urunkar, T. U., Gavade. K. M, Gupta, D. N. (2018) *Optik* 158, 1034–1039.
24. Patil, S. D., Takale, M. V. (2013) *Laser Physics Letters*, 10, 115402.

25. Aggarwal, M., Vij, S., Kant, N. (2014) *Optik*, 125, 2081-5084.
26. Vhanmore, B. D., Patil, S. D., Valkunde, A. T., Urunkar, T. U., Gavade, K. M., Takale, M. V. (2017) *Laser and Particle Beams*, 35, 670-676.
27. Urunkar, T. U., Patil, S. D., Valkunde, A. T., Vhanmore, B. D., Gavade, K. M., Takale, M. V. (2018) *Communications in Theoretical Physics*, 70, 220–224.
28. Takale, M. V., Navare, S. T., Patil, S. D., Fulari, V. J., Dongare, M. B. (2009) *Optics Communications*, 282, 3157–3162.
29. Patil, S., Takale, V., Fulari, V., Dongare, M. (2008) *Journal of Modern Optics*, 55, 3527–3533.
30. Kaur, S., Kaur, M., Kaur, R., Gill, T. S. (2017) *Laser and Particle Beams*, 35, 100-107.
31. Valkunde, A. T., Patil, S. D., Vhanmore, B. D., Urunkar, T. U., Gavade, K. M., Takale, M. V., Fulari, V. J. (2018) *Physics of Plasmas*, 25, 033103.
32. Vhanmore, B. D., Valkunde, A. T., Urunkar, T. U., Gavade, K. M., Patil, S. D., Takale, M. V. (2019) *European Physical Journal D*, 73, 1-4.
33. Kashyap, R., Aggarwal, M., Kumar, H., Mahajan, R., Arora, N. S., Gill, T. S. (2018) *Laser and Particle Beams*, 36, 353-358.
34. Gill, T. S., Saini, N. S., Kaul, S. S., Singh, A. (2004) *Optik*, 115, 493-498
35. Gill, T. S., Mahajan, R., Kaur, R., Gupta, S. (2012) *Laser and Particle Beams*, 30, 509-516
36. Vhanmore, B. D., Patil, S. D., Valkunde, A. T., Urunkar, T. U., Gavade, K. M., Takale, M. V., Gupta, D. N. (2017) *Optik*, 158, 574-579.
37. Valkunde, A. T., Vhanmore, B. D., Urunkar, T. U., Gavade, K. M., Patil, S. D., Takale, M. V. (2018) *AIP Conference Proceedings*, 1953, 140088.

A Facile Hydrothermal Synthesis of Nickel Phosphate Hydrate for Supercapacitors

Satyajeet S. Patil^a, Sumit D. Korade^a, Sarika B Dhavale^a,
Shweta M. Pawar^a, Pramod S. Patil^{a,*}

^aDepartment of Physics, Shivaji University, Kolhapur 416 004 (MS) India.

*Corresponding author: psp_phy@unishivaji.ac.in

ABSTRACT

A simple hydrothermal approach is used in this work to deposit nickel phosphate hydrate (NPH) microplates on the Ni foam. The compositional, morphological, and electrochemical studies of NPH electrode was thoroughly investigated. An XRD investigation of NPH material revealed a monoclinic crystal structure. The study of SEM reveals a microplate-like structure. The electrochemical investigations of the NPH electrode were performed in a 1 M KOH electrolyte across a potential range of -0.2 to 0.55 V vs SCE. At a current density of 10 mA/cm², the NPH electrode shows a specific capacitance of 104 F/g (21.66 mAh/g). NPH deposited on Ni-foam is a competent electrode for energy storage devices.

KEYWORDS

Nickel phosphate hydrate, Supercapacitors, Electrochemical study, Hydrothermal.

.....

1. INTRODUCTION

Electric vehicles (EVs) are becoming more popular owing to their environmental friendliness. To run, modern EVs need to supply high power density along with energy density. Because of its intriguing properties, a supercapacitor is an appealing option among energy storage technologies [1]. Such as fast charging/discharging, high power density, significant stable cyclic life, a simpler synthesis path than batteries, and so on. SCs are split into two categories according to how they store the charges: electric double-layered capacitors (EDLCs) (non-faradic) and pseudocapacitors (Faradic).

Despite having a low energy density (0.1 Wh/kg), EDLCs have a high-power density. As opposed to batteries, pseudocapacitors have modest energy and power density. Different metal-based materials, including oxides [2], nitrides [3], sulphates [4] and carbides [5] are explored in pseudocapacitors. They have good capacitive capability as well as efficient cycle life. Various metal phosphates (MPs) [6] have high electrical conductivity and customizable morphologies [7]. MPs offer a variety of shapes [8]. Transition MPs have a wide variety of valence states [9].

Owing to their excellent chemical stabilization and catalytic characteristics,

MPs are at the central core of many technological and economic concerns. MPs are used effectively in various fields [10-16]. Due to its open structure with extensive pathways and voids, phosphorus is the most intriguing contender and has reliably sustained good ion/charge conductivity and storage capacity [17]. Because of their various active sites, MPs with different micro/nanostructures have long been of interest [18]. Chemical stability is provided by the structure's strong P-O covalent bonds [19]. All transition MPs have some potential, but nickel phosphate stands out as a particularly viable electrode material for energy storage applications.

To date, nickel phosphate has been fabricated by a diverse set of chemical approaches [13, 20-27]. According to existing literature, the disorder, nonappearance of grain boundaries, and smaller ion diffusion lengths of the hydrous phase of materials make them more electrochemically active and stable than the crystalline phases [28, 29].

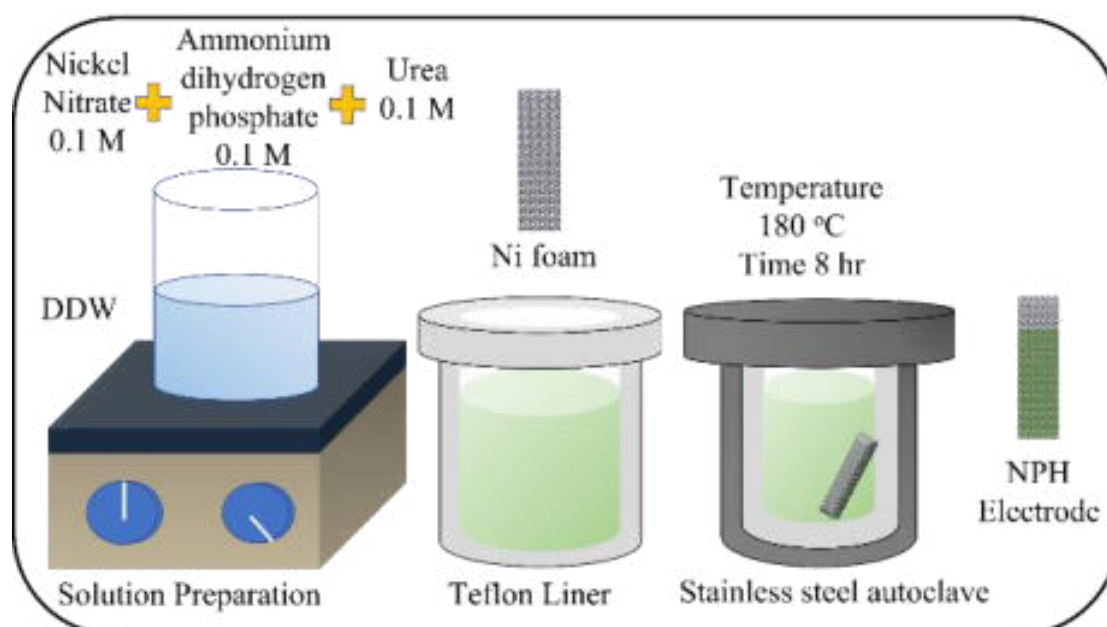


Figure-1. The hydrothermal synthesis of NPH electrode is shown schematically.

We used the simple hydrothermal approach on nickel foam to develop binder-free nickel phosphate hydrate (NPH) in this work. On the nickel foam, NPH microplates grow evenly. NPH microplates can be used as electrode material in energy storage devices based on electrochemical performance.

2. EXPERIMENTAL SECTION

2.1. Synthesis of NPH Electrode

The hydrothermal technique is utilized to synthesize NPH electrodes. The chemicals

(A. R.) were purchased from SRL (India) and were utilized as it is. The Ni foam was bought from Vritra Tech., India. Firstly, 0.1 M nickel nitrate ($\text{Ni}(\text{NO}_3)_2 \cdot 6\text{H}_2\text{O}$), 0.1 M ammonium dihydrogen phosphate ($\text{NH}_4\text{H}_2\text{PO}_4$) and 0.1 M urea ($\text{CH}_4\text{N}_2\text{O}$) were added to 80 ml DDW. The solution was then stirred for 15 minutes before being transferred into a Teflon liner with precleaned nickel foam. After that, for 8 hours, the hydrothermal was set to 180°C. After deposition, the electrode was then air-dried at room temperature after being washed with DDW. The prepared electrode was designated as NPH.

2.2. Synthesis Characterization Techniques

An XRD with $\text{Cu K}\alpha = 1.5405 \text{ \AA}$ was used to analyze the structural features of the electrodes (Bruker Private Ltd., Germany, Model: D6 phaser). The surface morphology micrographs were captured using SEM (JEOL 6360). The materials FTIR spectra were obtained using a JASCO 4700 spectrometer (JASCO, Lisses, France) using the KBr pellet method in the 4,000-400 cm^{-1} wavenumber regions. A potentiostat (PGSTAT302N Metrohm auto lab, Netherlands) was used to study the electrochemical features of the electrode in a 1 M KOH electrolyte using CV, GCD, and EIS. The working, counter, and reference electrodes were the NPH electrode, a platinum wire, and the Saturated Calomel Electrode (SCE). Electrochemical studies were performed on an active region (1 cm^2) having $\sim 5 \text{ mg/cm}^2$ mass deposited.

3. RESULTS AND DISCUSSION

The XRD method was used to analyze the phase and structural features of an NPH electrode. The vertical lines in **Figure-2** represent the typical JCPDS card peaks. The NPH sample exhibits monoclinic structure in the XRD pattern, with the most prominent peak seen at 13.33°, belonging to the (020) plane. In addition to the most prominent peak, 28 other peaks are seen at 11.32°, 18.35°, 19.72°, 20.72°, 22.18°, 23.38°, 24.84°, 27.02°, 28.19°, 30.51°, 32.82°, 33.46°, 33.70°, 34.57°, 35.19°, 36.01°, 37.66°, 39.44°, 40.08°, 41.17°, 41.92°, 42.58°, 45.93°, 46.86°, 47.79°, 48.57°, 49.02°, and 51° which corresponds to (110), (200), (-101), (011), (130), (101), (-211), (040), (031), (-301), (240), (-321), (-141), (330), (150), (141), (301), (-112), (-202), (-341), (-251), (-222), (-161), (411), (132), (-332), (-402) and (431) planes respectively. Here the XRD pattern is well match with JCPDS card number 00-033-0951 (nickel phosphate hydrate) and 00-004-0850 (Ni foam). In the XRD pattern, there is no additional peaks seen, confirming the purity of the sample. Crystallite sizes of the sample is calculated using the Scherrer expression as [30],

$$D = \frac{0.9\lambda}{\beta \cos\theta} \quad (1)$$

Here λ represents the wavelength of the X-ray, β denotes the full width at half maximum, θ refers to the Bragg angle and D symbolizes the size of the crystallite. For the NPH sample, the computed crystallite size was 53.23 nm using highest

intense peak.

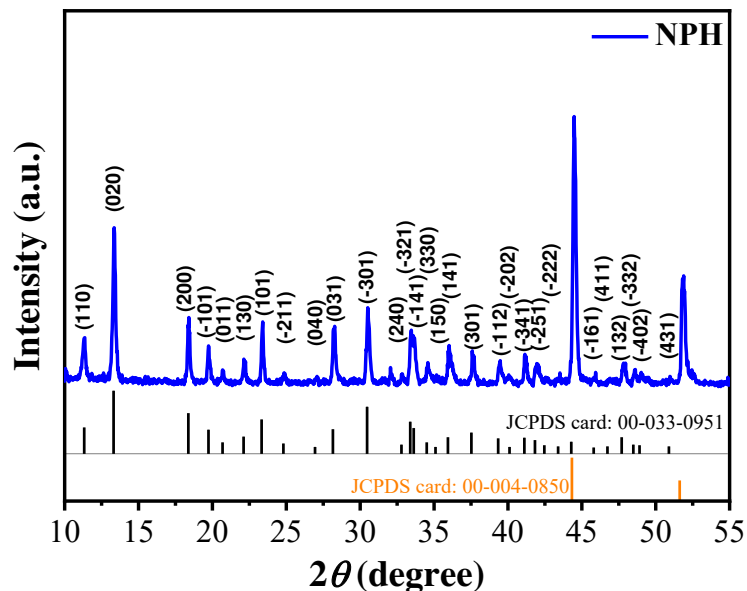


Figure-2. XRD pattern of the NPH sample.

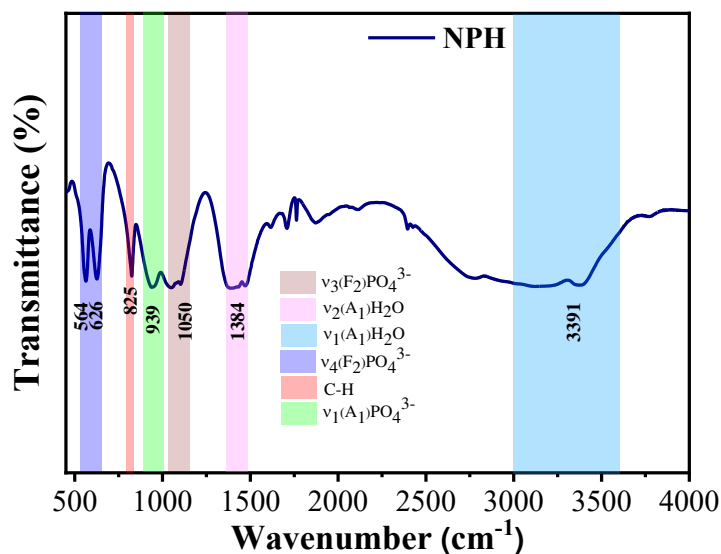
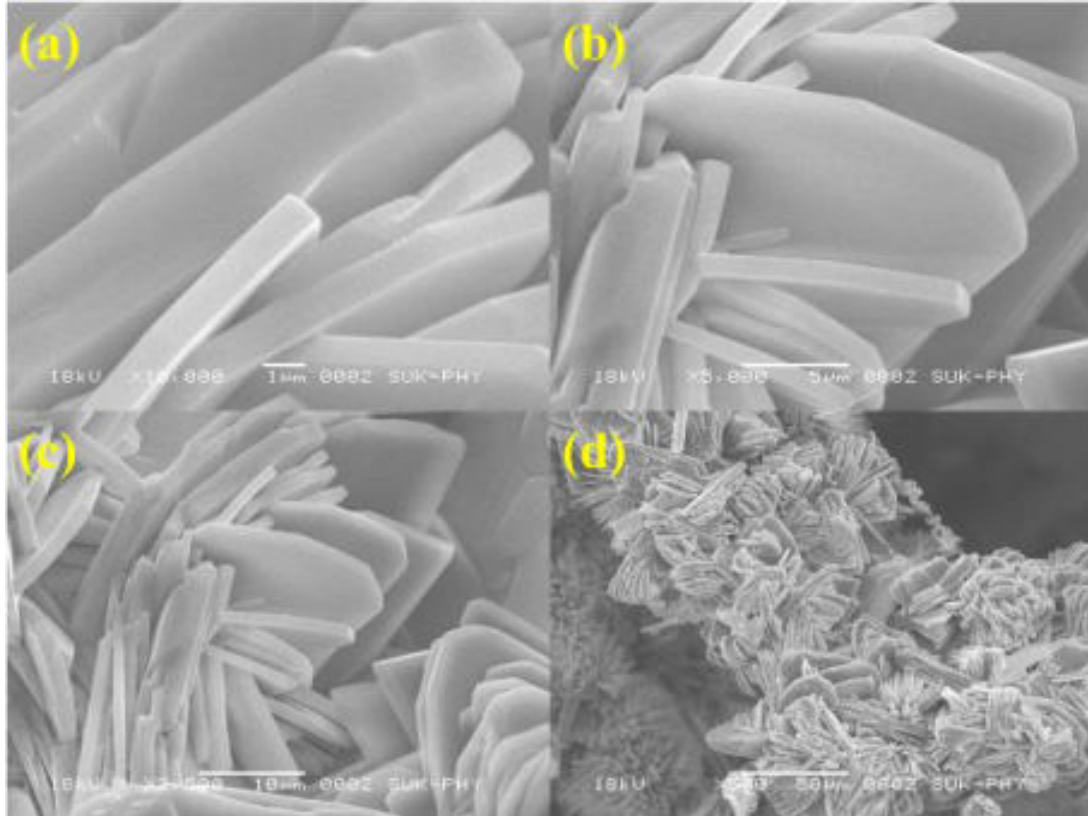


Figure-3. FT-IR of the NPH sample.

The existence of several functional groups in the NPH was studied using FT-IR analysis. The recorded FT-IR spectrum, is depicted in **Figure-3**. The vibrational bands for $(\text{PO}_4)^{3-}$ group appears in between $520\text{--}640\text{ cm}^{-1}$ ($v_4(\text{F}_2)\text{PO}_4^{3-}$), $850\text{--}960\text{ cm}^{-1}$ ($v_4(\text{F}_2)\text{PO}_4^{3-}$) and 1068 cm^{-1} ($v_3(\text{F}_2)\text{PO}_4^{3-}$) [24]. Furthermore water molecules bending bands occurs at 1384 cm^{-1} ($v_2(\text{A}_1)\text{H}_2\text{O}$) and $3000\text{--}3600\text{ cm}^{-1}$ ($v_1(\text{A}_1)\text{H}_2\text{O}$)

[31]. All of the FT-IR bands are consistent with the existing literature of NPH [32].

Figure-4. SEM images of the NPH sample.



SEM micrographs were acquired at 18 kV with magnifications of X 10,000, X 5,000, X 2,500, and X 500 to better understand the NPH electrode topologies, as shown in **Figure-4**. The NPH microplates are found to be evenly spread across the Ni foam. The microplates have an average thickness $\sim 1 \mu\text{m}$. Zhao et al. [33] and Liang et al. [34] found a similar plate-like shape of metal phosphate. The CV of the NPH electrode was investigated at several scan rates (shown in **Figure-5a**) in a working potential window ranging from -0.2 to 0.55 V vs SCE with strong redox peaks indicating that pseudo-capacitance is dominating.

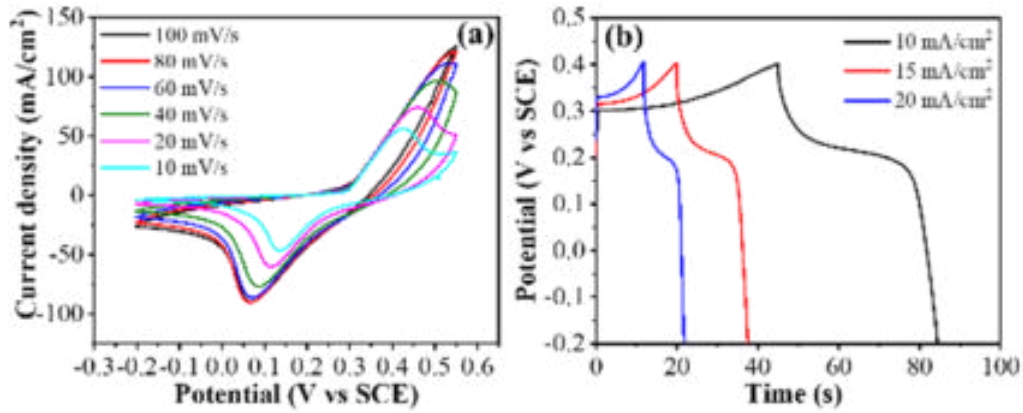
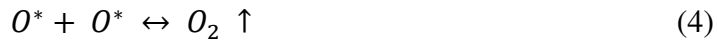
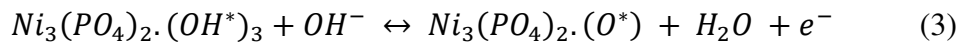
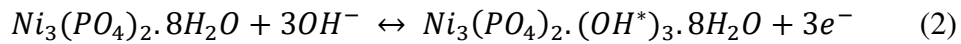


Figure-5. a) CV (at scan rates of 10 – 100 mV/s) (b) GCD (at current densities of 10, 15 and 20 mA/cm²) of the NPH electrode in 1 M KOH aqueous electrolyte.

The following are the expressions to signify the electrochemical redox aspects of the NPH electrode [35-37],



The NPH electrode showed a considerable area under the curve in the CV analysis, showing that it had better electrochemical behavior [32]. At the high scan rate, at which charges are stored at the surfaces hence, capacitive charge contribution rises as the scan rate rises.

The GCD is a useful approach for analyzing and comparing electrode charge storage capacity. **Figure-5b.** depicts the GCD curves of the NPH electrode. Because of the presence of plateau during charging-discharging, the GCD profiles of the NPH electrode show Faradic type behavior. The accompanying formulae were used to calculate the electrodes' charge storage capacity,

$$C = \frac{I_d \times t_d(s)}{m(g) \times \Delta V(V)} \quad (5)$$

$$C_{sp} = \frac{I_d(A) \times t_d(s)}{m(g) \times 3600} \quad (6)$$

$$\text{Energy density (E)} \left(\frac{Wh}{kg} \right) = \frac{C \left(\frac{F}{g} \right) \times V^2(V)}{2 \times 3.6} \quad (7)$$

$$\text{Power density (P)} \left(\frac{W}{kg} \right) = \frac{E \left(\frac{Wh}{kg} \right) \times 3600}{t_d(s)} \quad (8)$$

Where C denotes the specific capacitance (F/g), C_{sp} represents the specific capacity

(mAh/g), I_d signifies the current density (A), t_d represents the discharge time (s), m refers the deposited mass (g), and V symbolizes the potential window (V). The determined specific capacitance and specific capacity values for the NPH electrode are shown in **Table-1**.

Table-1. Table displaying the supercapacitive properties of NPH electrodes at different current densities.

Sample code	Current density (I_d) (mA/cm ²)	Specific capacitance (F/g)	Specific capacity (mAh/g)	Rate capability (%)	Energy Density (Wh/kg)	Power Density (W/kg)	Energy Efficiency (%) = $\frac{\text{Energy density while discharging}}{\text{Energy density while charging}}$
NPH	10	104	22	100	8.13	750	91
	15	68	14	65	5.32	1125	85
	20	56	12	53	4.33	1500	82

To study the rate capabilities of the NPH electrode GCD techniques was analyzed at varied current densities. The NPH electrode sustains specific capacitance up to 53% at 20 mA/cm² relative to 10 mA/cm² as shown in **Figure-5b**. The rate capability aspects of the NPH electrode are shown in **Table-1**. The NPH electrode's electrochemical performance might be attributed to the uniform covering of NPH microplates over nickel foam, which boosts the electrochemical performance. The NPH electrode exhibits improved electrochemical characteristics as a result of all of these aspects [20, 38, 39].

The electrochemical impedance of the NPH electrode was studied throughout a frequency range of 100 kHz to 0.1 Hz with an open circuit potential and an AC amplitude of 10 mV. The Nyquist plot of the NPH electrode is shown in **Figure-6a**. Generally, the Nyquist plot is divided into two parts: the high-frequency semicircle (which includes details on interfacial interactions) and the low-frequency vertical line (data concerning capacitive behavior). Because of the binder-free grown microplates, the NPH electrode does not display a semicircle in the high-frequency area, indicating minimal or no charge transfer resistance. The electrolytic resistance (R_s) for NPH electrode is 1.60 Ω , demonstrating a low internal resistance.

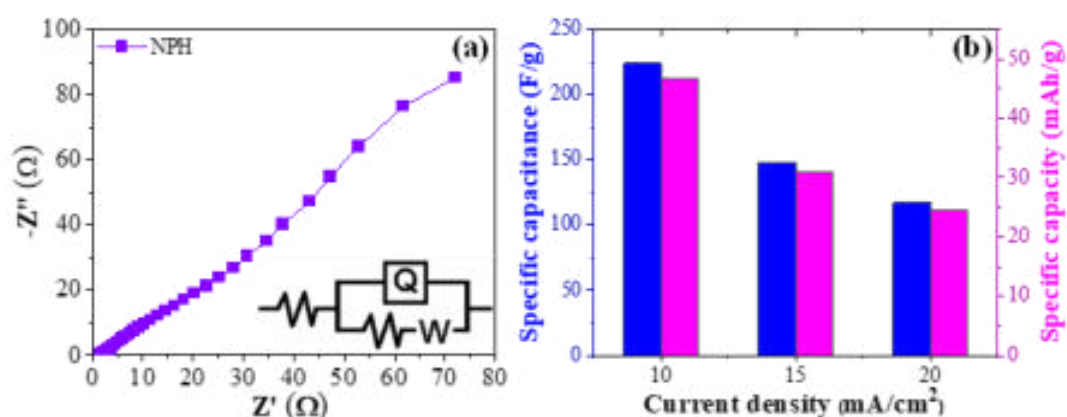


Figure-6. a) Nyquist plot of the NPH electrode (in the frequency range of 100 kHz to 0.1 Hz). b) Graph of Specific capacitance and specific capacity as a function of current density for the NPH electrode.

4. CONCLUSION

The simple hydrothermal approach was used to effectively produce nickel phosphate hydrate electrode. XRD pattern confirms the synthesis of nickel phosphate hydrate on 3D nickel foam. The occurrence of phosphate and hydrate groups in the electrode is confirmed by FTIR spectroscopy. SEM images reveal the uniform growth of nickel phosphate hydrate microplates on 3D nickel foam. The NPH electrode has a specific capacitance of 104 F/g (21.66 mAh/g) at 10 mA/cm², 8.12 Wh/kg energy density, and 750 W/kg power density. According to the findings of the thorough investigation, the synthesis of nickel phosphate hydrate microplates is beneficial for boosting energy density. Ultimately, the use of low-cost synthesis material and methodology will be beneficial for emerging energy storage technologies.

ACKNOWLEDGEMENT

Satyajeet S. Patil would like to acknowledge Golden Jubilee Research Fellowship (GJRF), Shivaji University, Kolhapur (MS) India, for providing financial assistance. The authors are thankful to DST-PURSE Phase II (2018-2023) and the UGC DSA Phase II (2018-2023) Program for providing research facilities at the Department of Physics, Shivaji University, Kolhapur (MS) India.

REFERENCES

1. Simon, P., Gogotsi, Y., Dunn, B. (2014) *Science*, 343, 1210-1211.
2. Sharma, G. P., Pala, R. G. S., Sivakumar, S. (2019) *Electrochimica Acta*, 318, 607-616.
3. Theerthagiri, J., Durai, G., Karuppasamy, K., Arunachalam, P., Elakkiya, V., Kuppusami, P., Maiyalagan, T., Kim, H. S. (2018) *Journal of Industrial and Engineering Chemistry*, 67, 12-27.
4. Liu, Y., Peng, X. (2017) *Applied Materials Today*, 8, 104-115.
5. Anasori, B., Lukatskaya, M.R., Gogotsi, Y. (2017) *Nature Reviews Materials*, 2, 16098.
6. Bendi, R., Kumar, V., Bhavanasi, V., Parida, K., Lee, P. S. (2016) *Advanced Energy Materials*, 6, 198.
7. Murugavel, R., Choudhury, A., Walawalkar, M. G., Pothiraja, R., Rao, C. N. R. (2008) *Chemical Reviews*, 108, 3549-3655.
8. Chang, Y. C., Wang, S. L. (2012) *Journal of the American Chemical Society*, 134, 9848-9851.
9. Zhan, Y., Lu, M., Yang, S., Xu, C., Liu, Z., Lee, J. Y. (2016) *ChemCatChem*, 8, 372-379.
10. Touny, A. H., Tammam, R. H., Saleh, M. M. (2018) *Applied Catalysis B: Environmental*, 224, 1017-1026.
11. Kim, H. D., Amirthalingam, S., Kim, S. L., Lee, S. S., Rangasamy, J., Hwang, N.S. (2017) *Advanced Healthcare Materials*, 6, 1700612.
12. Huang, H., Faulkner, T., Barker, J., Saidi, M. Y. (2009) *Journal of Power Sources*, 189, 748-751.
13. Yang, J. H., Tan, J., Ma, D. (2014) *Journal of Power Sources*, 260, 169-173.
14. Zhao, J., Wang, S., Run, Z., Zhang, G., Du, W., Pang, H. (2015) *Particle & Particle Systems Characterization*, 32, 880-885.
15. Li, X., Elshahawy, A. M., Guan, C., Wang, J. (2017) *Small*, 13, 1701530.
16. Liang, T., Li, G., Wojtas, L., Antilla, J. C. (2014) *Chemical Communications*, 50, 14187-14190.
17. Li, N., Xu, Z., Liu, Y., Hu, Z. (2019) *Journal of Power Sources*, 426, 1-10.
18. Mirghni, A. A., Madito, M. J., Masikhwa, T. M., Oyedotun, K. O., Bello, A., Manyala, N. (2017) *Journal of Colloid and Interface Science*, 494, 325-337.
19. He, Y., Yang, X., Bai, Y., Zhang, J., Kang, L., Lei, Z., Liu, Z. H. (2015) *Electrochimica Acta*, 178, 312-320.
20. Zhao, J., Pang, H., Deng, J., Ma, Y., Yan, B., Li, X., Li, S., Chen, J., Wang, W. (2013) *CrystEngComm*, 15, 5950-5955.
21. Li, N., Xu, Z., Liu, Y., Hu, Z. (2019) *Journal of Alloys and Compounds*, 789, 613-621.
22. Mahmoud, B. A., Mirghni, A. A., Fasakin, O., Oyedotun, K. O., Manyala, N. (2020) *RSC Advances*, 10, 16349-16360.

23. Zhang, X., Li, J., Sun, Y., Liu, Q., Guo, J. (2019) *Electrochimica Acta*, 299, 835-843.
24. Omar, F.S., Numan, A., Duraisamy, N., Bashir, S., Ramesh, K., Ramesh, S. (2016) *RSC Advances*, 6, 76298-76306.
25. Senthilkumar, B., Sankar, K. V., Vasylechko, L., Lee, Y. S., Selvan, R. K. (2014) *RSC Advances*, 4, 53192-53200.
26. Wang, T., Hao, Q., Liu, J., Zhao, J., Bell, J., Wang, H. (2016) *RSC Advances*, 6, 45986-45992.
27. Abdelsalam, M. E., Elghamry, I., Touny, A. H., Saleh, M. M. (2019) *Journal of Applied Electrochemistry*, 49, 45-55.
28. Li, Q., Xu, Y., Zheng, S., Guo, X., Xue, H., Pang, H. (2018) *Small*, 14, 1800426.
29. Yan, S., Abhilash, K. P., Tang, L., Yang, M., Ma, Y., Xia, Q., Guo, Q., Xia, H. (2019) *Small*, 15, 1804371.
30. Patil, S. S., Tarwal, N. L., Yadav, H. M., Korade, S. D., Bhat, T. S., Teli, A. M., Karanjkar, M. M., Kim, J. H., Patil, P. S. (2018) *Journal of Solid State Electrochemistry*, 22, 3015-3024.
31. Noisong, P., Danvirutai, C., Srithanratana, T., Boonchom, B. (2008) *Solid State Sciences*, 10, 1598-1604.
32. Kullyakool, S., Danvirutai, C., Siriwong, K., Noisong, P. (2014) *Journal of Thermal Analysis and Calorimetry*, 115, 1497-1507.
33. Zhao, Y., Chen, Z., Xiong, D.-B., Qiao, Y., Tang, Y., Gao, F. (2016) *Scientific Reports*, 6, 17613.
34. Liang, B., Chen, Y., He, J., Chen, C., Liu, W., He, Y., Liu, X., Zhang, N., Roy, V.A.L. (2018) *ACS Applied Materials & Interfaces*, 10, 3506-3514.
35. Bajdich, M., García-Mota, M., Vojvodic, A., Nørskov, J.K., Bell, A.T. (2013) *Journal of the American Chemical Society*, 135, 13521-13530.
36. Kim, H., Park, J., Park, I., Jin, K., Jerng, S.E., Kim, S.H., Nam, K.T., Kang, K. (2015) *Nature Communications*, 6, 8253.
37. Peng, X., Chai, H., Cao, Y., Wang, Y., Dong, H., Jia, D., Zhou, W. (2018) *Materials Today Energy*, 7, 129-135.
38. Raju, K., Ozoemena, K. I. (2015) *Scientific Reports*, 5, 17629.
39. Wang, Z., Gu, J., Liu, X., Sun, X., Li, J., Li, S., Tang, S., Wen, B., Gao, F. (2018) *Nanotechnology*, 29, 425401.

Synthesis and Characterization of Barium Titanate Perovskite by Co-precipitation for Oxygen Evolution Reaction

Rohit K. Kamble^a, Sharadchandra S. Patil^a, Prashant N. Nikam^a, Umesh M. Chougale^a, Gaurav M. Lohar^b, Vijay J. Fulari^{a,*}

^aDepartment of Physics, Shivaji University, Kolhapur 416 004 (MS) India.

^bLal Bahadur Shastri College of Arts, Science and Commerce, Satara 415 002 (MS) India.

*Corresponding author: vijayfulari@gmail.com

ABSTRACT

Barium Titanate (BaTiO₃) (BTO) nanospheres were synthesized using the simple one-step Co-precipitation method. The prepared BTO samples were annealed at 950^oC. The BTO sample with have been further characterized by various physico-chemical techniques like XRD, FT-IR, FE-SEM, and EDS. The nanosized BTO samples exhibit spherical morphology. The electrocatalytic activity study showed an overpotential of 0.446 V at a current density of 10 mA cm⁻² and Tafel slope of 107 mV dec⁻¹ in 1 M NaOH solution. The current study reports catalytic activity of BTO sample with efficient OER finding its applications for catalysis.

KEYWORDS

Barium titanate, Electrocatalyst, FE-SEM, XRD, Nanosphere, Oxygen evolution reaction, Tafel plot.

1. INTRODUCTION

Modern society has greatly benefited from the most cutting-edge technologies since the first and second industrial revolutions. But these systems rely on exhaustible carbon-based fuels like gas, coal, and oil. Due to the increasing demand for energy, the constant depletion of non-renewable energy sources, and their effects on the environment, the focus of scientific research has switched to the progress of renewable energy resources [1-3]. Right now, fossil fuels supply 80% of that energy. As we know, the stock of fossil fuels under the earth's crust is limited and will be exhausted soon. Because of their origins, fossil fuels have high carbon content, hence burning them releases carbon dioxide (CO₂) into the atmosphere which causes the greenhouse effect [4-5]. Due to this, it is widely agreed that fossil fuels cannot be the major energy supplier. This motivated intense research into the pursuit and utilization of clean and sustainable alternative energy sources [6].

The two half-reactions in total water splitting are the cathodic hydrogen evolution reaction (HER) and the anodic oxygen evolution reaction (OER). OER typically takes place at the anode and has complex kinetics since it needs to oxidise two water molecules with four electrons, then remove four protons to create a relatively weak O-O bond (eqⁿ. 1) [7–10].



The structural and morphological changes in BTO can enhance catalytic efficiency in OER reaction could be achieved by Co-precipitation. The present study describe synthesis and electrocatalytic performance of BTO thin films. The impact of structural and morphological characteristics of BTO thin film was examined. In order to describe the ECSA (electrochemical active surface area) and Tafel plot will be plotted, the relevant OER activities also evaluated using linear sweep voltammetry (LSV) and EIS (electrochemical impedance spectroscopy) in 1 M NaOH electrolyte solution.

1. EXPERIMENTAL SECTION

2.1. Chemicals

All analytical-grade materials have been used for the experiment. The chemical includes Barium (II) Chloride [$\text{BaCl}_2 \cdot 2\text{H}_2\text{O}$], Titanium (III) trichloride [TiCl_3] and potassium hydroxide (KOH) which have been obtained from Thomas Baker India pvt Ltd. (Mumbai) and used as it is without further purification.

2.2. Synthesis of BTO Nanospheres

Barium titanate was synthesized using the co-precipitation method. In the first beaker 2.4428 ml of Titanium (III) trichloride (TiCl_3) was slowly added to 50 ml of distilled water at room temperature under continuous stirring, this is homogeneous solution. In the second beaker, 1.8971 g of Barium (II) chloride ($\text{BaCl}_2 \cdot 2\text{H}_2\text{O}$) was dissolved in 50 ml distilled water under continuous stirring. After 20min both aqueous solutions were mixed with continuous stirring under room temperature then 3 M NaOH solution was added into the solution to maintain the PH 13 at constant stirring.

Prior to deposition, a stainless-steel substrate (1×5 cm) was polished using various polishing papers. The substrate was first washed with 1 M H_2SO_4 and then applied to ultrasonic treatment to remove the greasy surface.

2.3. Characterizations

Morphology of BTO thin film was characterized by FE-SEM (field emission scanning electron microscopy, Mira-3, Tescan Pvt. Brno-Czech Republic), X-ray diffraction (XRD), (Bruker D2 phaser tabletop model) with a Cu $\text{K}\alpha$ radiation (1.5405\AA) was used to investigate the crystal phase of barium titanate. LSV (Linear sweep voltammetry), CV (Cyclic voltammetry), and EIS (electrochemical impedance

spectroscopy) measurements were conducted on an electrochemical workstation (CHI608e, CH Instruments) using a three-electrode configuration. The elemental analysis of samples was studied with EDS (energy-dispersive X-ray spectroscopy, Oxford Instrumentations), inbuilt with FE-SEM. All the electrochemical tests were carried out at room temperature.

2.4. Electrode Preparation and Electrochemical Measurements

The working electrode has been prepared BTO sample, using the mass proportionate ratio of 80:10:10, carbon black and polyvinylidene difluoride polymer binder are combined. A 1 cm x 1 cm section of SS was coated with a slurry of N-methylpyrrolidinone (NMP) and dried overnight at 80°C in a vacuum. Electrochemical experiments were performed using a CHI-608E instrument with standard three-electrode setup. The as-prepared sample were used directly as the working electrode (1 cm x 1 cm) in 1 M NaOH as the electrolyte. Nernst equation (Eqⁿ. 2) was used to convert the measured potential from the SCE scale to the reversible hydrogen electrode (RHE) scale as

$$E_{RHE} = E_{SCE} + 0.059 \times \text{pH} + E^0_{SCE} \quad (2)$$

Where E_{RHE} is converted potential vs RHE, E_{SCE} is the experimentally measured potential vs reference electrode (SCE) and E^0_{SCE} is standard redox potential of SCE at 298 K (0.244 V ± 0.002 V).

By using the Tafel equation to fit a linear section of the Tafel plot, the Tafel slope was calculated [8,11].

$$\eta = b \log j + a \quad (3)$$

2. RESULTS AND DISCUSSION

3.1. XRD

For the structural analysis of the sample, XRD was recorded in the 2θ range of 10-90°. **Figure-1** shows the XRD pattern of the BTO sample. The XRD pattern of the sample revealed the formation of BTO, with a tetragonal crystal structure [JCPDS card no. #892475]. The diffraction peaks at angles (2θ) of 22.2°, 31.5°, 38.9°, 45.2°, 50.8°, 56.1°, 65.9°, and 75.0° are assigned to the (100), (110), (111), (200), (210), (211), (220) and (310) planes of the BTO crystal lattice, with Lattice parameters a=b= c= 4.03 Å. The crystallite size (D) of the sample are estimated from Scherrer's formula [12].

$$D = \frac{0.9\lambda}{\beta \cos\theta} \quad (4)$$

Where all the symbols have usual meaning. The calculated crystallite size for BTO is 20 nm.

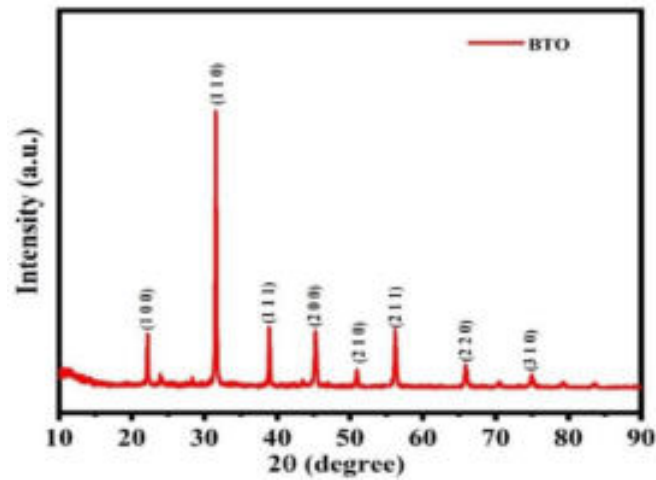


Figure-1. XRD pattern of the BTO sample.

3.2. FT-IR

FT-IR spectra of the synthesized BTO material, **Figure-2** the FT-IR spectra of BTO material in the range of $4000\text{-}400\text{ cm}^{-1}$. The peaks look as if in the range of $400\text{-}800\text{ cm}^{-1}$ is an M-O bond. The peaks at 560 cm^{-1} are given to Ti-O stretching modes. The individual peaks at 1446 cm^{-1} may be dispensed to stretching vibrations of a carbon-oxygen bond. The individual band at 1645 cm^{-1} specifies the bending / stretching mode of C-O. The specific broadband seems at 3450 cm^{-1} assigned to the stretching mode of the O-H bond. From the FT-IR analysis, the formation of BTO material is confirmed by the existence of the Ba-Ti-O bond [13].

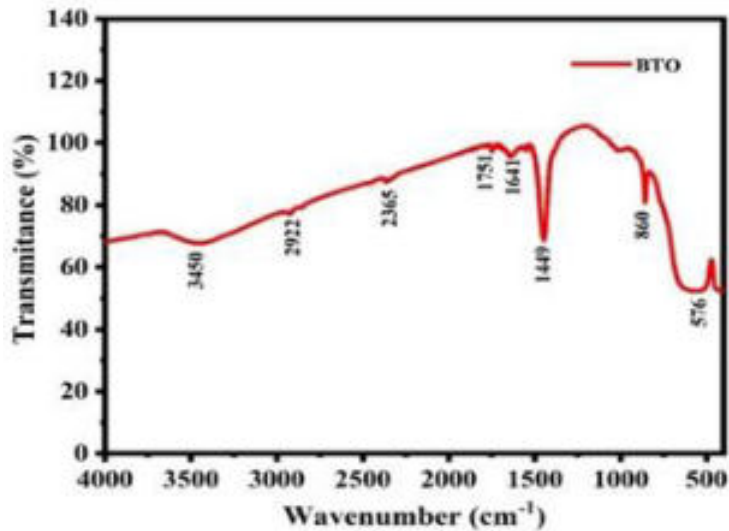


Figure-2. FT-IR of the BTO sample.

3.3. FE-SEM and EDS

The FE-SEM image of BTO sample is shown in **Figure-3A**. It is found that the surface morphology of BTO shows clear nano-spheres is observed. It is observed that the diameter of nano-spheres increases with an increase in the particle size of material due to the interconnected nano-spheres. In the study of chemical stoichiometry quantitative analysis technique EDS was used. **Figure-3B** shows the recorded EDS spectrum on a selected area of the BTO sample by the co-precipitation method exhibited elemental peaks only for barium (Ba), titanium (Ti), and oxygen (O) substantiating the presence of the important elements in the as-synthesized BTO as shown in table 1 compositional analysis of BTO. The present sample study shows that the prepared BTO consists of O, Ba, and Ti. These results indicated confirmed the formation of BTO nanosphere.

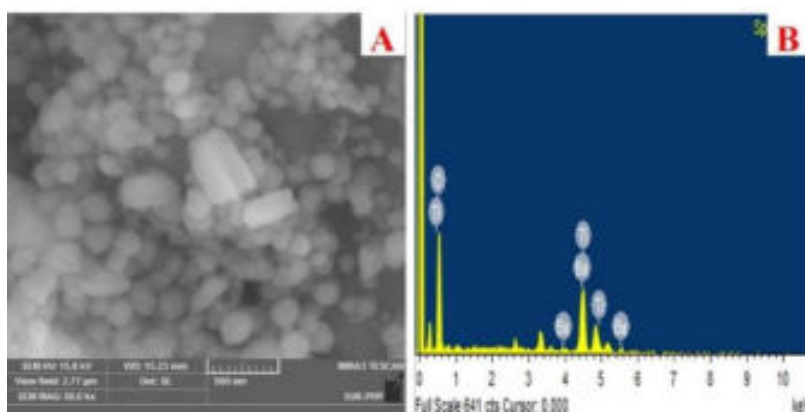


Figure-3. A) The FE-SEM and B) EDS spectra of the BTO sample.

Table-1. Compositional analysis from EDS of BTO sample.

Sr.No.	Sample	Weight%		
		Oxygen	Barium	Titanium
1	BTO	52.26	28.46	19.27

3. Electrochemical Measurement

Electrochemical properties of BTO sample were measured by LSV and CV techniques to analyse OER activity. **Figure-5 A** shows the LSV curves for OER at a scan rate of 10 mV s^{-1} in electrolyte solution using 1 M NaOH . The polarization curve of BTO sample has a distinct oxidative peak at 0.446 V versus RHE, it reached the overpotential of 446 mV at the current density of 10 mA cm^{-2} . At the same time,

the current density of BTO sample shows an obvious increase in the potential range of 0 to 0.7 V. The electrocatalytic activity of the prepared perovskite BTO toward OER has been examined by using Tafel linear polarization measurements. **Figure-5 B** Tafel curve verified in the potential region of Oxygen evolution for the platinum electrode. The BTO sample exhibited an overpotential of 446 mV at a current density of the 10 mA cm^{-2} and Tafel slope of 107 mV dec^{-1} .

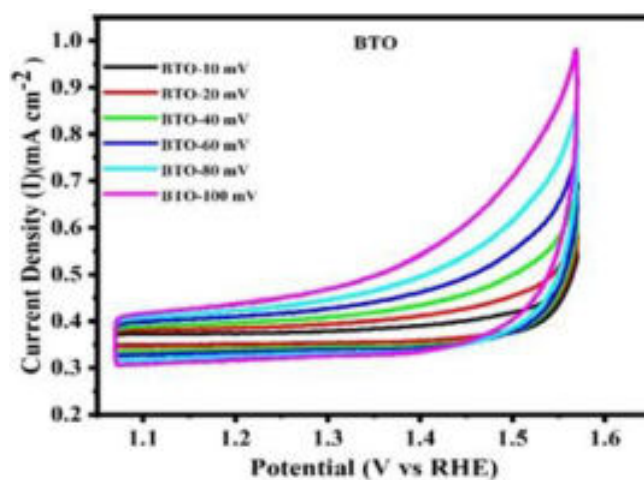


Figure-4. CV of the BTO sample.

Cyclic voltammetry (CV) is a powerful analytical technique to study electrochemical reactions, which is presented in **Figure-4**. In the solution of NaOH cyclic voltametric study is performed by using the standard three-electrode system such as stainless steel (SS) substrate as cathode, platinum electrode as anode and SCE as the reference electrode. The voltametric curves are scanned in the potential range of 0.00 to 0.45 V vs SCE. The typical cyclic voltammograms recorded for BTO sample substrate electrode in an aqueous solution mixture at different scan rate at room temperature an enlarged view of the CV curve.

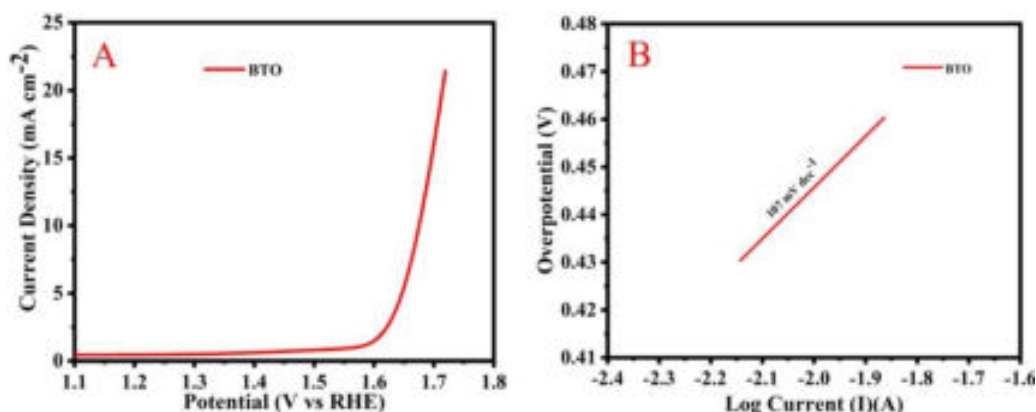


Figure-5. A) LSV and B) Tafel plot of the BTO sample.

The electrochemical impedance spectroscopy (EIS) measurement can be processed at the electrode-electrolyte interface can be better understood. **Figure-6** illustrates representative Nyquist plots designed for BTO sample from 10 Hz to 100 KHz by the amplitude of 10 mV. illustrations of representative Nyquist plot for all the samples with the current collector (CC) and 1M NaOH as an electrolyte. The inset shows the equivalent circuit electrodes **Figure-6** for EIS. The equivalent circuit is made up of two resistances one R_s is solution resistance and another R_{ct} is charge transfer resistance. It is seen that the R_s value of BTO thin film in NaOH is $2.61 \Omega \text{ cm}^{-2}$, respectively. Also, R_{ct} value of the BTO sample is $78.41 \Omega \text{ cm}^{-2}$.

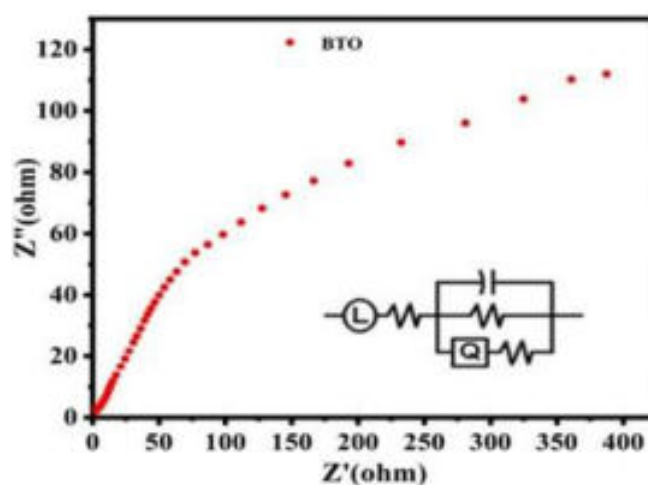


Figure-6. EIS of the BTO sample and the equivalent circuit model.

4. CONCLUSIONS

The BTO nanospheres was synthesized by a simple Co-precipitation method. The structural properties of XRD shows BTO has a tetragonal crystal structure. FE-SEM image shows BTO has a nano spherical morphology. EDS is confirmed that product contains only oxygen, barium and titanium having atomic weight 52.26, 28.46 and 19.17% respectively. The of BTO sample for the OER exhibited an overpotential of 446 mV at a current density of the 10 mA cm^{-2} and Tafel slope of 107 mV dec^{-1} . The electrochemical impedance spectroscopy measured the R_s value of BTO thin film in NaOH are $2.61 \Omega \text{ cm}^{-2}$, respectively. Also, R_{ct} value of BTO thin film is $78.41 \Omega \text{ cm}^{-2}$.

ACKNOWLEDGMENTS

Author R. K. Kamble would like to acknowledge the UGC (University Grand Commission) Government of India, for providing financial assistance through UGC-NFSC (National Fellowship for Scheduled Cast) JRF fellowship, No. F. 82-1/2018

(SA-III). The author is thankful to the UGC for the DSA-SAP Phase-II programme, and the DST-PURSE Phase-II programme through which research facilities were made available in the Department of Physics, Shivaji University, Kolhapur.

REFERENCES

1. Suen, N. T., Hung, S. F., Quan, Q., Zhang, N., Xu, Y. J., Chen, H. M. (2017) *Chemical Society Reviews*, 46, 337-365.
2. Chu, S., Majumdar, A. (2012) *Nature*, 488, 294-303.
3. Kale, S. B., Lokhande, V. C., Marje, S. J., Patil, U. M., Kim, J. H., Lokhande, C. D. (2020) *Applied Physics A*, 126, 206.
4. Olah, G. A., Prakash, G. K. S., Goepfert, A. J. Am. (2011) *Chemical Society* 133, 12881-12898.
5. Woodward, A., Smith, K. R., Campbell-Lendrum, D., Chadee, D. D., Honda, Y., Liu, Q., Olwoch, J., Revich, B., Sauerborn, R., Chafe, Z., Confalonieri, U., Haines, A. (2014) *The Lancet*, 383, 1185-1189.
6. Zhang, P., Zhang, J., Gong, (2014) *Chemical Society Reviews*, 43, 4395-4422.
7. Zuo, X., Chang, K., Zhao, J., Xie, Z., Tang, H., Li, B., Chang, Z. (2016) *Journal of Materials Chemistry A*, 4, 51-58
8. Yuan, C. Z., Jiang, Y. F., Wang, Z., Xie, X., Yang, Z. K., Yousaf, A. B., Xu, A. W. (2016) *Journal of Materials Chemistry A*, 4, 8155-8160.
9. Katkar, P. K., Marje, S. J., Kale, S. B., Lokhande, A. C., Lokhande, C. D., Patil, U. M. (2019) *CrystEngComm*, 21, 884-893.
10. Shang, X., Li, X., Hu, W. H., Dong, B., Liu, Y. R., Han, G. Q., Chai, Y. M., Liu, Y. Q., Liu, C. G. (2016) *Applied Surface Science*, 378, 15-21.
11. Oshida, T., Kojima, K. Toyota (2015) *INTERFACE Magazine*, 24, 45-49.
12. Lohar, G. M., Thombare, J. V., Shinde, S. K., Han, S. H., Fulari, V. J. (2014) *Journal of Materials Science: Materials in Electronics*, 25, 1597-1604.
13. Suryani, S. E. I., Ristanti, I., Diantoro, M., Wisodo, H., Taufiq, A., Mufti, N. (2020) *Journal of Physics: Conference Series*, 1595, 012009.

Air Quality and Air Ion Assessment Ratio for Papaya, Chickpea, and Guava Vegetation Area at Rural Station Khatav (16°57'N, 74° 31'E)

Subhash D. Pawar^a, Gajanan B. Patil^{b,*}, Prachi G. Patil^c, Pratik G. Patil^d,
Jalindar L. Bhosale^e

^aDepartment of Physics, A. C. S. College, Palus 416 310 (MS) India.

^bDepartment of Physics, Secondary School & Jr. College, Bhilawadi 416 303 (MS) India.

^cDepartment of Chemical Engineering, Institute of Chemical Technology, Jalna 431 203 (MS) India.

^dDepartment of Computer Science, Modern College of Engineering, Pune 411 005 (MS) India.

^eDepartment of Physics, Shikshan Maharshi Dr. Bapuji Salunkhe College, Miraj 416 410 (MS) India.

*Corresponding author: gajananpatil2004@gmail.com

ABSTRACT

Air ions play an important role in the determination of air quality and healthy environments for human beings living environment. The positive and negative air ions are measured in Chickpea (Cicer arietinum) Phule G-12 variety and Papaya (Carica papaya) of Pusa Delicious variety and Guava (Psidium guajava) of variety Lalit at rural station Bhilawadi (India) with help of Gerdien type air ion counter. These vegetation areas showed a remarkable count of negative air ions than positive air ions in the early morning, and midnight and lower in mid-day and late afternoon. The pollution index is the ratio of the number of positive air ions to the number of negative air ions. It is an air quality symbol. For a healthy human, it should be less than one. In Papaya, it is found to be 0.71, for Chickpea and 1.0 for Guava 0.9, which is good for human beings' health. Papayas and Chickpeas show enormous convergence of negative air ions. Radon exhalation, transpiration, and photosynthesis are generators of negative air ions. Thus, Chickpea, papaya, and Guavas are natural air ionizers and air purifiers.

KEYWORDS

Air ions, Ion counter, Transpiration, Photosynthesis, Ionizer, Pollution index.

.....

1. INTRODUCTION

Air ions have an electric charge and conductivity. Air ions are produced by natural as well as artificial activities. They are produced by cosmic rays, Radon exhalation, shearing forces of water (Lenard effect), lightning, corona discharge, and plant-based air ion generation [1-3]. Out of this negative air, ions are beneficial for humans. There are three types of air ions viz small, intermediate, and large depending upon their size and mobility. They are harmful or beneficial is depends upon their concentration and proportion in the air. Headache, fatigue, high blood pressure,

nervousness, decrease in work productivity occurs due to a higher quantity of positive air ions [4]. Negative air ions have a positive impact on human health. We feel happy, delightful, and relaxed, and breathe easily due to the presence of negative air ions [5].

The level of serotonin (5-hydroxytryptamine) in the blood decreases due to negative air ions [6] which affects mood and pain relief. Nowadays, air pollution has become a major environmental risk for public health.

The global burden of disease may be reduced by reducing the level of the pollution index. According to WHO, approximately 1.3 million deaths occur worldwide in developing countries due to indoor and outdoor air pollution. Vegetation canopies can act as a sink for gaseous as well as particulate air pollutants also [7]. Generally, there are three ways to remove air pollutants by plants from the air A) absorption by the leaves, B) deposition of particulate matter on the surfaces of leaves, and C) fallout of particulate on the leeward side of vegetation due to slowing of air movements [8].

The seasonal variations in the level of air pollutants depend upon meteorological factors like temperature and relative humidity. Higher humidity causes the settling down or washing of atmospheric particulate matter by precipitations [9]. The attachment of small ions to aerosol particles depends upon the mobility of air ions [10,11]. Air ions having high mobility are attached to the aerosol particles and settle down on the ground [12]. In clean atmospheric places, the concentration of aerosol particles is less and as a result, the concentration of air ions is higher as compared to urban areas [13]. In this study, the measurement of air ion concentration of Chickpea and papaya vegetation area enables us to understand the plausible mechanisms for the generation of air ions and pollution index which affects the air quality.

2. MATERIAL AND METHOD

Chickpeas (*Cicer arietinum*) Phule G-12 variety, Papaya (*Carica papaya*) of Pusa Delicious variety, and Guava (*Psidium guajava*) of variety Lalit are cultivated in rural areas Bhilawadi. Chickpea is a vital fix in Mediterranean and Middle Eastern foods, utilized in hummus, and, when ground into flour, falafel. It additionally is significant in Indian food, utilized in plates of mixed greens, soups and stews, curry, chana masala, and other feast items like Channa. Being an amazing wellspring of iron, calcium, nutrients C, A, E, folate, cell reinforcements, and different supplements, chickpeas contribute vigorously to one's bone upkeep and improve the body's iron ingestion limit [14]. Along these lines, osteoporosis and paleness can be dealt with by the utilization of supplement thick chickpeas. Chickpeas have dissolvable dietary fiber called raffinose which helps the colon in the stomach-related interaction. It keeps up with that the gastrointestinal system is solid and encounters

routineness by flushing out poisons. Harvest its benefit to the fullest to get by and large stomach well-being.

Papaya is a low-calorie sweet-tasting natural product that is brimming with nutrients and minerals. Also, the best part is you can partake in all aspects of the organic product, from its tissue to its seeds. Papaya may likewise work as a characteristic painkiller in light of the chemical papain [13]. This compound builds the body's creation of cytokines, which are a gathering of proteins that assist with directing irritation. The organic product might lessen the torment brought about by joint pain and comparative conditions.

Guava is a tropical natural product that fills in the dry or damp hotness. Both the meaty product of the guava plant and the leaves are consumable, with the organic product frequently eaten as a bite and the leaves ordinarily bubbled into homegrown tea. Guava is low in calories and fats yet conveys a few fundamental nutrients, minerals, and cell reinforcement polyphenolic, and flavonoid intensifies that assume an urgent part in the anticipation of malignancies, maturing, contaminations, and so forth.

Khatav (16°57'N, 74°31'E), a rural station is 525 km away from Mumbai (India). **Figure-2** and **Figure-3** shows the location of the site. The Krishna River is at a distance of two kilometers away from this vegetation area. This vegetation area is alongside the road which has a frequency of 4 to 5 vehicles per hour. **Figure-1** shows the instrument used for the measurement of air ions is Gerdien condenser-based air ion counter which is designed and developed at Arts, Commerce & Science College, Palus. It works on the principle that the concentration of air ions is directly proportional to the air ion current [14]. This instrument is kept in a caged box at a height of one meter above ground level. The instrument set consists of a Gerdien condenser, data logger, Laptop with Rishcom software, and Op-amp AD549JH circuit for conversion of the small ionic current into voltage, power supply, and digital voltmeter. This low-cost instrument measures either positive or negative air ions at a time. The diurnal variation means ion change in ion concentration in the daily cycle that is completed every 24 hours. The time 00:00:00 to 24:00:00 is a diurnal cycle. We have measured these variations of positive and negative air ions for Papaya, Chickpea, and Guava. The air ion concentration in Papaya was measured in January 2019, that of Guava is measured in November and December 2018, and that of Chickpea in December 2019.



Figure-1. Experimental setup of air ion counter.

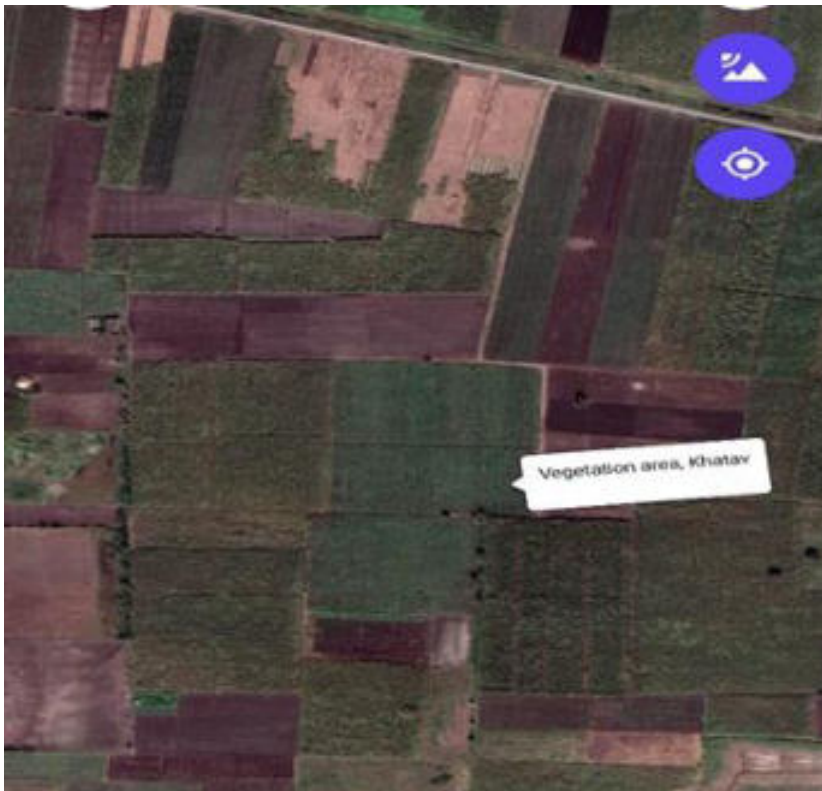


Figure-2. Vegetation area in Khatav.



Figure-3. Location of Khatav (India).

The air ion concentration of papaya is measured in January 2019 and that of Guava in December 2018 and that of chickpea in the month of chickpea in December 2019. All readings are expressed into $\times 10^2$ ions per cm^3 . For Papaya average count of positive air ions in Jan 2019 is 1890×10^2 ions per cm^3 . The negative air ions in Papaya are measured as 480×10^2 ions per cm^3 . For Guava the average positive air ions are found to be 1380×10^2 ions per cm^3 in December 2018. The average negative air ions measured are 294×10^2 ions per cm^3 . **Figure-2** shows a cracked Chickpea vegetation area and an experimental setup kept in the Guava vegetation area for the measurement of air ion concentrations. **Figure-3** shows the chickpea and Papaya vegetation area with an experimental setup for the measurement of air ion concentrations in the rural area of Bhilawadi. The cracked field and chickpea vegetation are shown in **Figure-4**. The vegetation of Guava with the experimental arrangement is in **Figure-5**. **Figure-6** indicates the vegetation area of Papaya at rural station Khatav. The diurnal variation of positive and negative air ion concentrations of papaya is shown in **Figure-7**.



Figure-4. Vegetation area of cracked field of chickpea.

Figure- 5. Vegetation area of Guava.

Figure- 6. Vegetation area of Papaya.

3. RESULTS AND DISCUSSION

The processes in the atmosphere produce small air ions. The primary air ions produced by ionization are O^- , OH^- , NO_2^- , O^{2-} , NO^- , CO_4^+ , O^{2+} , N^+ , O^+ , ... most common gases in the atmosphere. Complex water ions are proportional to humidity [15,16]. These air ions are produced by transpiration, photosynthesis, and respiration processes related to plants. Alpha, Beta, and Gamma decay from the cracked ground is also responsible for the formation of air ions. They provide energy to produce air ions. The average energy required for the generation of one ion pair for α - particle is



35 eV. For β - particles, X-rays and γ - rays are 33.8 eV [15-16]. The air ions produced by Radon 222 disintegration are 6.4×10^5 .

In photosynthesis, oxygen is released and in respiration, Carbon dioxide is released by plants. In transpiration, through cuticle and stomata, water-soluble radon is released into the atmosphere which produces energy for air ion production along with cosmic rays and electrode effect. **Figure-4** shows the diurnal air ion variation of the Guava vegetation area during January 2019 at the rural observatory Bhilawadi.

Figure-8 shows the diurnal variation of the chickpea vegetation area during Nov and Dec 2019. The cracked field of chickpea releases more radon gas and other radioactive radiations. The sticky and sour fluid of chickpea leaves attracts more aerosol particles so negative air ions are more in this area as compared to positive air ions. Geological factors and local humidity and temperature also affect the rate of air ion production. It may differ from place to place. The negative air ion concentration measured is 480×10^2 ions / cm^3 . The positive air ion concentration is found to be 1050×10^2 ions/ cm^3 in the morning session between 7 am to 11 am.

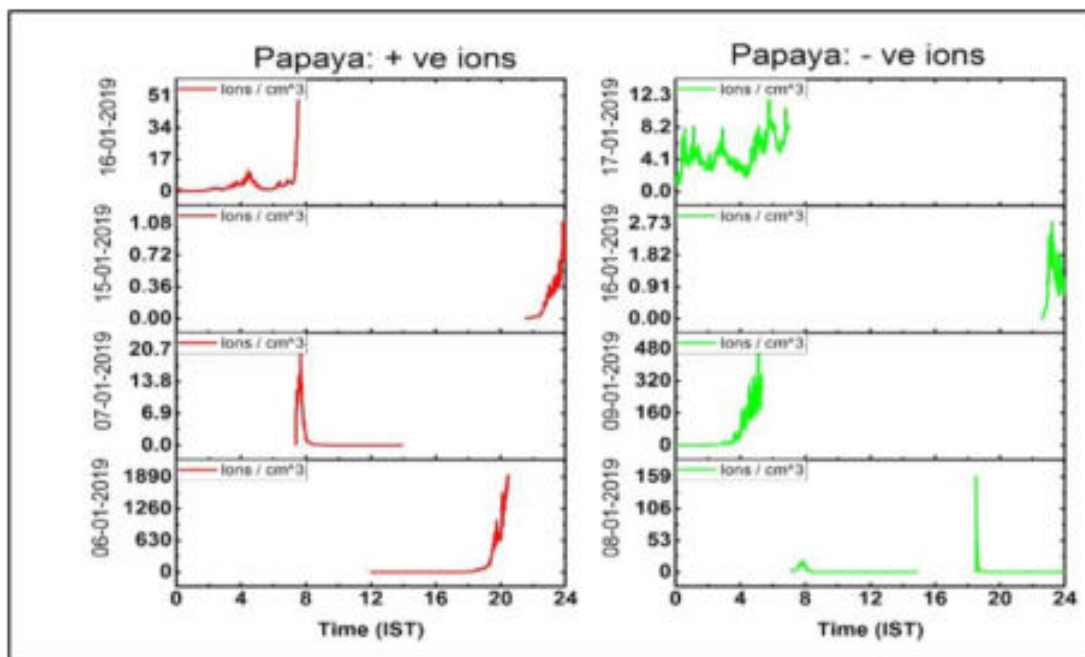


Figure-7. Diurnal air ion concentrations of positive and negative air ions for Papaya.

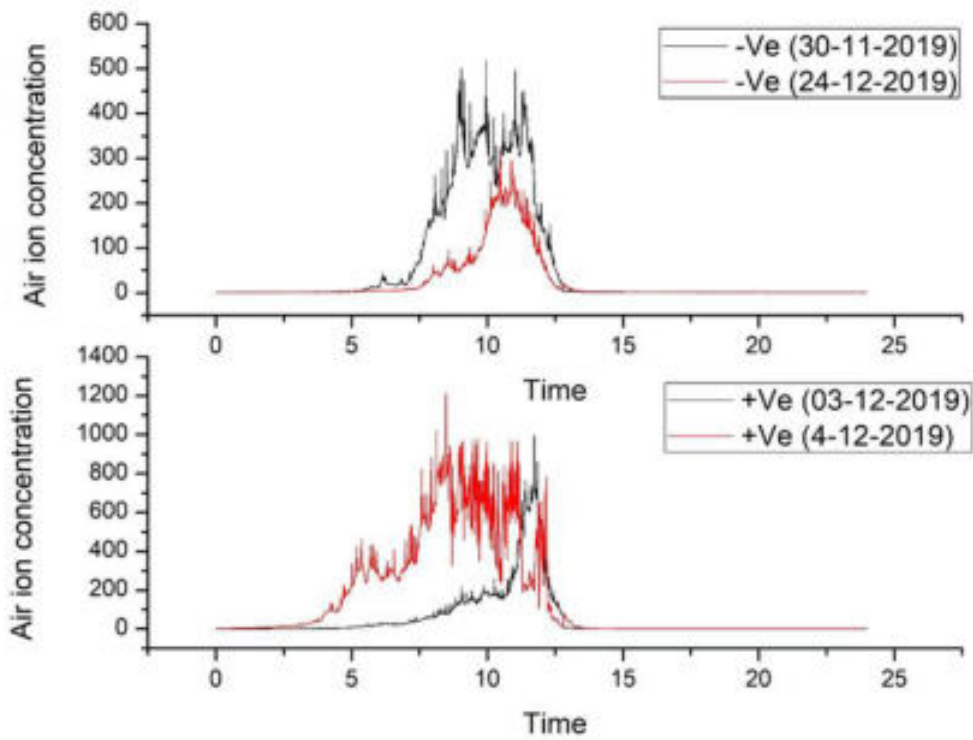


Figure- 8. The diurnal variation of Air ion concentration in the Chickpea vegetation area.

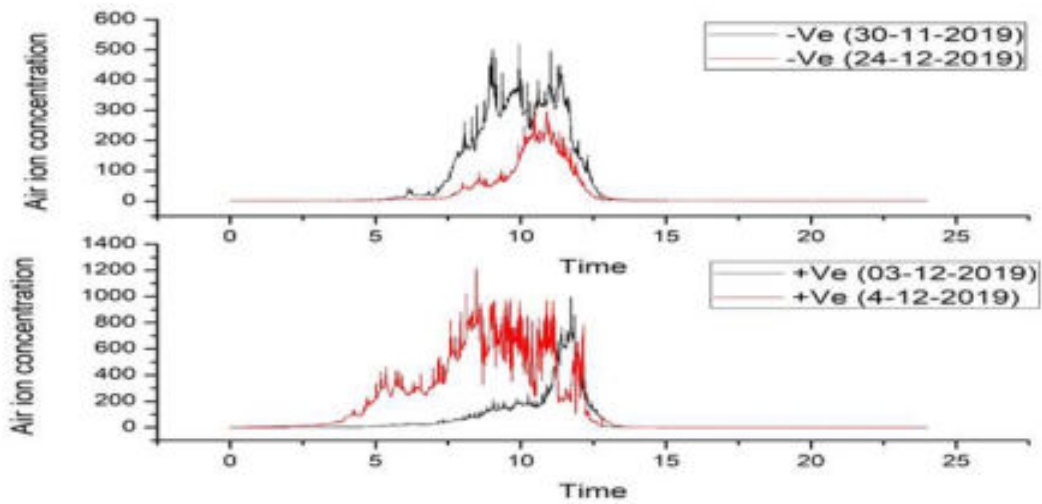


Figure-9. The diurnal variation of Air ion concentration in the Chickpea vegetation area.

The diurnal variation of air ion concentration of Guava vegetation for positive as well as negative air ions during Dec 2018 was shown in **Figure-10**. From 6 am to 10 am concentration of positive air, ions are more. From 8 am to 11 am, the concentration of positive air ions was found to be more. The temperature in guava is 24°C and the relative humidity is 37-39%.

Air ion concentration of Guava, Papaya, and Chickpea (**Figure-9**) is measured between December 2018 and January 2019 at rural station Bhilawadi. For the detection of air quality in the atmosphere, the pollution index and air ion assessment coefficient, are two components. The average value of positive and negative air ions is written in **Table-1** given below. The ratio of the number of positive air ions to the number of negative air ions is called as Pollution index or unipolarity ratio. For clean and fresh air pollution index should be less than one which is beneficial for human beings and animals. A pollution index greater than one indicates that the air is not clean, it is polluted and harmful to human beings and animals. The air ion assessment coefficient (C.I.) is the ratio of the number of negative air ions to the one thousand times pollution index [16]. For best air quality C.I. should be greater than one and C.I. less than one indicates poor and polluted air quality. **Table-1** shows the average number of positive and negative air ions, pollution index, and air assessment coefficient of Guava, Papaya, and chickpea vegetation area at rural station Bhilawadi. From **Figure-11**, it is clear that positive air ions and negative air ions produced by Papaya, Guava, and Chickpea vegetation areas are different but their average value is nearly the same. The generation of positive and negative air ions by plants is also different at different time duration. **Table-1** shows the pollution index and air ion assessment coefficient of different vegetation areas.

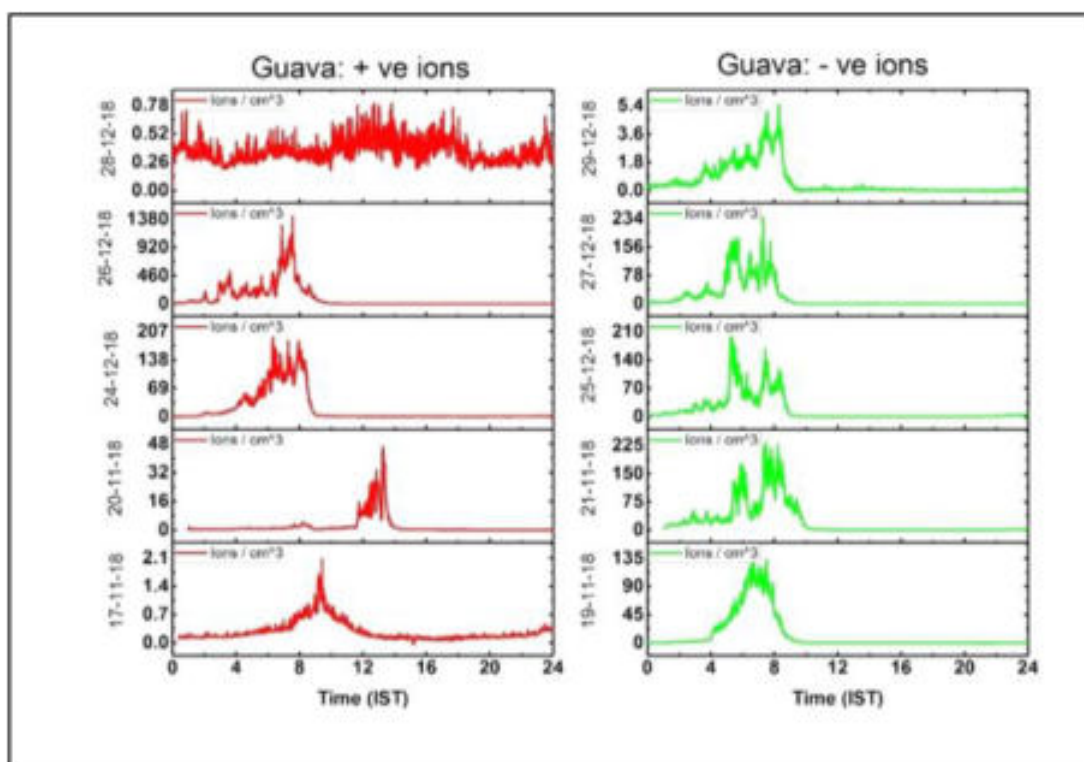


Figure-10. Diurnal air ion concentrations of positive and negative air ions for Guava.

The air ion assessment coefficient (C.I.) is the ratio of the number of negative air ions to the one thousand times pollution index [17]. For best air quality C.I. should be greater than one and C.I. less than one indicates poor and polluted air quality. **Table-1** shows the average number of positive and negative air ions, pollution index, and air assessment coefficient of Guava, Papaya, and chickpea vegetation area at rural station Bhilawadi. From **Figure-11**, it is clear that positive air ions and negative air ions produced by Papaya, Guava, and Chickpea vegetation areas are different but their average value is nearly the same. The generation of positive and negative air ions by plants is also different at different time duration. **Table-1** shows the pollution index and air ion assessment coefficient of different vegetation areas.

In the process of photosynthesis, oxygen is released into the atmosphere, and in the respiration process, CO₂ oxygen is given out in the atmosphere. In the transpiration process water vapor, which contains dissolved radon escapes into the atmosphere. This radon gas emits alpha, beta, and gamma radiation. These radiations provide energy for neutral oxygen, nitrogen, and CO₂ atoms, molecules which in turn

are responsible for the production of positive as well as negative air ions in the atmosphere. Thus, Papaya, chickpeas, and Guava produce positive as well as negative air ions independently. Human activities, burning gases, and smoke from factories increase the concentration of positive ions. Nature itself tries to balance ion concentrations but artificial interference from humans may lead to harmful air quality for all living things.

Table-1. The pollution index and air ion assessment coefficient of different vegetation areas.

Vegetation Area	Botanical Name	Average Positive air ions /cm³	Average Negative air ions /cm³	Pollution Index	Air ion assessment coefficient (C.I.)	Air Quality
Papaya	Carica papaya	51 X10 ²	62 X10 ²	0.71	8.73	Best air quality
Chickpea	Cicer arietinum	800 X10 ²	750 X10 ²	1.0	7.5	Good air quality
Guava	Psidium guajava	172 X10 ²	190 X10 ²	0.90	21.1	Clean and Pure, Fresh

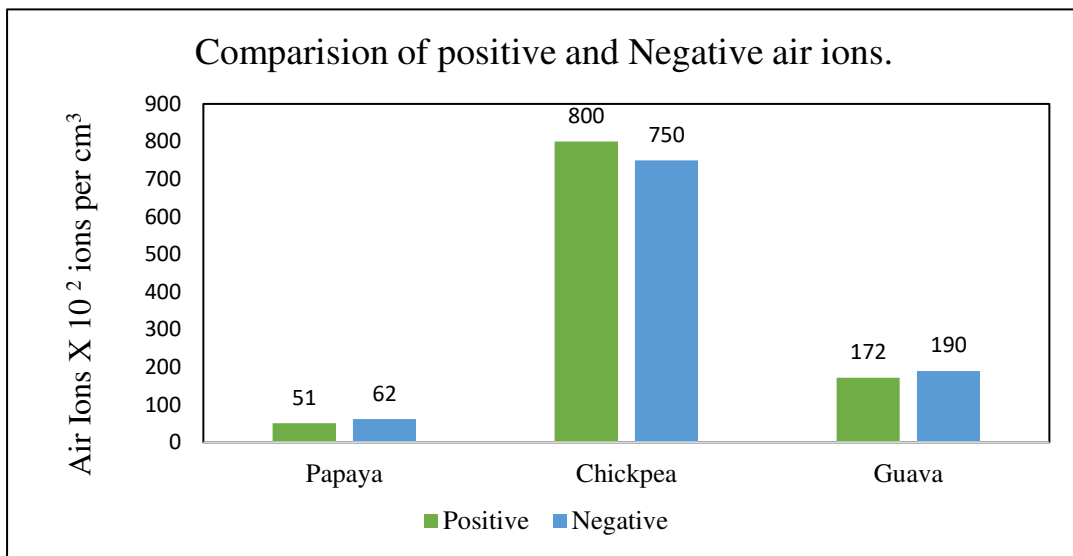


Figure-11. Comparisons of positive and negative air ions of different vegetation areas.

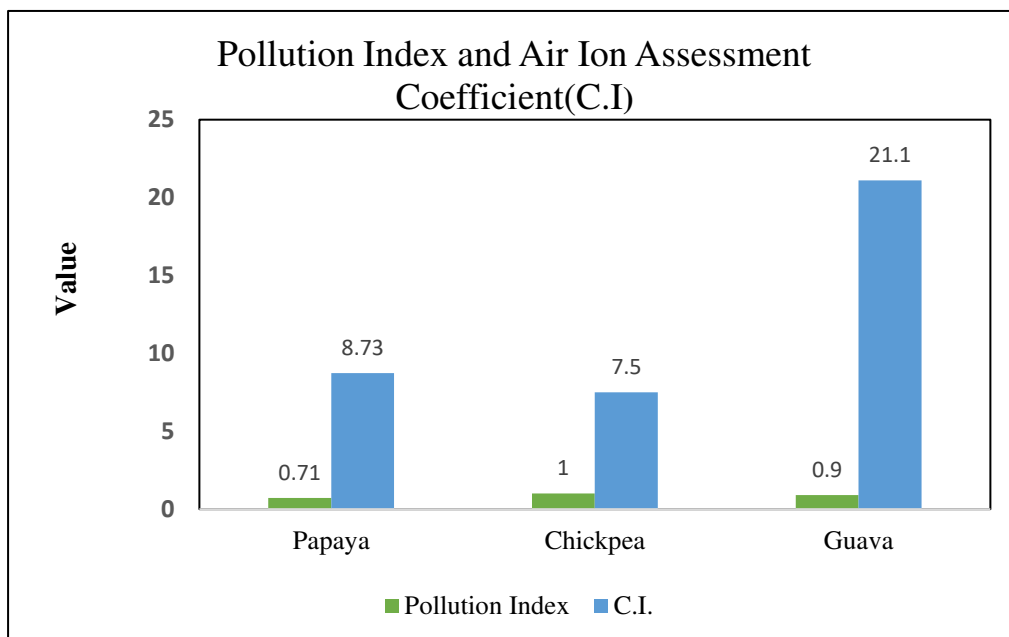


Figure-12. Comparisons of the pollution index and air ion assessment coefficient.

The pollution index and air ion assessment coefficient of Papaya, Chickpea, and Guava with standard error bars are shown in **Figure-12**. The results are the same in their respective scales. From the graph, it is clear that among these vegetation areas, Guava is found to have the best air quality free from air pollutants and aerosols. These results are in good agreement with results drawn in the measurement of air ions at Ramanandnagar [18,19]. In Australia, air ion concentrations in various urban outdoor environments were found to be more positive air ions [20]. The result from the atmospheric study of small air ions in a semi-Arid city in Northwest China coincides with it [21-23].

4. CONCLUSION

The diurnal air ion concentrations of Papaya, Guava, and Chickpea are found to be different. This air ion concentration depends upon the photosynthesis, transpiration, and respiration of plants. Temperature and humidity also play an important role in it. Air quality is best means it is rich in negative air ions. It contains less aerosol and other pollutants. It indicates fresh air. This is the reason why negative air ions are beneficial for human health. These natural negative air ions are a substitute for artificial air ionizers and to achieve it one has to go into nature. The air ionization rate depends upon the exhalation of radon from air and soil. It varies with time near the ground of vegetation area so air ion concentration is also different. The coefficient of unipolarity or pollution index in the diurnal variation of positive small ions was found to be close to that of negative air ions. i.e., 1 and 0.9 for chickpeas and Guava in the cold (winter) season. Our measurement of air ion concentration shows that negative air ions are more in Papaya and Guava during the morning period. But, for chickpeas, it is more from 10 to 11.30 am. The air quality in Papaya, Chickpea, and Guava is fresh, pure, and good.

REFERENCES

1. Tikhonov, V. P., Tsvetkov, V. D., Litvinova, E. G., Sirota, T. V., Kondrashova, M. N. (2004) *Journal of Plant Physiology*, 51, 414-419.
2. Iwama, H. (2004) *Indoor Air*, 14, 293-297.
3. Karma, A. K. (1972) *Journal of Geophysical Research*, 77, 5858-5869.
4. Kolartz, P., Gaiberger, M., Hofmann., W., Ritter, M. (2012) *Atmospheric Chemistry, Physics*, 12, 3687-3797.
5. Lenard, P., *Uber die* (1982) *Annals of Physics*, 46, 582-636.
6. Diamond, M. In *Enriching heredity: The impact of the environment on the anatomy of the brain*, edited by Diamond, M. C. (1988), pp 1-175.

7. Nowak, D. J., Crane, D. E., Stevens, J. C. (2006) *Urban Forestry & Urban Greening*, 4, 115-123.
8. Rawat, J. S., Banerjee, S. P. (1996) *Journal of Environmental Management*, 12, 109-116.
9. Sahu, S.K., Pandit, G. G., Sadasivan, S. (2004) *Science of The Total Environment*, 318, 245-249.
10. Hoppel, W. A. (1985) *Journal of Geophysical Research*, 90, 0148-0227.
11. Horrak, U., Salm, J., Tammet, H. (1998) *Journal of Geophysical Research: Atmospheres*, 103, 13909-13915.
12. Horrak, U., Salm, J., Tammet, H. (1995) *Journal of Aerosol Science*, 26, S429.
13. Dhanorkar, S., Kamra, A.K. (1993) *Journal of Geophysical Research: Atmospheres*, 98, 14895-14908.
14. Patil, G. B., Pawar, S. D., Bhosale, J. L. (2019) In *Journal of Physics: Conference Series*, 01172, 012010.
15. Keesee, R. G., Castleman, A.W. (1985) *Journal of Geophysical Research: Atmospheres* 90, 5885-5890.
16. Jesse, W. P., Sadaukis, J. (1957) *Physical Review* 107, 766.
17. Zhu, C., Ji, P., Li, S. (2017). *Journal of Environmental Engineering and Landscape Management*, 25, 39-55.
18. Pawar, S. D., Meena, G. S., Jadhav, D. B. (2010) *Aerosol and Air Quality Research* 10, 154-166.
19. Pawar, S. D. (2013) *Journal of Earth System Science* 122, 229-237.
20. Ling, X., Jayaratne, R., Morawska, L. (2010) *Atmospheric Environment* 44, 2186-2193.
21. Li, Y., Guo, X., Wang, T., Zhao, Y., Zhang, H., Wang, W. (2015) *Aerosol and Air Quality Research* 15, 865-874.
22. <https://www.everydayhealth.com/diet-nutrition/diet/papayas-nutrition-benefits-risks-how-eat-more/>.
23. <https://www.news18.com/news/lifestyle/5-amazing-health-benefits-of-chickpeas-3369287.html>

GUIDELINES FOR CONTRIBUTORS

- 1] **Journal of Shivaji University : Science & Technology** is the publication of Shivaji University, Kolhapur (Maharashtra, India), being published twice a year. It is an academic peer reviewed ISSN approved Journal.
- 2] The Journal welcomes research articles based on original research, review papers, research communication/notes by the faculty and research scholars working in various fields of Science and Technology. Articles/Papers can be submitted in English language only.
- 3] The length of manuscripts should not exceed 6000 words for review article, 5000 words for research article, 2000 words for research communication and 1000 words for research note.
- 4] The article/paper must accompany an **abstract not exceeding 200 words**.
- 5] During writing and submission of a manuscript, please follow the author guidelines available on the home page of Journal of Shivaji University: Science and Technology.
- 6] All the sources of literature referred to while writing the article/paper must be properly cited in the text. The serial numbers of End Notes, if any, must also be indicated within text at appropriate places.
- 7] The listing of references must follow the standard format.
- 8] Tables, charts, maps, figures etc. should be placed at appropriate places in the text of the article/paper and must be numbered serially with suitable headings. The tables should be referred to by their numbers within the text. Art-work for maps, figures and charts should be provided separately, if necessary.
- 9] Only articles evaluated and approved by the subject Experts/Referees/Departmental editorial board are considered for their publication in the Journal. The referees evaluate Article/ Paper drafts in term of structure and organization of paper/argument, originality of the research, appropriateness of abstract and introduction, literature review, methodology and data sources, data/evidence and conclusions, and quality of language.
- 10] The name of the author/co-author of the article being submitted should mentioned on the first page of the article/paper below title of that article. An asterisks (*) is used for defining corresponding author/s of a manuscript.
- 11] For any other information and for inquiries regarding submitted articles/papers preferably use e-mail communications. **(E-mail : editor:jscitech@unishivaji.ac.in)**
- 12] Manuscript should be sent to email of the Editor (**editor:jscitech@unishivaji.ac.in**) {or associate editor of the concerned subject}, Journal of Shivaji University: Science and Technology, Kolhapur with e-copy only (single M.S. word as well as PDF file).
Only research articles/review papers/research communication/notes prepared strictly in accordance with the above guidelines will be sent to referees for their evaluation and opinion about their acceptability or otherwise. We do not send back rejected articles.